Exploring Two-Dimensional Magnetism
By Scanning Nitrogen-Vacancy Magnetometry

Inauguraldissertation

zur

Erlangung der Würde eines Doktors der Philosophie
vorgelegt der
Philosophisch-Naturwissenschaftlichen Fakultät
der Universität Basel

von

Patrick Siegwolf

Basel, 2024

b _____

Genehmigt von der Philosophisch-Naturwissenschaftlichen Fakultät
auf Antrag von

Erstbetreuer: Prof. Dr. Patrick Maletinsky
Zweitbetreuer: Prof. Dr. Martino Poggio
Externer Experte: Dr. Jan Jeske

Basel, den 26.03.2024

Prof. Dr. Patrick Maletinsky   Prof. Dr. Marcel Mayor
Erstbetreuer   Dekan

Declaration

„Ich erkläre, dass ich die Dissertation "Exploring Two-Dimensional Magnetism By Scanning Nitrogen-Vacancy Magnetometry" nur mit der darin angegebenen Hilfe verfasst und bei keiner anderen Universität und keiner anderen Fakultät der Universität Basel eingereicht habe."

"I declare that I have written the doctoral thesis "Exploring Two-Dimensional Magnetism By Scanning Nitrogen-Vacancy Magnetometry" only with the help specified therein. And that I do not have submitted it at no other university and no other faculty of the University of Basel."

Basel, 26.02.2024

Abstract

Qubits represent the fundamental building blocks of emerging quantum technologies. Their properties are highly sensitive to the environment, making them well suited for sensing applications and enabling the exploration of new physics at the frontiers of current research. The nitrogen-vacancy (NV) is a particularly promising qubit for quantum sensing applications because its spin ground state can be manipulated, initialized, and read out in a simple setup, its Zeeman splitting allows for quantitative magnetic field measurements, its long spin coherence enables highly sensitive measurements, and diamond, as a host material, provides a robust framework for the fabrication of nanoscale sensors. Embedded in an all-diamond atomic force microscopy tip, the NV can be brought into close contact with a magnetic surface. This enables the quantitative recording of the arising stray magnetic field with high sensitivity and spatial resolution. Thus, scanning NV magnetometry (S-NVM) is a viable tool for studying various phenomena in solid state physics.

The discovery of two-dimensional (2D) magnets has opened a new field of research that requires novel imaging techniques to characterize them. S-NVM is a suitable technique to study these materials due to its sensitivity to detect the weak magnetic signals from even a single atomic layer, typically without perturbing the fragile magnetic state of these materials. Despite the constraints imposed by the photophysics and the quantization axis of the NV, S-NVM is able to operate over the full temperature and external field range relevant to 2D magnets.

S-NVM is applied to study the nanoscale magnetism of single-layer $EuGe_2$ grown by molecular beam epitaxy on a pre-patterned substrate. It is found that its average magnetization is described by a disordered 2D magnet with easy-plane anisotropy and low uniaxial in-plane anisotropy with a paramagnetic contribution. The disorder manifests itself in a complex magnetic texture on the film and can be described by a grain structure with a different critical temperature for each grain, replicating the observed statistics of the texture. Notably, the paramagnetic contribution is a property of each grain, indicating an internal structure below the spatial resolution of the technique.

S-NVM is also used to investigate the origin of the exchange bias in a $MnPS_3/Fe_3GeTe_2$ heterostructure observed in anomalous Hall effect transport measurements. Although $MnPS_3$ exhibits the magnetic structure of an ideal Heisenberg antiferromagnet with a perfectly compensated magnetic moment, a phase transition occurs below $40\,K$, giving rise to an uncompensated moment in the bulk crystal. This moment persists down to a few atomic layers and induces the exchange bias in the heterostructure.

These two examples demonstrate the great potential of S-NVM in exploring the rich physics of 2D magnetism. Thereby, it will contribute to new discoveries in the field and support the integration of 2D magnets into novel architectures for innovative spintronic devices.

Contents

List of symbols and abbreviations

Physical symbols

a, b, c	lattice constants
A_{ex}	exchange stiffness
B_{coer}	coercive field
$\boldsymbol{B}, B_i$	magnetic field
$B_{\text{EB}}, B_{\text{EB}}^{\infty}$	exchange bias field
B_{ext}	externally applied magnetic field
B_{flop}	spin-flop field
B_{NV}	magnetic field along the NV axis
C	relative PL contrast between the spin states
$D_{\text{gs}}, D_{\text{es}}$	ground state (excited state) zero-field splitting
E	energy
$\mathcal{F}$	lineshape
$\hat{H}$	Hamiltonian
I	nuclear spin quantum number
I, I_0, I_{PL}	PL intensity
J	magnetic moment for Brillouin function
	quantum number of total magnetic moment
	exchange constant
K_u	uniaxial anisotropy constant
$\boldsymbol{M} = (M, \varphi_M, \theta_M)$	spontaneous magnetization
M_{Sat}	saturation magnetization
$P(x)$	probability distribution of x
$\boldsymbol{S}, S_i(\hat{\boldsymbol{S}}, \hat{S}_i)$	spin vector (operator)
$\boldsymbol{r}$	position vector
S	spin quantum number
t	time
T	environmental temperature
T_1	spin relaxation time
T_2^*	spin dephasing time
T_2	spin coherence time
T_{c}	critical temperature, Curie temperature
T_{N}	Néel temperature
V_{AH}	anomalous Hall voltage
V_{bias}	bias voltage
$x, \langle x \rangle, \langle x^2 \rangle$	random variable, mean, variance
α, β, γ	angle between lattice constants

β	critical exponent of temperature dependence
γ	critical exponent of magnetic field dependence
$\delta\nu$	full width half maximum of resonance frequency
$\eta_{\mathrm{DC}}, \eta_B$	DC magnetic field sensitivity
η_M	sensitivity to magnetization
θ_{NV}	polar angle of NV
λ	optical wavelength
ν	microwave driving frequency
ν_0	resonant microwave frequency
σ	distribution parameter
ϕ_{NV}	azimuthal angle of NV

Constants

$h = 6.626 \cdot 10^{-34}\,\mathrm{m^2\,kg/s}$	Planck's constant
$\mu_0 = 1.257 \cdot 10^{-6}\,\mathrm{N/A^2}$	vacuum permeability
$\mu_{\mathrm{B}} = 9.274 \cdot 10^{-24}\,\mathrm{J/T}$	Bohr magneton
$g = 2.0028$	isotropic electron g-factor
$\gamma_{\mathrm{NV}} = 28\,\mathrm{GHz/T}$	gyromagnetic ratio of NV spin

Abbreviations

2D	two-dimensional
AFM	atomic force microscopy
	antiferromagnet, antiferromagnetic
AHE	anomalous Hall effect
BKT	Berezinskii-Kosterlitz-Thouless
cw	continuous-wave
DMI	Dzyaloshinskii-Moriya interaction
EB	exchange bias
FGT	Fe_3GeTe_2
FM	ferromagnet, ferromagnetic
GSLAC	ground-state level anticrossing
hBN	hexagonal boron nitride
HSQ	hydrogen silsesquioxane
IC	intersystem crossing
ICP	inductively coupled plasma
MBE	molecular beam epitaxy
MFM	magnetic force microscopy
MW	microwave
NV	nitrogen-vacancy
NW-MFM	nanowire magnetic force microscopy
ODMR	optical detected magnetic resonance

PID	proportional-integral-derivative
PL	photoluminescence
RIE	reactive ion etching
RF	radio frequency
SEM	scanning electron microscope
S-NVM	scanning nitrogen-vacancy magnetometry
SQUID	superconducting quantum interference device
TF	tuning fork
vdW	van der Waals
VSM	vibrating sample magnetometer/magnetometry
VTI	variable temperature inset

1. Introduction

The discovery of quantum mechanics and the subsequent development of quantum theory are important milestones in modern physics. They provide the fundamental understanding and mathematical framework to comprehend and describe the behavior of elementary particles, atoms, and molecules, leading to significant progress in the natural sciences and the emergence of new technologies. Nowadays, physicists are using the tools of quantum mechanics to control individual quantum objects for innovative technological concepts. The emerging quantum technologies are attracting increasing attention and major political institutions, such as the European Union, are ready to bridge the gap between fundamental research and technological applications like quantum communication, quantum cryptography, and quantum computing [1].

The basic building block for these technologies is a single physical object that exhibits two quantum states controllable by external means. In analogy to information technology, such a two-level system is referred to as a quantum bit or qubit. Qubits are realized by various physical systems such as trapped ions, quantum dots, superconducting circuits, dopants in semiconductors, or color centers in wide-band gap materials [2]. The ideal qubit is easy to integrate into larger systems, simple to control, and robust against external disturbances of the environment. However, controlling them is a major challenge due to the extreme sensitivity of quantum states to the environment. On the one hand, this hinders rapid progress in the field of quantum technologies, but on the other hand, this high sensitivity is the basis for quantum sensing technologies, that exploit the fragility of a qubit to sense the environment, outperforming classical sensing devices [3]. Quantum sensors are even considered to test postulates of modern physics on an unprecedented level, paving the way for new physics and increasing our knowledge about the nature and the universe [4].

Quantum sensors can be defined as sensors that use a quantum system with discrete, resolvable quantum levels that can be initialized, read out, and coherently manipulated [5]. The smallest implementations of such sensors contain only a single qubit, providing highly localized information about the environment that is spread only over the spatial extent of the qubit, approaching the size of a single atom or molecule in the case of color centers in solid-state systems. Moreover, the solid-state nature of their host facilitates their integration into nanometer-sized structures, allowing the advantages of quantum sensing to be applied to nanoscale sensing applications [6].

A particularly interesting color center for nanoscale quantum sensing is the nitrogen-vacancy (NV) in diamond. Its spin forms a qubit that can be initialized and read out all-optically, exhibits long coherence times, and shows a linear Zeeman effect, allowing sensitive and calibration-free measurements of the magnetic field [7]. The NV center, integrated into an atomic force microscopy setup, can be brought into close contact with a magnetic sample, allowing nanoscale imaging of magnetic surfaces by scanning the NV center across the substrate. After initial proof-of-principle experiments [6, 8, 9], scanning NV magnetometry (S-NVM) has been successfully

applied to image current distributions [10] and to study the microwave field of microscopic antennas [11]. However, S-NVM proves to be particularly well suited to study phenomena in the field of condensed matter physics [12], such as superconductors [13, 14], antiferromagnets [15, 16], electron transport in graphene [17, 18] or even dynamic phenomena such as the propagation of spin waves [19, 20].

With the discovery of two-dimensional (2D) magnetic systems [21, 22] a whole new field of condensed matter physics has emerged, providing opportunities to explore a new kind of magnetism at a reduced dimensionality, and opening new prospects in the field of spintronics due to the possibility of realizing 2D magnetic heterostructures [23]. Since these materials consist of only a few atomic layers, even down to a single atomic layer, their magnetic signal is rather weak and easily disturbed. Consequently, sensitive and non-invasive characterization techniques are required to study this novel type of materials. Although several optical characterization techniques are available, they provide only diffraction-limited spatial resolution and qualitative information about the magnetization. In contrast, scanning probe microscopy techniques offer higher spatial resolution and sensitivity. However, they typically have their own technique-specific issues, such as limited operating ranges or severe impact on the sample itself [24]. S-NVM provides high spatial resolution and sensitivity and is therefore suitable for studying 2D magnetism at the nanoscale. Moreover, it provides quantitative information about the arising stray field and can be operated in the full relevant temperature range without significant perturbation of the magnetic sample [25]. S-NVM has been successfully applied to several 2D magnetic systems. For instance, it has been used to study the unusual interlayer coupling in CrI_3 [26] or the domain pattern arising from a magnetic Moiré pattern [27], demonstrating the great potential of S-NVM in the field of 2D magnetism.

This thesis explores the possibility of using S-NVM to study 2D magnetism in greater detail. The advantages and limitations of the technique regarding sensitivity, spatial resolution, and operating regime are discussed. Following this assessment, it is demonstrated, how this technique can be used to shine light on the unusual coexistence of magnetic order in single-layer $EuGe_2$ and on the origin of the exchange bias in a $MnPS_3/Fe_3GeTe_2$ heterostructure.

Chapter 2 introduces the NV center and its basic properties. First, its electronic structure is presented and how its spin triplet ground state can be used as a spin qubit. Next, the fundamentals and various experimental schemes of NV magnetometry are shown. Finally, it is discussed how to embed the NV in a scanning setup and how it can be applied to record an image of the magnetic stray field of a sample.

Chapter 3 discusses S-NVM as a tool for studying 2D magnetism. It starts with a short introduction to the topic and the main characterization tools. Since the NV center records the stray magnetic field, it is shown how such a stray field map can be related to a 2D magnetic source. Because this inverse problem does not have a general solution, the additional constraints and assumptions required to infer the magnetization from the stray field signal are discussed. During this discussion, the spatial resolution and sensitivity of S-NVM with respect to a 2D magnetization are defined. Next, the operating regime of S-NVM is examined. Although S-NVM can operate at the temperatures relevant to 2D magnetism, its magnetic field range is limited to external fields applied parallel to the NV axis. The low ordering temperature of

2D magnets requires the implementation of S-NVM in a cryostat, the description of which concludes this chapter.

Chapter 4 presents S-NVM data on single-layer $EuGe_2$ grown by molecular beam epitaxy. After describing a patterning process, that allows the realization of a 2D magnet with well-defined lateral geometry, the macroscopic magnetization of $EuGe_2$ is studied by the stray field arising from the geometry edge. The characterization is in agreement with previous macroscopic measurements, but also reveals a local inhomogeneous magnetization, indicating nanoscale disorder of the film. The magnetic texture is further investigated in detail. Both the macroscopic and microscopic magnetization are described in terms of a disordered model based on the general Arrott-Noakes equation and a grain structure with varying critical temperature.

Chapter 5 investigates the origin of the exchange bias in a $MnPS_3/Fe_3GeTe_2$ heterostructure. Although this exchange bias has been observed in several works, its origin is under debate because the ideal $MnPS_3$ surface does not provide trivial pinning sites for the Fe_3GeTe_2. Macroscopic SQUID measurements indicate a phase transition in $MnPS_3$ below the Néel temperature that result in a small magnetic moment. S-NVM confirms the presence of the moment in the few-layer limit, which presents a plausible mechanism for the exchange bias, despite the hysteretic behavior being different between the bulk crystal and the few-layer flake.

This work concludes with a summary of the main results and ends with an outlook into the future: What challenges need to be addressed to fully exploit the potential of S-NVM, and what exciting physics in the field of 2D magnetism might be revealed in the experiments to come?

2. Magnetometry with the Nitrogen-Vacancy Center

The nitrogen-vacancy center (NV) is a point defect in diamond where two adjacent carbon atoms are substituted by a single nitrogen atom. Its negatively charged variant forms a spin triplet ground state, constituting a solid-state spin qubit, particularly advantageous for quantum sensing applications. The spin state is initialized by driving the optical transition of the NV center and is controlled by resonant coherent microwave (MW) fields in the gigahertz frequency range. The photoluminescence (PL) intensity directly correlates with the specific spin state, allowing an all-optical read-out mechanism for its spin state [28]. The fine structure splitting of the different spin states depends on the external magnetic field due to the Zeeman effect. In addition, the high phonon energies in the diamond lattice, due to its high mechanical stiffness, lead to long spin coherence times, allowing a precise and quantitative measurement of the local magnetic field at the NV center [7].

The mechanical stiffness of diamond also enables the nanostructuring of the host material and thus the realization of all-diamond atomic force microscopy (AFM) tips, hosting a single NV center near the apex of the tip [29]. Employing such a tip in a scanning setup, the NV center can be brought close ($\approx 30 - 100\,\mathrm{nm}$) to a magnetic substrate. This setup allows direct imaging of the stray magnetic field of a substrate, achieving spatial resolutions corresponding to the NV-sample distance and a typical static field sensitivity of $1\,\mathrm{\mu T}/\sqrt{\mathrm{Hz}}$. By employing dynamical decoupling techniques, this sensitivity can be pushed to the tens of nanotesla range for alternating magnetic fields [12]. Spin coherence persists over a wide temperature range from millikelvin temperatures [30] to $1000\,\mathrm{K}$ [31]. This broad range allows for nanoscale imaging across various temperature regimes, establishing scanning NV magnetometry (S-NVM) as a powerful tool to study nanoscale phenomena within the field of condensed matter physics [12]. Such phenomena include the breakdown of ohmic transport in graphene [17], the intrinsic structure and dynamics of domain walls [16, 32], non-trivial spin textures in chiral antiferromagnets [15] and skyrmions [33] as well as the interplay between different interlayer couplings in two-dimensional magnets [26, 27].

This chapter elucidates the fundamentals of S-NVM. It begins with a discussion of the atomic and electronic structure of the NV center, followed by a description of its spin state, which forms a suitable spin qubit. Subsequently, it delves into the utility of the NV center for the measurement of external magnetic fields. Finally, this chapter concludes with a description of the integration of the NV center into a scanning setup for nanoscale imaging of magnetic stray fields.

2.1. Nitrogen-Vacancy Center in Diamond

The NV center is a naturally occurring point defect in diamond where two adjacent lattice sites are occupied by a single nitrogen ion and a vacancy. Its symmetry axis aligns along the $\langle 111 \rangle$ or its three equivalent directions and it shares the symmetry of the C_{3V} point group (Fig. 2.1 **a**). The NV center is most commonly created artificially by ion implantation of the diamond lattice with nitrogen ions [34], although this process causes collateral damage to the diamond lattice. High-temperature annealing can mitigate this damage, preserving good optical and spin coherence [35, 36]. Alternative creation methods include delta doping during diamond growth [37], electron irradiation [38] and laser writing [39], the latter facing challenges in producing near-surface NVs required for sensing applications [40].
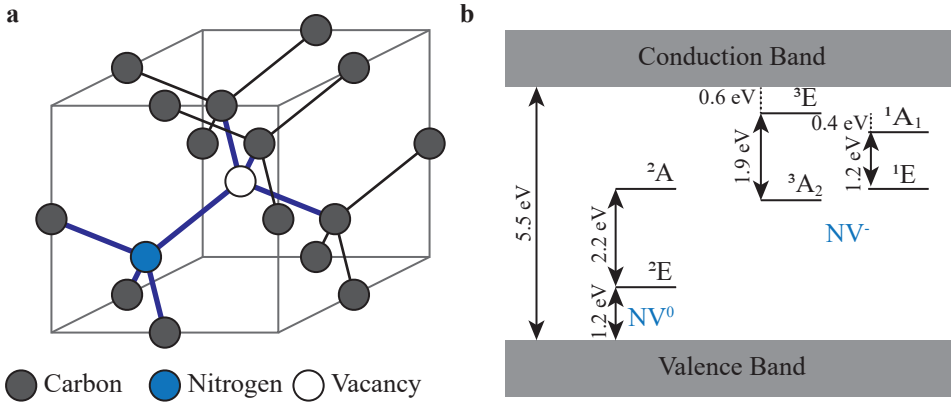
Figure 2.1.: Atomic and Electronic Structure of the Nitrogen-Vacancy Center. a Schematic representation of the atomic structure of the NV center. In the cubic lattice cell of diamond, a single nitrogen ion replaces two adjacent carbon atoms, leaving an additional vacancy in the cell and creating the NV center. The NV center displays the symmetry characteristic of the C_{3V} point group with its symmetry axis aligned along the $\langle 111 \rangle$ direction. **b** The NV center occurs predominantly in the neutral and negatively charged states, the latter being used for sensing applications. Its electronic states lie within the band gap of the diamond. The optical transition $^3A_2 \leftrightarrow {}^3E$ is utilized for optical readout and spin state initialization by spin-selective intersystem crossing to the singlet state $^1A_1 \leftrightarrow {}^1E$. The negatively charged NV$^-$ can be converted to the neutral NV^0 by two-photon ionization, while a two-photon process enables the absorption of an electron from the valence band, restoring the NV$^-$ state (adapted from [41]).

The NV center exists in several stable charge states, primarily the neutral NV^0 and the negatively charged NV$^-$, both residing within the diamond band gap (Fig. 2.1 **b** [41]). The NV$^-$ is used for sensing purposes and henceforth referred to as the "NV center" unless otherwise specified. Switching between charge states occurs via double-photon ionization [42] and is detrimental for sensing applications for two reasons: First, it compromises the optical and spin coherence due to

additional relaxation channels, and second, the average time in the NV^0 state represents a dead time for the measurements. Consequently, stabilization and control of the charge state are crucial for the utility of the NV center in sensing applications [43, 44].

The negatively charged NV center comprises six electrons in the unfilled electron shell, three electrons from neighboring carbon sites, two from the nitrogen, and one from the surrounding environment. Its electronic structure is deduced by optical spectroscopy [41], ab-initio calculations [45], and group theoretical considerations [46]. The electronic structure is described by the nomenclature of the C_{3V} symmetry group: The ground state is the spin triplet $^3A_2$, optically excitable into the two ^3E states and their respective phonon side bands. The NV center emits a broad PL spectrum between $\lambda = 640 - 800$ nm with a zero-phonon line at 637 nm and a radiative lifetime of 12 ns. According to Hund's rules, the singlet spin state ^1E is energetically about 0.4 eV relatively higher than the triplet state. Its radiative transition $^1A_1 \rightarrow {}^1E$ occurs at a photon wavelength of 1040 nm. The spin-dependent intersystem crossing between the singlet and the triplet state forms the basis for the spin-dependent PL of the NV center and its advantageous properties for quantum sensing purposes, detailed in the subsequent section.

2.2. Nitrogen-Vacancy Center as Spin Qubit

The electronic fine structure of the NV center, coupled with its spin-dependent photophysics and long spin coherence times make the NV center a solid-state spin qubit suitable for quantum technologies.

The level structure of the NV center encompasses a spin triplet in the ground state and two spin triplets in the excited state (Fig. 2.2 **a**). The ground state exhibits no angular momentum, and hence the observed zero-field splitting of $D_{gs} = 2.87$ GHz is mainly attributed to spin-spin interactions [28]. Due to the nuclear magnetic moment of the nitrogen isotopes ^{14}N ($I = 1$) and ^{15}N ($I = 1/2$), the fine structure levels also show a hyperfine splitting, resulting in three and two optically allowed transitions within the fine structure ground state, respectively [47, 48]. In the excited state, the two degenerate spin triplets are split into three doublets due to spin-orbit coupling, while the degeneracy of the uppermost doublet is broken by spin-spin interactions. Lattice vibrations couple the orbital degrees of freedom in the excited state and induce temperature dependent orbital averaging. At room temperature, the doublet structure behaves like an effective spin triplet state with zero-field splitting $D_{es} = 1.42$ GHz [49, 50].

The spin-dependent PL and the all-optical spin initialization arise from a spin-dependent intersystem crossing (IC) of the triplet states with the singlet state. Upon optical excitation, the ^3E state exhibits two decay paths: direct optical decay to the $^3A_2$ state (spin-conserving) leading to PL, and non-radiative decay to the singlet state ^1A via spin-dependent IC, which occurs preferentially for the states $\langle m_S = \pm 1|$. Subsequent radiative decay from ^1A to ^1E and non-radiative decay to the ground state $^3A_2$ complete the latter decay path. The overall spin dynamics can be modeled by an effective 5-level system where the singlet state serves as a shelving state. A $\approx 30\%$ optical contrast and close to 90% all-optical spin polarization stem from
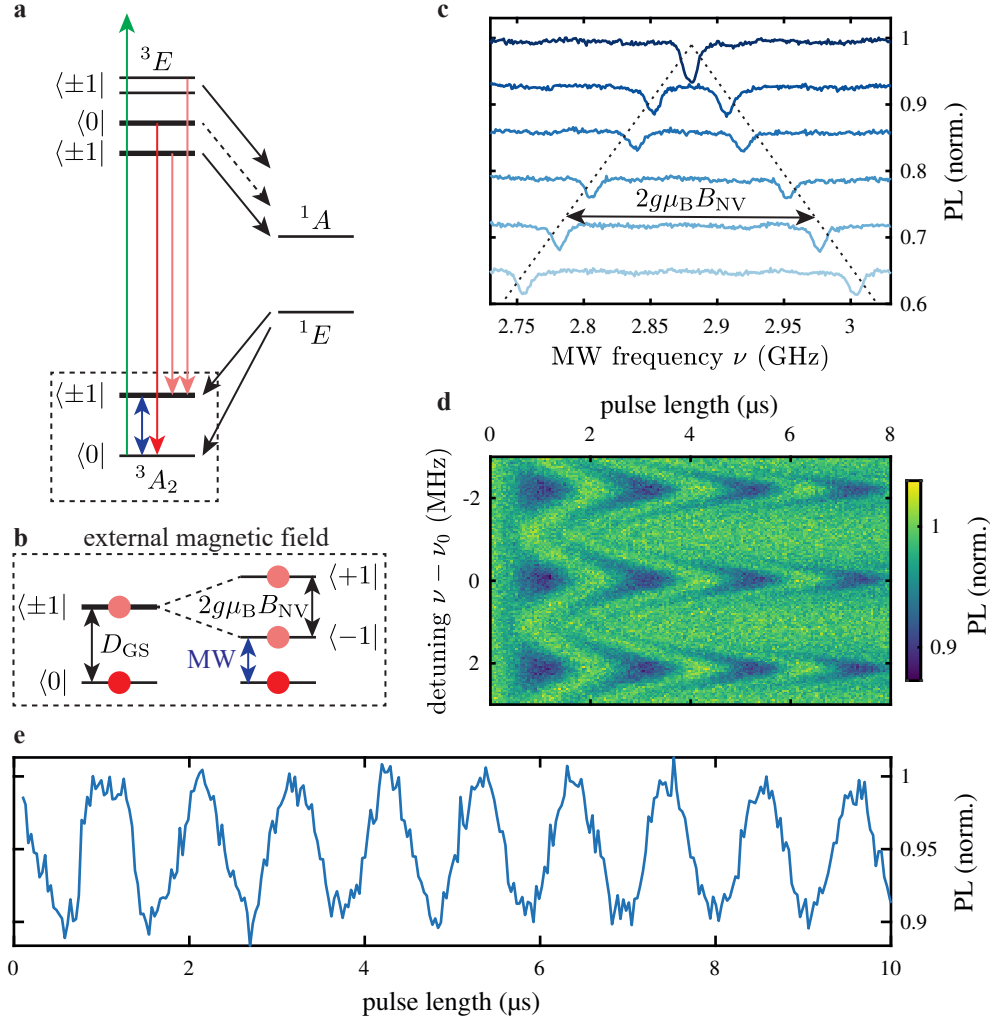
Figure 2.2.: The Nitrogen-Vacancy Center as Spin Qubit. a Fine structure of the NV$^-$. The ground state is a spin triplet with zero-field splitting 2.87 GHz. The excited state consists of two triplet states split by spin-orbit coupling. Spin-dependent intersystem crossing to the singlet state leads to optical spin initialization and spin-dependent PL. **b** In an external field, the ground state shows a Zeeman splitting of the $\langle \pm 1 |$ state proportional to the field along the NV axis B_{NV}. **c** The spin-dependent photophysics allows the determination of B_{NV} by an optically detected magnetic resonance (ODMR) experiment. **d** In a non-zero field, the spin triplet can be approximated by a two-level system that can be coherently controlled by resonant MW fields, allowing Rabi oscillations to be driven, resulting in the Chevron pattern shown. **e** The NV center exhibits excellent spin coherence, allowing Rabi oscillations to be driven by pulse lengths $\gg 10\,\mu\mathrm{s}$.

the spin-dependent IC probability of the excited state and the relatively long lifetime of the singlet state compared to the optical lifetime of the triplet state [51].

At zero field, the upper spin levels $\langle \pm 1|$ of the ground state are degenerate, but an external field splits them according to the Zeemam effect (Fig. 2.2 **b**). The ground state spin levels of the NV are described by the Hamiltonian

$$
\begin{aligned}
\hat{H}_{\mathrm{gs}}/h &= D_{\mathrm{gs}} \left(\hat{S}_z^2 - 2/3 \right) + g\mu_{\mathrm{B}} \boldsymbol{B} \cdot \hat{\boldsymbol{S}} \\
&= D_{\mathrm{gs}} \left(\hat{S}_z^2 - 2/3 \right) + g\mu_{\mathrm{B}} \left(B_x \hat{S}_x + B_y \hat{S}_y + B_z \hat{S}_z \right)
\end{aligned}
\tag{2.1}
$$

where $\hat{S}_i$ represents the various spin operators in the coordinate frame of the NV with $z \parallel$ NV, B_i the component of the applied external magnetic field, g the electronic Landè factor and μ_{B} the Bohr magneton. While B_z induces a linear shift of the upper spin levels with $\gamma_{\mathrm{NV}} = g\mu_{\mathrm{B}} = 28.0\,\mathrm{GHz/T}$, a field perpendicular to the NV couples the different eigenstates resulting in a second-order quadratic Zeeman effect. Because such a coupling between different eigenstates is detrimental to the qubit properties of the NV center, the NV center is typically operated under bias fields parallel to the NV axis [7]. Although the orbital ground state of the NV lacks first-order sensitivity to electric fields or strain due to the absence of spin-orbit coupling, it exhibits a weak dependence on both due to a second-order Stark effect. This results in a slight shift of the zero-field splitting and coupling between different spin levels described by an effective electric-strain field in the Hamiltonian [52]. Additionally, a weak temperature dependence of D_{GS}, following a T^5 scaling, arises from phonon-induced lattice distortion [53, 54]. However, even at room temperature the effect is small ($\partial D_{\mathrm{GS}}/\partial T = -74.2(7)\,\mathrm{kHz/K}$ [55]) compared to the linear Zeeman effect of typical on-axis external magnetic fields.

Coherent resonant MW fields can be used to manipulate the spin of the NV orbital ground state making the NV center a two-level spin qubit. Spin-dependent PL facilitates the determination of the splitting of the upper spin levels via optical detected magnetic resonance (ODMR) spectroscopy: The NV center, continuously illuminated by a green laser, shows a decrease in PL whenever the MW frequency is near-resonant with the ground state level splitting during a frequency sweep. As the splitting is mainly affected by the field parallel to the NV axis B_{NV}, ODMR spectroscopy can be directly used to quantitatively determine the external magnetic field [7] (Fig. 2.2 **c**). Furthermore, resonant MWs can also be used to induce coherent spin manipulations, such as Rabi oscillations, revealing a three-fold Chevron pattern due to the hyperfine interaction with the nuclear spin of ^{14}N (Fig. 2.2 **d**).

The spin coherence, required for coherent manipulation, is limited by the longitudinal spin relaxation time T_1 and the transverse spin relaxation T_2^* or T_2. The former describes the spontaneous transition between the spin sublevels and is ultimately limited by the spin-phonon interaction, but can exceed several seconds at cryogenic temperatures [56]. The latter describes the dephasing of the spin state due to local fluctuating magnetic fields in the environment, such as neighboring nuclear and defect spins or electric charge noise, and sets the time scales available for coherent spin manipulations. For the NV center T_2^* up to the millisecond range are reported [57], which can be extended by dynamical decoupling to T_2 times into the second range [56] ultimately limited by the longitudinal spin relaxation time $T_2 < 2 \cdot T_1$. The combina-

tion of optical initialization, spin readout, and extended coherence times renders the NV center a solid-state qubit suitable for quantum technologies.

2.3. Magnetometry with the Nitrogen-Vacancy Center

The linear Zeeman splitting of the spin of the NV center, combined with its spin properties, enables the determination of the stray magnetic field B_{NV} along the NV axis. The magnetic field sensitivity η_{DC} for a single NV center depends on the longitudinal spin relaxation time T_2^*, the detected PL intensity I_0, and the PL contrast between the different spin states C. Typically, sensitivities down to $\mu\mathrm{T}/\sqrt{\mathrm{Hz}}$ can be achieved [7].

The most common measurement scheme for magnetic field determination is continuous-wave (cw) ODMR. In this scheme, the NV is continuously excited by a green laser and read out from its PL while a cw MW source drives the NV spin (Fig. 2.3 **a, i**). At resonance, the MW driving is most efficient, resulting in the largest relative population of the spin states $\langle\pm 1|$, leading to a minimum PL intensity (Fig. 2.3 **b**). The PL intensity I as a function of the MW frequency ν can be written as

$$I(\nu) = I_0 \left(1 - C\mathcal{F}\left(\frac{\nu - \nu_0}{\Delta\nu}\right)\right) \tag{2.2}$$

with the undriven PL intensity I_0 and the functional lineshape $\mathcal{F}$. A change in the magnetic field ΔB along the NV axis induces a frequency shift $\Delta\nu = \gamma_{\mathrm{NV}} \cdot B_{\mathrm{NV}}$. Assuming photon shot-noise $\Delta I = \sqrt{I_0}$ in the measurement interval Δt, the sensitivity η_{DC} is given by the change in magnetic field resulting in an intensity difference identical to the photon shot-noise:

$$\begin{aligned}\eta_{\mathrm{DC}} &= \Delta B\sqrt{\Delta t} = \frac{\Delta I \sqrt{\Delta t}}{|\partial I/\partial B|_{\mathrm{max}}} \\ &= \frac{4}{3\sqrt{3}} \cdot \frac{h}{g\mu_{\mathrm{B}}} \cdot \frac{\Delta\nu}{C\sqrt{I_0}},\end{aligned} \tag{2.3}$$

where the last expression is valid for a Lorentzian line shape. Notably, this sensitivity is given at the maximum slope of the line [58] and depends on three NV-specific parameters: the linewidth $\Delta\nu$, the detected PL intensity I_0, and the PL contrast C.

The width of the resonance $\Delta\nu$ is fundamentally limited by the spin dephasing time T_2^*, a limit that is typically not reached in cw ODMR, because for optimal sensitivity the linewidth is broadened equally by the optical power, the MW power, and the spin dephasing. However, more advanced measurement protocols can approach this limit [59]. Pulsed ODMR overcomes power broadening by separating the optical excitation and the MW driving [58]. In this scheme, the spin state is first initialized to the state $\langle 0|$ with a green laser pulse. A coherent MW π-pulse transfers the spin to the state $\langle\pm 1|$, which is read out by a second laser pulse (Fig. 2.3 **a, ii**). Optimal sensitivity is achieved when the readout and initialization pulse durations are set to the singlet lifetime ($\approx 300\,\mathrm{ns}$), and the MW pulse length is set to T_2^* [59]. However, if $1/T_2^*$ exceeds the hyperfine splitting of the NV, the π-pulse cannot drive all states simultaneously, resulting in a decrease in optical contrast (Fig. 2.3 **c**). This is mitigated
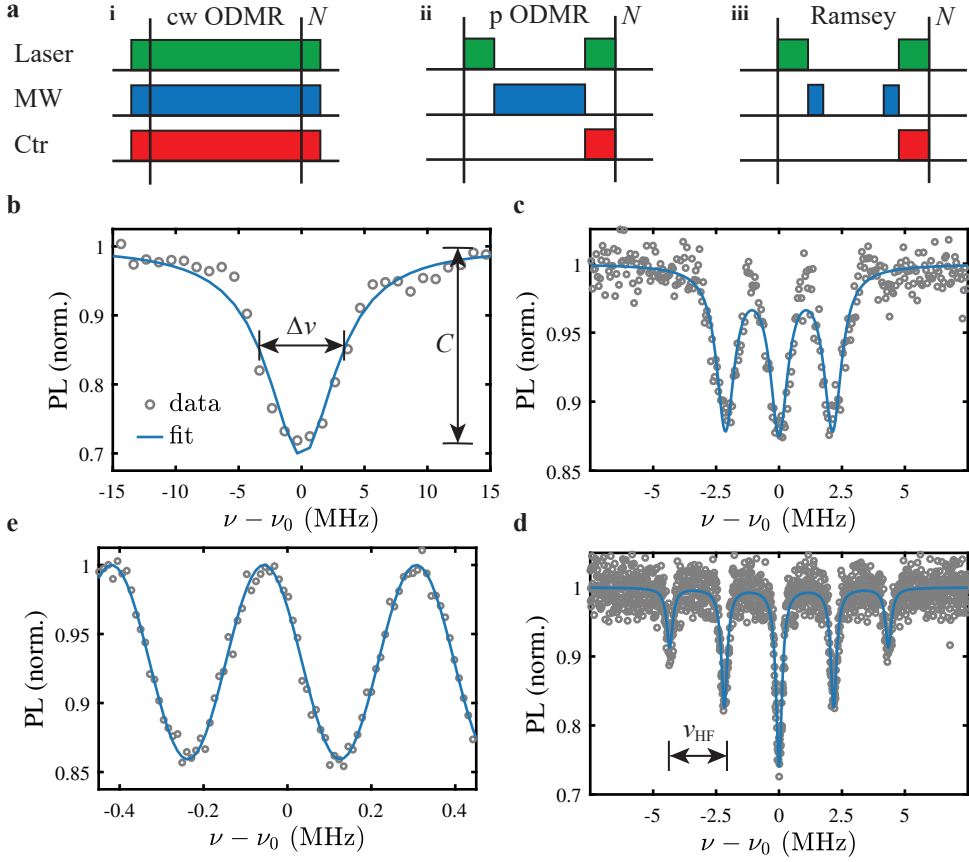
Figure 2.3.: Magnetometry with the NV Center. a The three different pulse sequences to determine the resonance frequency of the spin triplet: continuous-wave ODMR, pulsed ODMR, and the Ramsey sequence. **b** cw ODMR spectrum of a strongly driven NV center. The PL is normalized to the undriven NV. The magnetic field sensitivity is given by the PL intensity, the spin contrast C, and the full width at half maximum of $\Delta\nu$. **c** Hyperfine-resolved pulsed ODMR spectrum. **d** Simultaneous driving of all three hyperfine levels with a three-tone MW field where the splitting between the tones is equal to the hyperfine splitting ν_{HF}. **e** PL spectrum for a typical Ramsey experiment.

by multitone driving of all hyperfine states with a MW cone, where the frequency components are split by the frequency of the hyperfine splitting [60, 61] (Fig. 2.3 **d**). This increases the sensitivity of pulsed ODMR to approach the sensitivity of Ramsey spectroscopy.

In the Ramsey protocol, after spin initialization, a superposition between the states $\langle 0|$ and $\langle \pm 1|$ is created by a $\pi/2$-pulse. During the interrogation time, a field-dependent phase difference between the superposition state accumulates. This phase difference is translated into a population difference by a second $\pi/2$-pulse, which is

read out by a second laser pulse (Fig. 2.3 **a, iii**). For optimal sensitivity, the state preparation time should be minimal, requiring high MW driving powers and a short $\pi/2$-time, and the interrogation time between MW pulses should be long to allow a long accumulation of a field-induced phase difference. As the spin dephases, the contrast diminishes, and the optimal interrogation time is set by $T_2^*/2$, resulting in the optimal combination of PL oscillation frequency as a function of field-induced detuning and optical contrast for field sensitivity [59] (Fig. 2.3 **e**). Despite the high sensitivity of the Ramsey protocol, pulsed ODMR and cw ODMR are preferred in scenarios where the highest sensitivity is not required. Due to their more pronounced single resonance, it is easier to track the resonance at moderate field strengths, providing a higher dynamic range for field measurements.

2.4. Scanning Nitrogen-Vacancy Magnetometry

The NV center, due to the Zeeman splitting of the ground state and its favorable spin properties, is well-suited for sensitive magnetometry. Additionally, the spatial extent of the electronic wavefunction of the center, confined to a few carbon sites and below the nanometer range, inherently provides highly local information about the stray field component that can be utilized for nanoscale magnetic imaging [12]. However, in a magnetic source-free space above a magnetic surface, the stray field components decay exponentially $\propto \exp(-kz)$, while the distance z increases for a spatial frequency k [62]. As a result, the spatial resolution is determined less by the physical nature of the NV center itself and more by the distance between the NV center and sample d_{NV}, ultimately limiting the spatial resolution [7].

For S-NVM, a single NV center is typically embedded in an AFM tip to bring the NV center close to an atomic surface. To confine the NV center near the apex of the AFM tip, all-diamond cantilevers can be fabricated from diamond membranes with shallowly implanted NVs (depth $\approx$ 5-10 nm) [29]. Such a diamond tip can be seen as a photonic structure requiring a minimum base diameter of 200 nm to enable the excitation of the NV center by a confocal laser spot. Furthermore, the shape can be engineered to facilitate the collection of the PL emitted from the NV. The highest collection efficiencies have been achieved by conical [63] or parabolic tip designs [64], providing high collection efficiency, a small numerical aperture of the emission, and spatial resolutions of 30-100 nm. Such a cantilever can be integrated into a conventional AFM system, allowing the scanning of the NV center in close contact over a magnetic substrate, while optical access for spin initialization and readout is provided by a confocal setup. Spin manipulations are performed by a nearby external MW antenna (Fig. 2.4 **a, b**[1], details in Appendix A.1).

To record the stray magnetic field of a substrate, the NV spin resonance frequency needs to be recorded while scanning across the substrate. The most straightforward approach is to record a full ODMR or Ramsey spectrum (as shown in Fig. 2.3) at each pixel (Fig. 2.4 **d**). However, a full spectrum contains frequency components that are insensitive to magnetic field changes, thereby deteriorating the magnetic field sensitivity compared to the sensitivity at the maximum slope of the spectrum. Alternatively, modulation of the MW driving frequency can be used to generate two

---

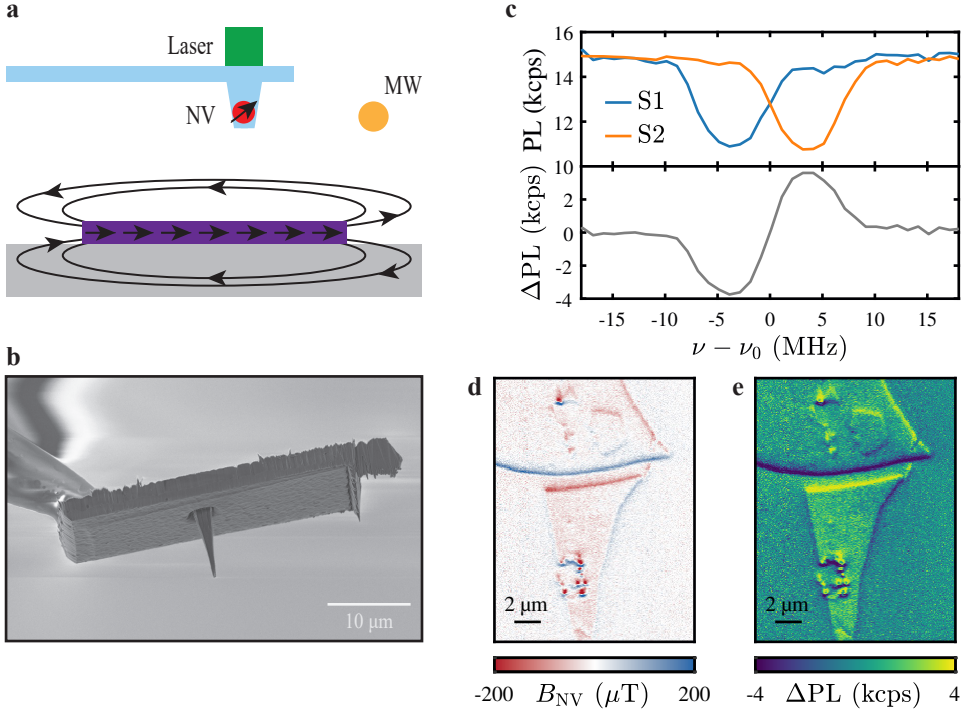[1]the SEM image of the cantilever is provided by J. Happacher

Figure 2.4.: Principles of Scanning Nitrogen-Vacancy Magnetometry.
a Schematic of S-NVM: An all-diamond tip with a single NV center at its apex is brought into close contact with a magnetic substrate. A confocal geometry is used to excite the NV and collect its PL while a nearby external antenna ($\approx 100\,\mu m$ distance) transmits the MW for coherent driving. **b** Scanning electron microscope image of an all-diamond cantilever tip. **c** ODMR spectrum as used for magnetometry: Two signals S1 and S2 are generated by two MW signals offset by $\nu_{S2} - \nu_{S1} = 8\,MHz \approx \Delta\nu$ (top), the difference of the signals can be used as an error signal to track the resonance frequency (bottom). **d** Determination of the resonance frequency at each pixel allows imaging of the stray field of a magnetic sample quantitatively. Here, the stray field arising from a two-dimensional $CrCl_3$ flake is depicted. A homogeneous magnetization creates a stray field only at the edge of the flake (Section 3.3.1). **e** The measurement of the PL at a fixed frequency allows a fast qualitative imaging. Here, the simulation of the PL difference resulting from the stray field in d and the ODMR spectrum in c is shown.

separate MW signals shifted by $\pm\Delta\nu/2$ and subsequent separate readout of the two channels allows the generation of an error signal with its maximum slope centered around the resonance frequency (Fig. 2.4 **c**). By doing so, a fast magnetic image can be recorded without the need to sweep the MW frequency, merely evaluating the PL of the NV (Fig. 2.4 **e**). Although this method can in principle be used to quantitatively infer the stray magnetic field in the linear regime of the error signal, it is primarily used for qualitative imaging with a dynamic range set by the width of the electron

spin resonance. However, the error signal can also be used for a proportional-integral-derivative (PID) feedback loop in which the driving frequency is adjusted according to ΔPL, ensuring that the central MW frequency always equals the resonance frequency of the NV spin [65]. This enables the quantitative determination of the stray magnetic field with the maximum sensitivity of the slope of the ODMR/Ramsey spectrum. Additionally, the switching of the readout acts as a high-pass filter for magnetic noise. Noise with a frequency lower than the switching frequency affects both counters equally and is thus averaged out. Consequently, modulated feedback-based determination of the resonance frequency stands out as the superior imaging method for stray magnetic field maps.

2.5. Summary and Outlook

This chapter has elucidated the spin-dependent PL and all-optical spin initialization of the negatively charged NV center in diamond. These phenomena arise from a spin-dependent IC of the triplet state with the singlet state. The linear Zeeman effect, which is mainly dependent on the external magnetic field applied along the NV axis, allows a calibration-free determination of the stray magnetic field. Embedded in an all-diamond AFM tip, a single NV center can be brought into close proximity to a magnetic substrate, enabling nanoscale magnetic imaging with a field sensitivity of $\mu T/\sqrt{Hz}$ and a spatial resolution of a few tens of nanometers. S-NVM has thus emerged as a powerful tool for studying magnetism at the nanoscale.

The ongoing development of S-NVM involves optimizing sensitivity, spatial resolution, and the exploration of novel measurement protocols to expand its applicability to diverse research areas. Examining Eq. (2.3), sensitivity improvement requires reducing the ODMR linewidth, enhancing the PL count rate, and maximizing the spin contrast. The spin coherence times fundamentally constrain the linewidth, which is predominantly reduced by magnetic and electrical noise from nearby defects. Major defect sources are lattice damage from the nitrogen implantation process for NV creation and surface irregularities from the diamond tip fabrication. While the former can be mitigated by less invasive creation methods such as carbon implantation [66] or post-treatments such as high temperature annealing protocols [35, 36], the latter is addressed by surface treatments such as oxygen annealing for well-defined surface termination [67]. Surface termination also stabilizes the charge state [43, 68], which is crucial for high optical contrast. The charge state can also be stabilized by introducing electron donors into the diamond material, such as phosphorus doping [69]. Improving the PL count rate involves photonic engineering of the diamond environment [64] or optimizing the collection optics. A promising avenue is transitioning from a confocal setup to a fiber-based collection path [70]. Enhancing spatial resolution can be achieved by creating shallower NVs, which reduces the distance between the diamond surface and the NV, and overall reduces the distance to the host material [71]. However, shallower NVs are also more susceptible to surface defects and band bending, which deteriorate the charge stability and coherence times. Sharper photonic structures compared to the commonly used truncated pillar geometry, such as diamond pyramids, can also reduce the stand-off induced by the AFM tip geometry [72]. Complementary to sensor improvements, optimizing the measurement

protocols is an additional route for improving S-NVM. A particularly interesting route is to convert the static magnetic signal to an alternating magnetic signal, allowing the application of dynamical decoupling sequences and exploiting significantly extended spin coherence times T_2. Modulating the magnetic source is a simple experimental approach [18], but it is limited to appropriate sources. Alternatively, synchronizing the oscillatory movement of the AFM tip and the readout of the signal at the AFM frequency also converts the static magnetic signal to an alternating signal [73]. Accelerating the determination of the resonance frequency by real-time statistical methods compared to conventional feedback protocols during the scanning process is another viable avenue [74, 75].

While further enhancements in S-NVM are anticipated, the method has already been successfully applied to various questions in the field of magnetism [12]. The next chapter explores the potential of this imaging tool in the context of two-dimensional magnetism.

3. Nanoscale Imaging of 2D Magnetism

Layered two-dimensional (2D) van der Waals (vdW) materials typically consist of single atomic layers that are strongly covalently bonded, while multiple layers are stacked via weak vdW forces. Mechanical exfoliation then allows for the isolation of a single atomic layer. As the properties of these materials change dramatically between their bulk counterpart and their 2D limit, they give rise to novel physical phenomena and unprecedented physical properties, such as the remarkable high carrier mobility in graphene [76]. Moreover, the vdW nature of the interlayer coupling enables the stacking of several different 2D materials with atomically clean interfaces, resulting in novel heterostructures with unique properties [77]. The discovery of ferromagnetic order in these materials down to the monolayer limit [21, 22] opens the prospect of studying magnetism in a reduced dimension and extends the concept of vdW heterostructures to the field of spintronics [78]. Thus, the study of 2D magnetic materials holds great promise for both fundamental research and future advances in the field of spintronic devices.

This chapter discusses the fundamental concepts of 2D magnetism. It will be shown that the limited toolset for nanoscale characterization requires further development of novel experimental techniques, such as scanning nitrogen-vacancy magnetometry (S-NVM), to provide quantitative nanoscale information about these materials. To this end, it is first discussed how information about the magnetization can be derived from the stray magnetic field. The expected spatial resolution and sensitivity of S-NVM are discussed with respect to 2D magnetizations. Finally, the possibilities and limitations of the operating regime of S-NVM are described, while the challenges of integration into a cryogenic system are briefly discussed.

3.1. Fundamentals of 2D Magnetism

Magnetic order arises from interacting neighboring spins $\hat{\boldsymbol{S}}_{\boldsymbol{r}}$ at the lattice site $\boldsymbol{r}$, which form an ordered spin arrangement below a critical temperature T_{c}. In the case of pure Heisenberg exchange coupling, such a system is described by the Hamiltonian

$$\hat{H} = -2 \sum_{|\mathbf{r}-\mathbf{r}'|} J\hat{\boldsymbol{S}}_{\boldsymbol{r}} \cdot \hat{\boldsymbol{S}}_{\boldsymbol{r}'}. \tag{3.1}$$

While a positive exchange constant $J > 0$ favors parallel alignment of the spins and thus ferromagnetic (FM) ordering, $J < 0$ favors antiparallel alignment and antiferromagnetic (AFM) ordering of the spins [79]. Depending on the spin dimensionality[1],

---

[1]the spin dimensionality is not necessarily identical to the lattice dimensionality and describes the number of degrees of freedom for the spin direction

several magnetic models are distinguished: In the Ising model the spin is confined along a single direction, while in the XY model the spin is confined in a specific plane, and in the Heisenberg model the spin can rotate freely along all three directions [80]. The spin model determines the spin wave spectrum, resulting in a characteristic critical behavior toward T_c, that is approximately described by a power law behavior [81]. For example, the temperature dependence of the spontaneous magnetization M in the absence of an external magnetic field is given by

$$M(T) = M_0 \left(\frac{1}{T - T_c} \right)^{\beta} \tag{3.2}$$

with a proportionality constant M_0 and a critical exponent β. This formalism can be extended to include the stabilizing effect of an external magnetic field B_{ext}, leading to the so-called Arrott-Noakes equation of state

$$\left(\frac{B_{ext}}{M/M_0} \right)^{1/\gamma} = a \left(\frac{T - T_c}{T_c} \right) + b \left(\frac{M}{M_0} \right)^{1/\beta} \tag{3.3}$$

with the empirical parameters a and b, and the additional critical exponent γ, describing an FM system near its critical temperature [80, 82]. The critical exponents are characteristic of the different spin Hamiltonians and allow to distinguish different spin models by a careful analysis of the scaling parameters for a material system, thus providing important information about the underlying physics [83].

For 2D lattices with continuous symmetry, the spin wave spectrum is gapless, and due to the non-zero spin wave density of states, long-range magnetic order is destroyed even at $T = 0$, prohibiting long-range FM order for 2D magnets described by the Heisenberg [84] or planar XY model [85], commonly referred to as the Mermin-Wagner theorem. In 2D crystals with broken continuous symmetry, the spin-wave spectrum shows a non-zero energy gap that allows stable FM order [86]. The symmetry can be broken intrinsically by magnetocrystalline anisotropy, which introduces a uniaxial magnetic anisotropy axis favoring spin alignment along the out-of-plane axis, as in the case of the 2D vdW magnet CrI_3 [21], or along a specific in-plane axis, as in the 2D vdW magnet CrSBr [87, 88]. Additionally, the symmetry can be extrinsically broken by an external magnetic field, introducing an effective anisotropy axis via the Zeeman energy of individual spins that can stabilize FM order [22]. In addition, finite-size effects can also stabilize the FM order by limiting the magnon density of states, allowing FM order even for micron-sized flakes in systems with continuous symmetry [89]. The resulting FM order of such 2D magnetic systems is generally thermodynamically less stable, leading to a decrease in T_c compared to their 3D bulk counterparts. This results in a layer dependent T_c in the few layer limit [90].

In addition to the layer dependence of magnetic properties, 2D magnetic systems offer a plethora of possibilities to manipulate their properties, allowing the creation of novel spin textures or the realization of new spintronic devices [91]. The properties can be controlled by external means, such as mechanical pressure [92, 93], or electric fields, influencing the magnetic order either by an intrinsic magnetoelectric effect [94] or by electrostatic doping [95, 96]. Additionally, the vdW nature of many 2D magnets allows for the controlled stacking of different layers with atomically smooth interfaces, enabling the tuning of properties by the stacking order [97] or by twisting the orientation of two successive layers [98, 99]. Moreover, the vdW nature enables the stacking

of different materials, allowing both the tuning of the magnetic properties, for example by the proximity effect [100] or by exchange bias [101], and the realization of novel heterostructures where the material is iterated with even single layer variation, offering exciting prospects for novel electronic and spintronic devices [23].

In addition to understanding and manipulating the basic magnetic properties of 2D magnets, their magnetic behavior at the nanoscale is of both fundamental interest and importance for future device applications. One area of particular interest is the study of magnetic domains and domain walls: The evolution of domains in an external field provides insight into the mechanisms of magnetic phase transitions [102] and reveals defects that act as pinning sites for the magnetic domain walls [103]. Moreover, the character of a domain wall (Bloch or Néel type) and the domain wall width are indicative of the fundamental spin interactions of the system and give rise to fundamental micromagnetic parameters such as the exchange stiffness or the magnetocrystalline anisotropy [32]. Understanding domain reversal is also crucial for understanding the switching of the magnetization state, a fundamental mechanism in magnetic memory technology [104].

Additionally, 2D vdW magnets can also host non-trivial chiral spin textures resulting from antisymmetric exchange interactions, such as the Dzyaloshinskii-Moriya interaction (DMI). While DMI is a key ingredient for stabilizing chiral spin textures, it is a rare property in most 2D vdW magnets. Non-trivial topologically protected skyrmionic bubbles have been observed in $Cr_2Ge_2Te_6$ arising from a complex interplay between dipolar interactions, uniaxial anisotropies, and external magnetic fields [105]. However, DMI can be induced in heterostructures where a 2D vdW magnet is brought into contact with a heavy metal material, such as transition metal dichalcogenides. For example, stripe-like domain structures and skyrmion lattices have been observed in a WTe_2/Fe_3GeTe_2 system [106].

The stacking of different vdW materials also allows to twist of the crystallographic orientation of these layers with respect to each other, resulting in so-called Moiré superlattices with a periodicity on the order of a few to tens of nanometers, depending on the twist angle. Since the stacking order varies with the periodicity on the Moiré lattice, the energetic landscape is modulated by a change in the interlayer coupling, giving rise to long-range correlations and novel, non-trivial phases [107]. It has been shown that in the 2D vdW magnet CrI_3, the locally varying stacking order leads to a magnetic superlattice consisting of alternating AFM and FM domains [27]. Similarly, a multistep hysteresis loop in a twisted bilayer has been reported in CrSBr, suggesting anomalous domain formation in such a heterostructure [99].

The diverse possibilities to manipulate the magnetic properties of 2D vdW magnets, together with the clean interfaces they provide between subsequent stacked layers, make them exciting candidates for advances in the field of spintronics [78, 108]. A promising model system are vdW magnets with FM intralayer coupling and tunable interlayer coupling, such as CrI_3 and $CrCl_3$, which exhibit giant magnetoresistance for electrons tunneling vertically through the stacked layers [109, 110]. This magnetoresistance can be used to realize logic devices based on the magnetic state of the vdW magnet, leading to the first demonstration of a spin tunneling field effect transistor based on 2D vdW magnets [111]. Additionally, changes in magnetic properties in vdW heterostructures by the proximity effect can provide electronic control of their magnetic state. The proximity effect of CrSBr on a Fe_3GeTe_2/Pt heterostructure al-

lows spin-orbit torque switching of the FM Fe_3GeTe_2 at zero external magnetic field, adding interesting new functionalities to the field of 2D vdW spintronics [112].

Despite their great prospects in the field of spintronics, the scalability of 2D vdW magnets poses a major challenge for the integration of these materials into working devices. While mechanical exfoliation typically results in micron-sized flakes with ill-defined geometry, scalable growth techniques such as chemical vapor deposition or molecular beam epitaxy result in materials with high defect densities diametrically opposed to the clean interfaces promised by the vdW nature of these materials [113]. Therefore, characterization tools are needed to probe the materials in great detail at the nanoscale, and to provide a deeper understanding of this novel and exciting form of magnetism.

3.2. Imaging Methods for 2D Magnetism

Nanoscale imaging methods for 2D magnetism serve as essential tools to characterize the fundamental properties of these magnets, to study the aforementioned nanoscale phenomena, and to analyze material quality in terms of spatial homogeneity and defect-induced local disorder. An ideal imaging method provides high spatial resolution, magnetic field sensitivity, direct probing of the magnetization, versatility across various materials, applicability over a wide temperature and magnetic field range to cover the entire magnetic phase space, and non-invasiveness to avoid altering the magnetic properties of the sample during a measurement. Two major classes of imaging methods are optical imaging tools and scanning probe microscopy techniques. Optical methods are limited by diffraction, while the spatial resolution of scanning probe techniques is limited by the sample-to-sensor distance, which typically exceeds the optical resolution [24].

The most basic optical imaging tools rely on the magneto-optical Kerr effect or on magnetic circular dichroism, and extract information from the changes in polarization or intensity of the incident laser beam as a function of the magnetic state of the sample. Such setups are comparatively easy to implement and they allow for fast qualitative characterization of 2D magnets, providing insight into fundamental magnetic properties of the material, such as the magnetic field dependent interlayer coupling in CrI_3 [21] or the electric field switching of its magnetic state [114]. Despite the diffraction-limited spatial resolution, optical methods allow experiments with high temporal resolution, for example in a pump-probe configuration spin dynamics have been studied in the picosecond range [115]. An interesting possibility is also offered by X-ray magnetic circular dichroism, because it allows to study the magnetization in an element-specific way, providing information about the constitution of the total magnetization [116, 117]. Other optical methods include Raman spectroscopy, where the magnetic state manifests itself in additional Raman peaks associated with the absorption or emission of spin waves [118], or measurements of the second harmonic generation induced by the breaking of space inversion and time reversal symmetry due to the emergence of magnetic order [88]. Another optical technique is NV widefield magnetometry, in which a diamond membrane with high NV density is brought into contact with a magnetic substrate. Although conceptually similar to S-NVM, this technique relies on an ensemble of NVs, which limits the resolution to the diffrac-

tion limit of the confocal setup and allows only coarse quantitative analysis of 2D magnets [104, 119].

Scanning probe techniques offer spatial resolution down to the nanometer range, limited by the sample-to-sensor distance, exceeding the diffraction-limited resolution of optical imaging techniques. Spin-polarized scanning tunneling microscopy achieves even atomic resolution. This technique requires an atomically sharp tip with a polarized spin at the apex. The tunneling probability of an electron in such a configuration depends on the alignment of the spin of the tip with the underlying magnetization. By that, the stacking-dependent interlayer magnetism of $CrBr_3$ has been directly studied [39]. Although it provides the highest spatial resolution, this technique is restricted to conductive samples and provides only qualitative information about the underlying magnetization. A more flexible technique is scanning superconducting quantum interference device (SQUID) microscopy, in which a nanoscale SQUID is brought close to a magnetic substrate from which it detects the stray magnetic field passing through its SQUID loop. This technique provides high magnetic field sensitivity and has been applied, for example, to image the weak orbital ferromagnetism in twisted bilayer graphene [120]. However, miniaturization of the SQUID loop poses a challenge, limiting the spatial resolution to tens of nanometers. In addition, the SQUID operates only below the superconducting transition temperature, which limits the typical operating range to below $10\,K$. Magnetic force microscopy (MFM) is able to operate over the full relevant temperature and external field range and thus enables the exploration of the full magnetic phase space. A magnetic tip is brought into contact with the sample and the magnetostatic interaction of the tip with the sample provides the imaging contrast. By that, for example, the spin-flip transition of the vdW antiferromagnet $MnBi_4Te_7$ has been studied in detail [121]. Although it offers a large operating range, the calibration of the magnetostatic interaction to extract the underlying magnetization is challenging, and the interaction can severely affect the sample itself, influencing the studied magnetic state.

In summary, various scanning probe techniques are available for studying 2D magnetism, each with its own advantages and drawbacks. S-NVM, with its calibration-free direct measurement of the stray field, low impact on the sample, and flexible operating regime, is an attractive technique for nanoscale imaging of 2D vdW [25]. The details are discussed in the following sections.

3.3. Determination of the Magnetization

In S-NVM, the NV center can directly detect the stray magnetic field along the NV axis B_{NV} emanating from a magnetic surface, such as for example a 2D magnetic system. The stray field can be used to derive information about the underlying magnetization of the sample by direct analysis of the stray field emerging from the edge of the sample or by reconstruction methods.

3.3.1. From Stray Field to Magnetic Source

In general, the magnetic field $\boldsymbol{B}(\boldsymbol{r})$ at a given position $\boldsymbol{r}$ induced by a magnetization $\boldsymbol{M}(\boldsymbol{r})$ is described by the integral equation

$$\boldsymbol{B}(\boldsymbol{r}) = \frac{\mu_0}{4\pi} \int_{\mathrm{d}V'} \left(\frac{3\boldsymbol{M}(\boldsymbol{r}')(\boldsymbol{r} - \boldsymbol{r}')}{|\boldsymbol{r} - \boldsymbol{r}'|^5} (\boldsymbol{r} - \boldsymbol{r}') - \frac{\boldsymbol{M}(\boldsymbol{r}')}{|\boldsymbol{r} - \boldsymbol{r}'|^3} \right) \mathrm{d}V' \tag{3.4}$$

where μ_0 is the vacuum permeability [122]. While S-NVM detects the stray magnetic field, obtaining the magnetization from the stray field requires the inversion of this integral equation. However, there is no general solution to this inversion problem. Nevertheless, specific experimental scenarios constrain the problem sufficiently to allow the determination of $\boldsymbol{M}$ from $\boldsymbol{B}$.

An example of such an experimental scenario is the stray magnetic field arising from an edge (at $x = 0$) of a homogeneous surface magnetization $\boldsymbol{M} = (M, \varphi_M, \theta_M)$ with strength M pointing along the polar angle θ_M and the azimuthal angle φ_M, extending infinitely along the y-axis (Fig. 3.1 **a**, **b**). The magnetic field is then given by [26, 32, 123]

$$B_{\mathrm{x}} = -\frac{\mu_0 M}{2\pi} \cdot \left(\frac{z}{z^2 + x^2} \cos\theta_{\mathrm{M}} + \frac{x}{z^2 + x^2} \sin\theta_{\mathrm{M}} \cos\varphi_{\mathrm{M}} \right),$$
$$B_{\mathrm{y}} = 0,$$
$$B_{\mathrm{z}} = +\frac{\mu_0 M}{2\pi} \cdot \left(\frac{x}{z^2 + x^2} \cos\theta_{\mathrm{M}} - \frac{z}{z^2 + x^2} \sin\theta_{\mathrm{M}} \cos\varphi_{\mathrm{M}} \right). \tag{3.5}$$

The field along the NV axis is obtained by projecting the NV orientation $\boldsymbol{e}_{\mathrm{NV}} = (\varphi_{\mathrm{NV}}, \theta_{\mathrm{NV}})$ with the stray field and the vertical distance equal to the NV-sample distance $z = d_{\mathrm{NV}}$

$$B_{\mathrm{NV}}(x, y) = \boldsymbol{B}(x, y, z = d_{\mathrm{NV}}) \cdot \boldsymbol{e}_{\mathrm{NV}}. \tag{3.6}$$

Using the stray magnetic field arising from such an edge, one can define the sensitivity of S-NVM to detect a certain magnetization η_M. The minimum detectable M is defined as the value of M that produces a stray field equal to the sensitivity limit of the NV center η_B. Since the stray field amplitude decreases with increasing NV distance, the sensitivity η_M depends on d_{NV}. For common NV distances on the order of tens of nanometers, the dependence is approximately linear. For a typical field sensitivity $\eta_B = 1\,\mu\mathrm{T}/\sqrt{\mathrm{Hz}}$ and $d_{\mathrm{NV}} = 50\,\mathrm{nm}$, the sensitivity is equal to $\eta_M = 0.027\,\mu_{\mathrm{B}}/\mathrm{nm}^2/\sqrt{\mathrm{Hz}}$ (Fig. 3.1 **c**), making S-NVM one of the most sensitive imaging tools for 2D magnetic systems [24].

The general Eq. (3.4) can be interpreted as a convolution of the magnetization M with a kernel $\boldsymbol{D}(\boldsymbol{r} - \boldsymbol{r}')$

$$\boldsymbol{B}(\boldsymbol{r}) = \int_{\mathrm{d}V'} \boldsymbol{M}(\boldsymbol{r}') \cdot \boldsymbol{D}(\boldsymbol{r}' - \boldsymbol{r}) \mathrm{d}V' \tag{3.7}$$

implying that the Fourier components of the magnetic field and the magnetization are linked by a tensor multiplication

$$\boldsymbol{B}(\boldsymbol{k}) = \boldsymbol{D}(\boldsymbol{k}) \cdot \boldsymbol{M}(\boldsymbol{k}). \tag{3.8}$$
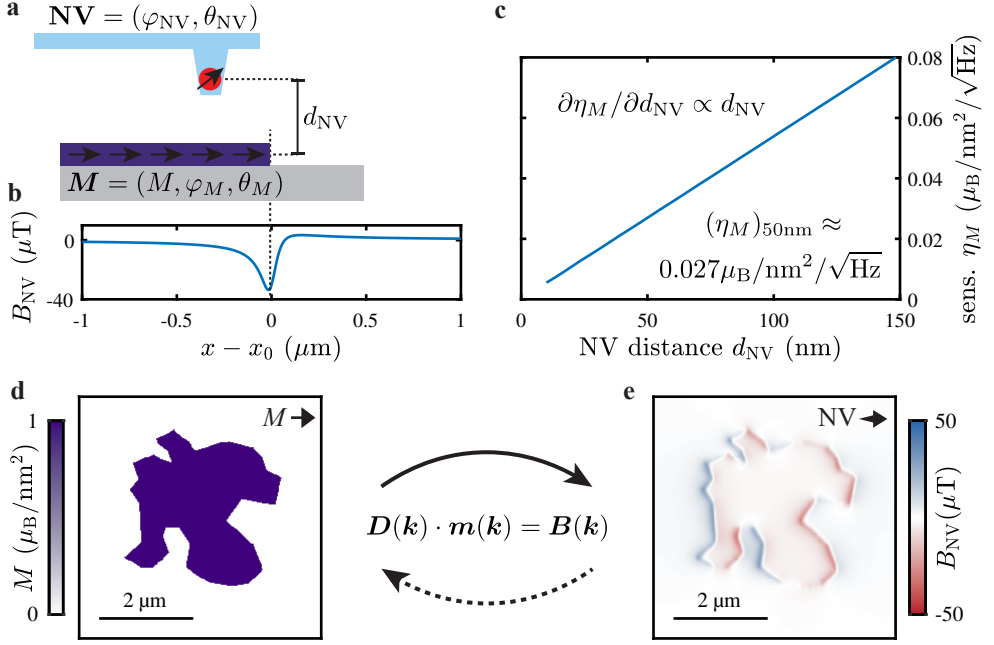
Figure 3.1.: Determination of the Magnetization by S-NVM. a Schematic of the measurement scenario: An NV center is brought into contact with a magnetization at a distance d_{NV} by AFM. **b** Stray magnetic field arising from an edge of a homogeneous magnetization with in-plane orientation. **c** Magnetization sensitivity of S-NVM as a function of d_{NV}, assuming a magnetic field sensitivity of $1\,\mu\text{T}/\sqrt{\text{Hz}}$. The sensitivity is defined as the ability to detect the stray field amplitude of a homogeneous magnetization with a signal-to-noise ratio of one. **d** 2D image of an arbitrarily shaped magnetization of amplitude $M = 1\,\mu_B/\text{nm}^2$ pointing along the in-plane direction as indicated by the arrow. **e** Simulated stray magnetic field as detected by an NV of the common $\langle 100 \rangle$ orientation forming an angle of $\theta_{NV} = 54.7°$ to the surface normal and with the in-plane direction as indicated by the arrow. The stray field is calculated using standard forward propagation techniques.

In the case of a 2D magnetization, the so-called dipolar tensor $\boldsymbol{D}$ can be calculated directly and is given by [33, 123]

$$\boldsymbol{D}(\boldsymbol{k}) = \frac{\mu_0}{2} k e^{-kz} \begin{pmatrix} -\left(\frac{k_x}{k}\right)^2 & -\frac{k_x k_y}{k^2} & -i\frac{k_x}{k} \\ -\frac{k_x k_y}{k^2} & -\left(\frac{k_y}{k}\right)^2 & -i\frac{k_y}{k} \\ -i\frac{k_x}{k} & -i\frac{k_y}{k} & 1 \end{pmatrix} \tag{3.9}$$

allowing the calculation of the stray magnetic field of any given 2D magnetic source (Fig. 3.1 **d, e**).

However, the properties of the dipolar tensor reveal an important restriction for the determination of the magnetization from the stray magnetic field and thus from the data obtained by S-NVM: Although the stray field of a given magnetization can be

calculated directly (also called the forward problem), the rows of the dipolar tensor are not linearly independent. Therefore, the dipolar tensor is not invertible and it is impossible to uniquely determine a general 2D magnetization distribution from a field distribution (also referred to as reverse problem) without additional assumptions. However, in case the orientation of the magnetization is known, it is possible to reconstruct the underlying magnetization pattern, because the tensor equation simplifies to a scalar multiplication for each field component [124].

3.3.2. Spatial Resolution of S-NVM

The dipolar tensor describes how different spatial frequency components of the magnetization contribute to the stray magnetic field signal. From a measurement perspective, it describes the sensitivity of the NV center to a given spatial frequency k at a given sample distance d_{NV}. Consequently, the dipolar tensor allows to define the spatial resolution of S-NVM for the determination of the magnetization.
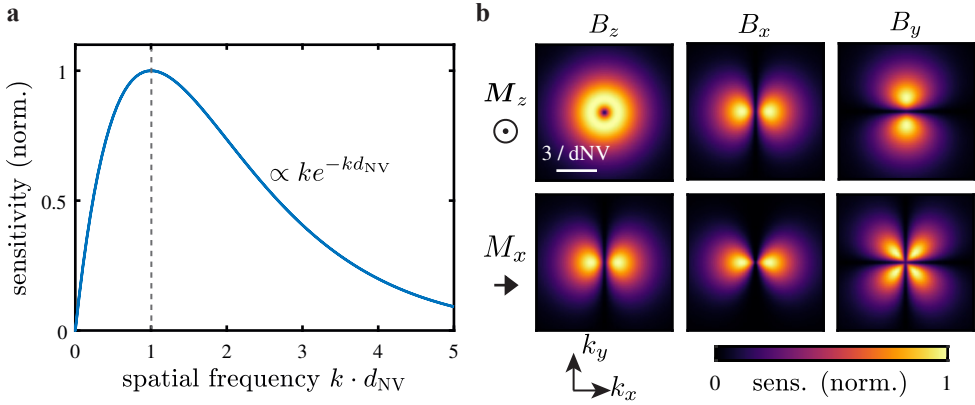

Figure 3.2.: Spatial Resolution of S-NVM. a Prefactor of the dipolar tensor ke^{-kz}, expressed in units of d_{NV}, which indicates the relative sensitivity of S-NVM for a given spatial frequency. The maximum sensitivity is reached for $k = 1/d_{NV}$. **b** The different components of the dipolar tensor, which relate the different components of the stray magnetic field B_i to an out-of-plane and in-plane magnetization M_z and M_x, respectively. The components express a relative sensitivity to a certain spatial frequency and are normalized to their maximum, which is identical for all components.

The prefactor of the dipolar tensor ke^{-kz} acts as a spatial filter: For high spatial frequencies, it describes how the stray field signature decays exponentially with distance (Fig. 3.2 **a**), which reflects the general scaling of the magnetic field in a source-free region (Section 2.4 [62]). For low spatial frequencies $k \to 0$, the sensitivity is linear in k and approaches zero for $k = 0$, because a homogeneous magnetization does not produce any stray field. Consequently, sensors such as the NV center, which directly detect the stray field, are only sensitive to gradients in the magnetization. The maximum sensitivity is reached for $k = 1/d_{NV}$, because higher spatial frequencies

result in stronger gradients, but also decay faster with increasing distance. This maximum is one possibility to define the spatial resolution of S-NVM with respect to a magnetization, which is determined by the stand-off of the NV to the magnetization. Compared to the spatial extent of the NV wavefunction, the stand-off is significantly larger and thus the main limiting factor for the spatial resolution. The stand-off is determined by the depth of the NV center within the diamond tip (typically 5-20 nm for near-surface NVs) and the quality of the AFM contact with the substrate (typically tens of nanometers due to the large tip diameter of 200 nm required for photonic coupling). Overall, a typical stand-off distance of 30-100 nm is achieved, defining the spatial resolution of S-NVM in the field of 2D magnetism.

The various components of the dipolar tensor also describe how different spatial frequencies contribute to a single component of the stray magnetic field (Fig. 3.2 **b**). Besides low spatial frequencies, frequencies along a given in-plane direction produce solely a stray field component parallel to their direction and no stray field orthogonal to it. Additionally, in the case of in-plane magnetizations, spatial frequencies orthogonal to their magnetic direction do not produce any stray field component. This implies that sensors that detect only the stray magnetic field, such as the NV center, are unable to detect the corresponding spatial frequencies of an in-plane magnetization along its orthogonal direction. In general, a divergence-free magnetization does not produce a stray magnetic field, which implies that a given stray field map cannot be assigned to a unique magnetization map. However, the reconstruction of the magnetization from the stray field is possible if, for example, the corresponding magnetization direction is known and suitable filters are applied [124] or additional convergence criteria are defined [125], that provide sufficient constraints on the underlying magnetization.

3.3.3. Nanoscale Stray Magnetic Field Sources

An important application of S-NVM is the study of local nanoscale changes in magnetization. The sensitivity of S-NVM depends on the spatial frequency of the underlying magnetization change, which determines the spatial resolution, which is on the order of the NV-sample distance d_{NV}. Consequently, three different regimes in terms of the spatial resolution can be distinguished: First, the change in magnetization occurs on length scales significantly larger than d_{NV} ($1/k \gg d_{NV}$), in which case sufficiently large spatial frequencies can be recorded, enabling a full reconstruction of the magnetization under the aforementioned boundary conditions. Second, the change in magnetization occurs on length scales significantly smaller than d_{NV} ($1/k \ll d_{NV}$), in which case the NV becomes insensitive to magnetization variations and probes only the average magnetization. Third, the change in magnetization occurs on length scales comparable to d_{NV} ($1/k \approx d_{NV}$), in which case some spatial information is detected, but it is insufficient for a complete spatial reconstruction, which also requires higher harmonics of the underlying characteristic spatial frequencies. In this regime, a stochastic analysis is still possible and allows the extraction of the statistical properties of the underlying magnetization.

To study this stochastic regime, the probability distributions of the stray field values and their spatial frequencies can be analyzed in Fourier space (details in Appendix A.2). Characterizing the resulting distributions $P(x)$ by their statistical mo-
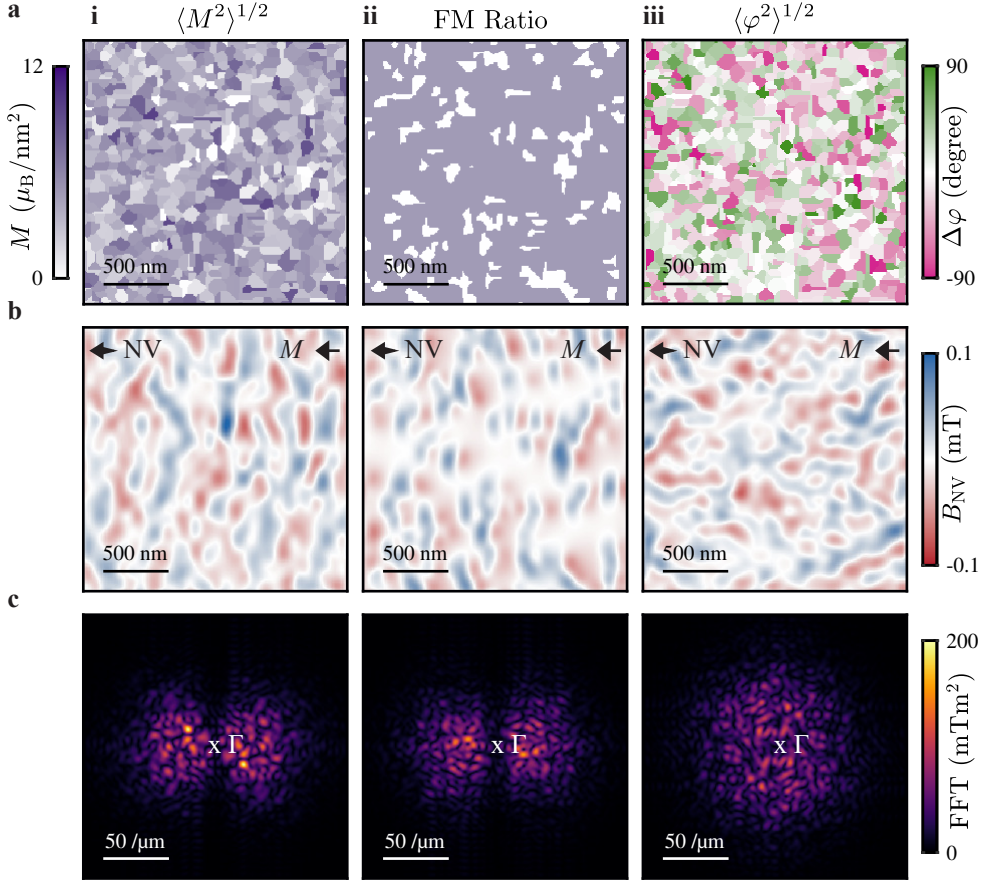
Figure 3.3.: Stray Field Pattern from Various Random Magnetization Pattern. a Three magnetic models for inhomogeneous magnetization patterns based on a Voronoi tiling into homogeneous areas: (i) each area has a magnetization strength drawn from a Gaussian distribution (ii) each area is assigned a non-zero or zero magnetization according to a binomial distribution (iii) each area has a magnetization direction drawn from a Gaussian distribution. All patterns have the same mean magnetization $\langle M \rangle = 4.2\,\mu_\mathrm{B}/\mathrm{nm}^2$ pointing along the x-axis. **b** Resulting stray field pattern recorded by an NV with $(\varphi_\mathrm{NV}, \theta_\mathrm{NV}) = (0°, 54.7°)$ and $d_\mathrm{NV} = 63\,\mathrm{nm}$. All patterns have the same stray field variance $\langle B_\mathrm{NV}^2 \rangle^{1/2}$. The arrows indicate the direction of the NV and the average magnetization. **c** Corresponding Fourier images of the patterns shown in b. All patterns have the same mean spatial frequency $\langle k \rangle$. Γ indicates the origin of the Fourier image.

ments of order N

$$\langle x \rangle^N = \int_{-\infty}^{\infty} (x - \langle x \rangle)^N P(x)\mathrm{d}x \tag{3.10}$$

with $x \in \{B_\mathrm{NV}, k, k_\mathrm{x}, k_\mathrm{y}\}$, provides valuable insight into the underlying magnetization.

While the moments of the stray field are expected to scale with the strength or amplitude of the underlying inhomogeneity, the moments of the spatial frequencies contain information about the relevant length scale and symmetries of the source.

In general, a locally varying magnetic stray field requires a locally varying magnetization. Such a variation can be produced either by a variation in the magnetization strength or by a variation in the magnetization direction. The former can be obtained either by a direct variation of the magnetic properties or by the coexistence of different magnetic states such as paramagnetic or antiferromagnetic and a ferromagnetic state. Examples of such structures with identical average magnetization are shown in Fig. 3.3 **a** with the stochastic model of magnetization strength following a Gaussian distribution (characterized by its standard deviation $\langle M^2 \rangle^{1/2}$), a binomial distribution of ferromagnetic and antiferromagnetic states (characterized by the FM/AFM ratio), and magnetization orientation following a Gaussian distribution (characterized by its standard deviation $\langle \varphi_M^2 \rangle^{1/2}$). These magnetic states are assigned to patterns consisting of tiles with homogeneous magnetization obtained by a Voronoi tessellation (characterized by the average area A of a tile with characteristic size $d = \sqrt{A}$).

Full-parameter searches of simulations with varying size d and distribution parameters $\sigma \in \{\langle M^2 \rangle^{1/2}, \langle \varphi_M^2 \rangle^{1/2}, \text{FM ratio}\}$ show that the mean spatial frequency $\langle k \rangle$ depends only on the former, while it is independent of the magnetic model and the corresponding σ (Appendix A.2). Consequently, $\langle k \rangle$ is a sufficient measure to determine the typical structure size for a given sample. Due to the symmetry of Maxwell's equations ($\nabla \cdot \mathbf{B} = 0$, absence of magnetic monopoles), for a random pattern, it holds that $\langle B_{NV} \rangle \approx 0$ and only $\langle B_{NV}^2 \rangle^{1/2} \neq 0$. For a given d, $\langle B_{NV}^2 \rangle^{1/2}$ increases monotonically with increasing σ, implying that $\langle B_{NV}^2 \rangle^{1/2}$ is characteristic of the underlying distribution of magnetic properties. Therefore, a given stray field map can be assigned a unique Voronoi tessellation with size d and a unique distribution parameter σ by matching d to a given $\langle k \rangle$ and subsequently matching σ to $\langle B_{NV}^2 \rangle^{1/2}$ (an example is given in Fig. 3.3 **b**, where all stray field maps have identical $\langle k \rangle$ and $\langle B_{NV}^2 \rangle^{1/2}$).

While different statistical models can have identical $\langle k \rangle$ and $\langle B_{NV}^2 \rangle^{1/2}$, their Fourier images exhibit distinct symmetries (Fig. 3.3 **c**). A variation in magnetization strength and magnetic state results in a strongly directional pattern aligned orthogonally to the magnetization direction, reflecting the properties of the dipolar tensor. Conversely, a variation in magnetization orientation results in an isotropic Fourier image. However, it is impossible to distinguish between the first two models based on the stray field, since the two mechanisms causing the stray field to arise in both cases are a change in magnetization strength. Distinguishing between these models requires additional information, such as the average macroscopic magnetization.

In summary, although a complete reconstruction of the magnetization pattern is not possible when the structure size is of the order of d_{NV}, statistical information can be derived from the stray field pattern. This statistical information enables the determination of equivalent distributions of magnetic properties, facilitating comparison with different physical models. In Section 4.4, this analytical approach is applied to gain insight into a disordered 2D magnetic film.

3.4. Operating Range of S-NVM

For investigations of 2D magnets, an ideal sensor should operate over the entire phase space where magnetic order occurs. Typical magnetic transitions for 2D magnets occur in the entire temperature range of 1-300 K and in the external magnetic field range up to tens of teslas [80]. While NV magnetometry is suitable for operation over the entire temperature range, sensitive operation is only possible when the external field is applied along the NV axis. In addition, external field strengths of several teslas shift the resonance into the tens of gigahertz regime, which is challenging to access with conventional microwave (MW) electronics. Furthermore, implementation in a cryogenic system poses additional challenges for S-NVM operation in order to avoid disturbances of the fragile magnetism of 2D systems. These three aspects are discussed in more detail in this section.

3.4.1. Temperature Range

The temperature dependence of the NV performance is mainly limited by two key factors. First, the thermally activated phonon population determines the photophysics of the NV and its spin coherence. Second, at cryogenic conditions, the negative charge state of the NV becomes less stable and is more likely to convert to the neutral charge state.

The temperature dependence of the mean occupation number of the phonon modes in diamond can be well modeled by considering two phonon modes with energy $E_1 = 59\,\text{meV}$ and $E_2 = 145\,\text{meV}$. These modes correspond to the highest energy of the acoustic and optical phonon branches of the diamond lattice [54]. The phonon occupation affects the NV performance regarding its spin coherence, because the spin relaxation time is ultimately limited by the phonon-induced spin-lattice relaxation [53]. This limits the maximum temperature at which NV magnetometry can be applied. Due to the absence of spin-orbit coupling in the ground state and the relatively high phonon energies, stable spin coherence can be observed at temperatures well above room temperature [31], significantly exceeding the critical temperatures reported so far for 2D magnetic systems. However, the phonon occupation also results in phonon-induced orbital averaging between the two orbital branches in the excited state, resulting in complex photophysics of the NV center [49][2].

The temperature dependence of the photoluminescence (PL) shows three distinct temperature regimes: At low temperatures ($T < 20\,\text{K}$), the photophysics is described by the excited state level structure derived from group theory (Section 2.1), while at high temperatures ($T > 60\,\text{K}$), the photophysics is captured by a single effective orbital branch. The intermediate transition regime ($T = 20 - 60\,\text{K}$) shows complex excited state dynamics, which can be assessed through the PL intensity of the NV [50]. The field dependent minima of the PL intensity are a result of anticrossings of the different spin levels in the excited state, where a mixing of the $\langle 0|$ and the $\langle \pm 1|$ spin states occurs. This mixing reduces the PL due to the spin-dependent intersystem crossing to the singlet state. At low temperatures, the two orbital branches result in a total of four anticrossings: two within the same orbital branch and two within

---

[2]a detailed discussion of the NV photophysics can be found in works of Happacher et al. to which the author of this thesis contributed as co-author [50, 126].
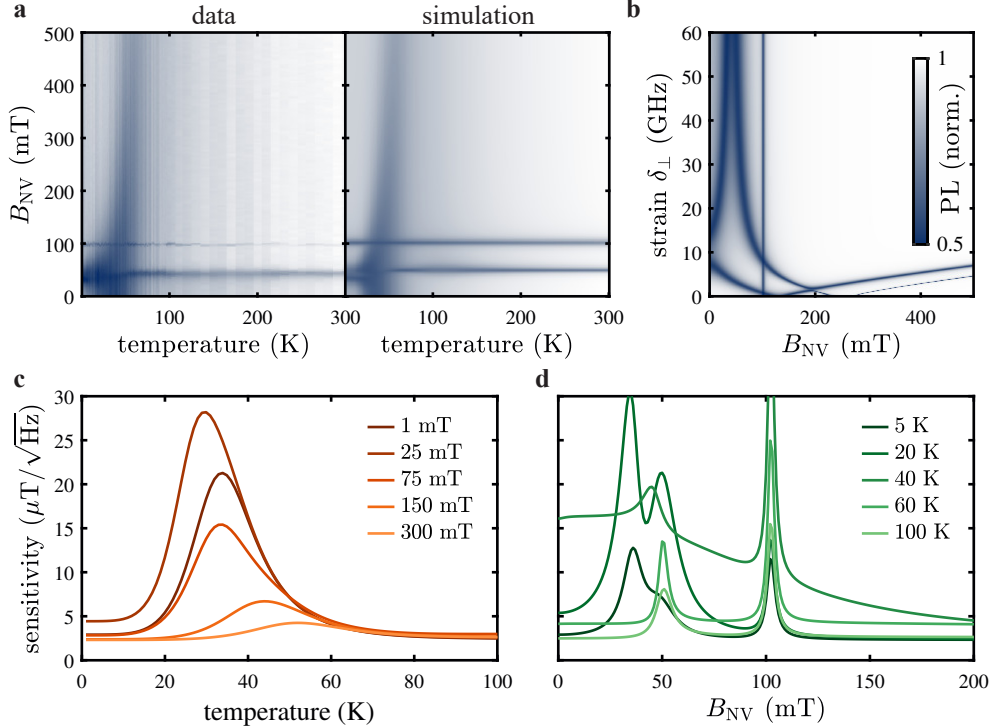
Figure 3.4.: Temperature Dependence of the Sensitivity. a Normalized photo-luminescence of the NV center as a function of temperature and external field along the NV axis. Measurement on an NV in a tip (left) and simulation with effective strain $\delta_\perp = 75\,\text{GHz}$ (right). **b** Simulation of the normalized PL as a function of effective strain at low temperatures such that phonon-induced orbital averaging can be neglected. **c** Sensitivity as a function of temperature for various external magnetic fields. **d** Sensitivity as a function of external magnetic field for various temperatures.

opposite orbital branches. The splitting of these branches depends on the effective strain $\delta_\perp$ experienced by the NV. For typical strain levels present in a diamond AFM tip, the two minima associated with the anticrossings between different branches are at external fields in the tesla regime. They are only observable at low strain levels $\delta_\perp < 10\,\text{GHz}$ [126] (Fig. 3.4 **b**).

Phonons induce a spin-preserving coupling between the two orbital branches, broadening the observed minima when the coupling rate is comparable to the radiative lifetime of the NV. The broadening follows a T^5 scaling, describing the phonon occupation number. Once the orbital mixing rate surpasses the spin mixing rate at the anticrossing, the difference between the orbital branches is effectively averaged out. The resulting photophysics of the NV is then described by an effective spin triplet in the excited state, resulting in a single excited state level anticrossing at $B_{\text{NV}} = 50.5\,\text{mT}$. Together with the minimum caused by the ground state level anticrossing at $B_{\text{NV}} = 102.4\,\text{mT}$, this describes the NV PL in the high temperature

regime [50, 127, 128].

The excited state anticrossings severely restrict the measurement capabilities of
the NV sensor in the corresponding temperature and magnetic field ranges due to the
reduced PL intensity and spin contrast, resulting from the mixing of the spin states.
Both quantities determine the magnetic field sensitivity of the NV, which consequently
deteriorates near the anticrossings (Fig. 3.4 **c, d**). In the low and high temperature
regime, these anticrossings are relatively narrow and limit the sensitivity only in small
external magnetic field windows. In the intermediate regime, the NV performance
is significantly worse over a wide magnetic field range due to the phonon-induced
broadening of the anticrossings. This severely limits the operating regime of NV
magnetometry between 20-60 K, where sensitive measurements are possible only at
large bias magnetic fields in the tesla range, sufficiently far away from any anticrossing.

A major limitation for the operation of NV magnetometry at low temperatures,
and hence in the relevant temperature regime for investigations of 2D magnetism, is
the charge instability of the NV center towards low temperatures, which has been
reported by several groups but is not yet fully understood [129, 130]. This instability
is characterized by a degradation of PL intensity and optical spin contrast, accompa-
nied by a spectral shift of the PL spectrum towards the neutral charge state during
operation of the scanning NV tip. This leads to the phenomenological description that
during operation the charge state of the NV center becomes unstable and the relative
population of the neutral charge state increases [130]. While stable NV operation in
ambient conditions at room temperature is possible for several months, at cryogenic
conditions the degradation is significantly accelerated to a few hours or days, severely
limiting the low-temperature operation of S-NVM.

Since this phenomenon is more pronounced for near-surface NVs, a common hy-
pothesis is that the degradation results from a change in the diamond surface, such as
tribological charging, a change in the surface termination, or adsorption of chemical
impurities [129]. The adsorption of impurities is particularly an issue for cryogenic
operation, as laser-induced contamination is accelerated in the required vacuum con-
ditions [131]. The modification of the surface alters its electron affinity and increases
the relative NV population towards its neutral charge state due to band-bending [132].
The extent of band bending is determined by the charge carriers available in diamond,
which screen surface effects. Consequently, the freezing of charge carriers towards
cryogenic temperatures extends the spatial region of unfavorable band bending, and
thus surface effects become more dominant at low temperatures.

The degradation of the NV charge state may be mitigated by procedures that sta-
bilize the charge state in general, such as various surface terminations [67, 68] or
doping [69]. A second mitigation path is to avoid contaminations associated with the
vacuum conditions required for cryogenic operation and to provide a clean environ-
ment for S-NVM also at low temperatures [131]. Nonetheless, understanding the
exact mechanism of destabilizing the charge state and its prevention is a topic requir-
ing further research to allow reliable operation at low temperatures, a prerequisite for
S-NVM measurements of 2D magnetism.

3.4.2. Magnetic Field Range

The operating magnetic field range of S-NVM is set by three main mechanisms: the crystalline orientation of the NV, the excited state anticrossings, and the maximum frequency of the driving MW source. These factors currently confine S-NVM operation to the field range of a few hundred millitesla along the NV axis.

Quantitative magnetometry is only possible if the external magnetic field is mainly aligned with the NV axis, resulting in a linear Zeeman splitting. In contrast, an orthogonal magnetic field leads to a mixing of the $\langle 0|$ and $\langle \pm 1|$ spin states, reducing the spin contrast and limiting the NV operation to orthogonal fields of a few tens of millitesla [133]. To explore the phase diagram of 2D magnetic systems, one is usually interested in applying the external field along the fundamental magnetic anisotropy directions of the magnetic system, typically the in-plane or out-of-plane direction. The quantization axis of the NV is set by its crystalline orientation, and conventional diamond tips are cut along the crystalline $\langle 100 \rangle$ direction of the diamond, forming an angle of $\theta_{NV} = 54.7°$ to the sample normal. However, recent works have shown that by using diamonds cut along the $\langle 111 \rangle$ and $\langle 110 \rangle$ directions, NV tips can be aligned with the out-of-plane orientation [134] and in-plane orientation [135], respectively[3]. However, even with these tips, a large field can only be applied along one NV-specific direction, requiring the use of multiple different tips to explore the entire magnetic field dependence of the phase space along the symmetry axes of a magnetic sample.

Anticrossings, as discussed in Section 3.4.1, impose additional constraints on the operating regime of S-NVM. These anticrossings induce mixing between the different spin states at a given external field, which reduces the overall spin contrast. At both high and low temperatures, these field ranges are rather narrow, but in the intermediate temperature range of 20-60 K, the anticrossings impose severe limitations on NV magnetometry.

Finally, there is also a technical limitation for the field regime due to the required coherent driving of the NV, which requires a MW capable of accessing the resonance frequency. The gyromagnetic ratio of the NV spin $\gamma_{NV} = 28\,\text{GHz/T}$ is rather high, advantageous for magnetic field sensitivity, but also leads to high spin resonance frequencies at moderate external fields. Typical commercial MW equipment with a cut-off frequency of tens of gigahertz constrain the operation to the sub-tesla regime, often insufficient to reach the coercive field or metamagnetic transitions of common 2D magnetic systems.

3.4.3. Cryogenic Implementation

To cover the full temperature and magnetic field range with S-NVM, integration of the setup into a cryostat is required. A complete experimental setup comprises four main subsystems: optical access for spin readout and initialization, MW control for coherent spin manipulation, an AFM setup to control the NV distance and its lateral position, and temperature and external magnetic field control.

Several cryostat concepts are suitable for S-NVM operation. The most basic concept is the helium bath cryostat, where a sample chamber containing the NV setup is placed in a bath of liquid helium, cooling the entire chamber to its base temperature

---

[3]the author of this thesis contributed as a co-author to the work of Rohner et al. [134]

of 4.2 K. While contact with a thermal bath is beneficial in terms of AFM operation due to the isolation from the environment after preparation, the bath requires periodic refilling in typical operating cycles of a few days, limiting long-term measurements. An alternative is a closed-cycle cryostat, where cooling power is generated by the compression and expansion of a closed He cycle, allowing the cooling of a heat sink (e.g. a large copper plate) down to the condensation point of He at $T = 4.2$ K. Thermal contact between a sample chamber and the heat sink enables cooling of the chamber to its base temperature. Although such a system provides continuous operation, the compression and expansion of the closed cycle induce significant mechanical vibrations from which the NV setup must be isolated to perform measurements in AFM contact. Closed-cycle cryostats have the additional advantage that the heat sink can also be coupled to a secondary cooling cycle. Such a cycle is used to achieve even lower base temperatures, for example by evaporative cooling for temperatures below < 2 K or dilution cooling of a ^{3}He/^{4}He mixture to approach millikelvin temperatures. In this work, a commercial bath cryostat (Attocube, attoLiquid1000 detailed description in [136]) and a commercial closed-cycle cryostat with evaporative cooling (Attocube, attoDry2200 details in Appendix A.1) are used. A description of a closed-cycle dilution refrigerator is given elsewhere [130].

Excitation and optical readout of the NV is achieved using a confocal microscope setup. A green laser at 532 nm and a subsequent acousto-optic modulator provide the excitation light, which is fiber-coupled to an optical head mounted on top of the cryostat. The excitation light is focused on the NV inside the sample chamber by an achromatic cryogenic objective, which also collects the resulting PL of the NV, separated by dichroic filters and detected by a fiber-coupled single-photon detection unit. Coherent MW driving is achieved by a resonant MW field, for instance applied by a local antenna such as a gold wire spanned across the sample at $\approx 50 - 200$ µm distance from the NV. For the AFM setup, all-diamond AFM tips are commonly used with an NV embedded close to its apex (≈ 20 nm). Such an AFM tip is integrated into commercial cryogenic AFM systems, although the topographic resolution is limited by the large (≈ 200 nm) tip diameter required for good optical coupling. Details of the experimental setup used are described in Appendix A.1.

A common challenge for any characterization tool is to avoid disturbing the sample during the investigation, especially for fragile samples such as 2D vdW magnets. For S-NVM, the following disturbance mechanisms have to be considered: the mechanical pressure of the AFM tip, the optical power and the MW power.

Mechanical pressure arises from the AFM operation, required to place the NV center as close as possible to the sample. This is done by monitoring either the oscillation amplitude or the resonance frequency of a tuning fork to which the NV tip is attached. Close to contact, the mechanical force between the tip and the sample induces both a damping of the amplitude and a frequency shift of the resonance, allowing the tip to be kept at a constant height above the surface by an appropriate PID loop. This mechanical force is also exerted on the sample and thus affects its magnetic properties. However, the mechanical forces required to alter the magnetic state of a 2D magnet are typically much larger than the mechanical forces exerted by the AFM tip [92]. In addition, AFM operation exposes the sample to the risk of a singular, strong mechanical perturbation, resulting in a loss of feedback control and

subsequent puncture of the sample with irreversible effects on the magnetic sample, as reported for CrI_3, where such a puncture has changed the interlayer coupling from AFM to FM [26].

The optical power required for efficient S-NVM operation is roughly set by the saturation power of the NV center, and for parabolic diamond scanning probes it is on the order of tens of microwatts [64]. Although such laser powers typically do not exert a significant back action on the magnetic state [26], in scenarios where the excitation wavelength overlaps with the absorption band of the sample, the optical power can induce a photophysical change in the magnetic properties [101]. While the optical power of S-NVM operation is rather low, the MW power required for spin manipulation is rather high because the distance between the antenna and the NV reduces the coupling efficiency. The applied MW frequencies are in the range of a few gigahertz, which is typically too low to directly excite any spin dynamics, because the ferromagnetic resonance is typically in the order of tens of gigahertz [137]. However, the applied power in the order of tens of milliwatts [26] induces significant local heating, which is particularly problematic for samples with a low ordering temperature.

Changing the measurement scheme from continuous-wave to pulsed operation mitigates the negative effects of both optical and MW power. Pulsed operation provides the flexibility to adopt the duration of the applied sources, thus allowing the required power to be reduced either by extending the interrogation time or by introducing a dead time into the measurement cycle. A case illustrating the impact of MW heating on single-layer $CrCl_3$ is shown in Fig. 3.5. At the base temperature of the cryostat, a different magnetic order is observed using either cw-ODMR (**a**) or a pulsed ODMR (**b**) measurement scheme: While almost no magnetic signature is observed in the former, weak magnetic order is observed in the latter image, indicating a difference in the local sample temperature, confirmed by the resistive temperature readout below the sample plate. This highlights the importance of MW power management for accurate measurements, especially near critical temperatures.

3.5. **Summary and Outlook**

This section provides an introduction to 2D magnetic materials as an interesting class of materials. While the exploration of their magnetic properties and the various ways to manipulate them is still a major focus of current research, the integration of these materials into 2D vdW heterostructures offers a great prospect for both fundamental research and advances in the field of spintronics. Nanoscale phenomena such as non-trivial spin textures, 2D domain formation, or Moiré superlattices arise in such systems, urging the need for nanoscale characterization techniques. While optical imaging tools are typically diffraction-limited, scanning probe techniques offer spatial resolutions in the tens of nanometers. S-NVM directly images the stray field arising from a 2D magnet, enabling calibration-free determination of the magnetization of the sample. Although a magnetization generates a well-defined stray field, the field itself is not unique to a specific magnetization, requiring additional assumptions to quantitatively determine the magnetization. The spatial resolution of S-NVM with respect to a 2D magnetization can be deduced from the dipolar tensor and is given by the NV-sample distance $d_{NV} \approx 30 - 100\,nm$. In principle, S-NVM can operate
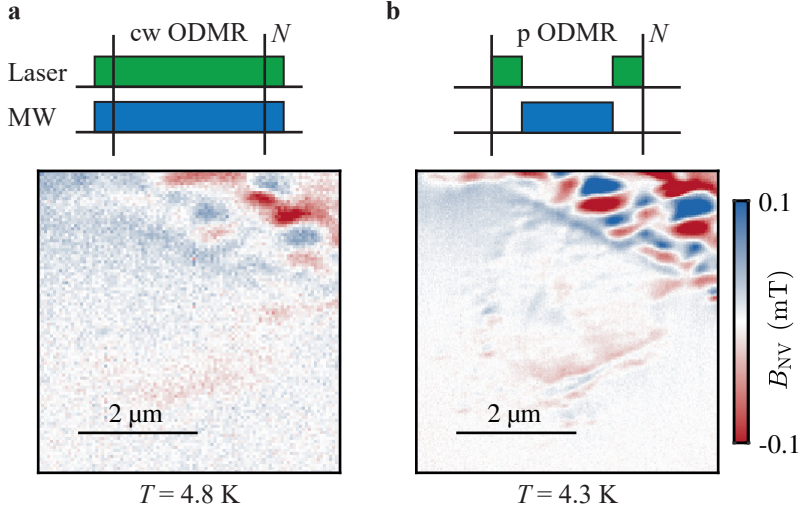
Figure 3.5.: Impact of the Microwave on the 2D Magnet. **a** Image of the stray magnetic field of a single-layer $CrCl_3$ flake attached to a multilayer part by cw ODMR at a nominal sample temperature $T = 4.8\,K$. **b** Image of the stray magnetic field of the same flake by pulsed ODMR at a nominal sample temperature $T = 4.3\,K$. Although both measurements are taken at the base temperature of the cryostat, MW induced heating can have a severe impact on the observed magnetic order near the critical transition.

throughout the entire relevant temperature range, but excited state photophysics limits the sensitivity in certain field ranges, especially in the intermediate temperature range of $20 - 60\,K$. However, a major limitation of S-NVM is that good sensing performance is only achieved when the external field aligns with the NV axis, typically not aligned with the fundamental axes of the sample. The common integration into a cryogenic setup exposes the sample to weak mechanical forces during AFM operation and optical and MW powers during spin manipulation. While these disturbances are typically small and do not affect the magnetic state, S-NVM is considered a non-invasive measurement technique. However, these disturbances have secondary effects such as heating the sample chamber, which poses a challenge for measurement scenarios at low temperatures approaching the base temperature of the cryostat used.

In conclusion, S-NVM is suitable for nanoscale imaging of 2D magnetism due to its high magnetic field sensitivity, excellent spatial resolution, calibration-free measurement of the stray field, large operating range, and minimal impact of the technique on a magnetic sample. For these reasons, S-NVM is considered a powerful tool to study 2D magnetism [25], as demonstrated by previous works: The technique has been used to quantify the magnetization of single-layer CrI_3 and to shine light on its unusual AFM interlayer coupling [26]. Furthermore, the nucleation and propagation of domains while changing the external environment have been studied in $CrBr_3$ [103] as well as in $Fe_{5-x}GeTe_2$ [138]. Finally, the technique has even been exploited to image the exotic domain pattern that arises when two successive CrI_3 layers are twisted

by a small angle to obtain a magnetic Moiré superlattice [27]. The next two chapters delve into two additional use cases: the analysis of the inhomogeneous magnetic state of single-layer MBE-grown $EuGe_2$ and the investigation of the exchange bias in the $MnPS_3/Fe_3GeTe_2$ heterostructure, found to be attributed to an unexpected anomalous magnetic moment in $MnPS_3$.

4. Nanoscale Magnetism of Single-Layer EuGe$_2$

As discussed in the preceding chapter, two-dimensional (2D) van der Waals (vdW) magnets hold significant potential for novel physical phenomena at reduced dimensionality and offer prospects for new spintronic heterostructures and devices [80]. However, devices based on these materials typically rely on mechanical exfoliation, resulting in micrometer-sized flakes with poorly defined lateral geometry, severely limiting their scalability and integration into more complex architectures [113]. Issues such as uniformity, wrinkles, surface contamination, and interfacial bubbles arise during exfoliation, severely compromising device quality, especially with increasing area size and fabrication steps [139]. To overcome these issues, large areas of 2D materials can be grown by chemical processes such as chemical vapor deposition or molecular beam epitaxy (MBE) [113].

Various 2D magnetic systems have been successfully grown at wafer-length scales, including Fe$_x$GeTe$_2$ [140, 141], chromium chalcogenides [142], chromium trihalides [116], or lanthanide metalloxenes [143, 144]. Limited control of lateral geometry by selective nucleation [145, 146] or preferential growth along crystallographic directions [147] has been achieved. However, despite the atomic-level cleanliness of these large-area films, nanoscale grain structures commonly form during the growth process and affect local magnetic properties. For instance, lattice mismatch and growth-induced defects cause variations in the strain environment, affecting the magnetic anisotropy [148]. Therefore, advanced magnetic characterization techniques are needed to understand the impact of these defect structures on magnetic properties and to guide the improvement of fabrication protocols for large-area 2D magnetic materials.

This chapter discusses the magnetic properties of single-layer EuGe$_2$ MBE grown on pre-patterned substrates. First, the sample fabrication is presented with a focus on the patterning of the substrate, enabling the realization of 2D magnets with well-defined lateral geometry. Subsequently, an in-depth characterization of the average film magnetic properties is provided, revealing local disorder, which is further investigated. It is found that a model of a disordered 2D magnet effectively describes single-layer EuGe$_2$, where the disorder manifests as a grain structure, in which each grain is characterized by an individual critical temperature[1].

4.1. Magnetism of EuGe$_2$

EuGe$_2$ is a layered A-type antiferromagnet (AFM) belonging to the class of lanthanide metalloxenes [151]. Its structure comprises a metallic honeycomb lattice

---

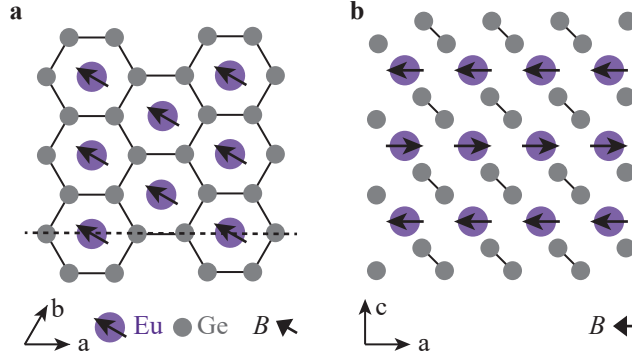[1]These results have been presented in [149, 150].

Figure 4.1.: Atomic Structure of EuGe$_2$. a Top view of the EuGe$_2$ structure. The germanium atoms form a honeycomb lattice with an europium ion in the center. The latter carries the magnetic moment, which has a ferromagnetic intralayer coupling with an easy-plane anisotropy. The direction of the moment is set by the external magnetic field. **b** Side view of the EuGe$_2$ structure. The Ge honeycomb lattice consists of two separate and vertically displaced triangular lattices. The Eu ions are stacked on top of each other and their interlayer coupling is antiferromagnetic.

formed by germanium with a single europium ion placed at the center of the honeycomb cell (Fig. 4.1). The honeycomb lattice, formed by the Ge atoms, consists of two vertically displaced triangular sublattices. Within each honeycomb cell, the Eu ion is centered, and the distance of two neighboring Eu ions defines the crystallographic a- and b-axes with $a = b = 0.410$ nm, while different layers are vertically aligned along the crystallographic c-axis with $c = 0.498$ nm. The overall structure exhibits the trigonal symmetry of the $P\bar{3}m1$ space group [152, 153].

The half-filled $4f$-shell of the Eu ion results in a strong magnetic moment $J = 7/2$. In bulk, the moments order below a Nèel-temperature $T_N = 49.6$ K with an AFM interlayer coupling and a ferromagnetic (FM) intralayer coupling with an easy-plane anisotropy. The strength of the magnetic moment, consistent with the $7\mu_B$ per Eu ion, yields a saturation magnetization of the single layer of $M_{Sat} = 48.8\,\mu_B/nm^2$ [152, 153].

In the few-layer limit, the magnetic properties of EuGe$_2$ deviate from the bulk properties. While the easy-plane anisotropy and FM intralayer coupling are preserved, the AFM interlayer coupling transitions towards FM coupling, resulting in a nonzero FM moment for even layers of EuGe$_2$. The ordering temperature decreases with decreasing layer number and becomes highly dependent on the applied external magnetic field. The Eu ion exhibits a reduced magnetic moment, for example around $2\mu_B$ at 2 K for the single-layer, indicating the significance of interlayer coupling in stabilizing long-range FM order [144]. In addition, the single-layer magnetization shows an AFM field response described by a generalized Brillouin function [117] and a strong intrinsic exchange bias [154]. The observation of FM order and AFM field response suggests the coexistence of different magnetic states within a single layer of EuGe$_2$, potentially manifesting in a nanoscale magnetic structure, resulting in a nanoscale magnetic stray field signature.

4.2. Sample Fabrication

Scanning nitrogen-vacancy magnetometry (S-NVM) directly probes the stray magnetic field arising from a 2D magnetic sample. It therefore requires a boundary of the magnetized area within the sample, since a homogeneous magnetization does not produce a stray field. Such a boundary can be induced, for instance, by a change in the topography of the sample on a patterned substrate. In this study, a single layer of EuGe$_2$ grown on a pre-patterned substrate is investigated. The pattern is defined by e-beam lithography and transferred into the substrate by reactive ion etching (RIE). In the final step, a single-layer EuGe$_2$ is grown on the patterned substrate by MBE (Fig. 4.2). This procedure allows the realization of a 2D magnetic film with circular and rectangular geometries suitable for characterizing the magnetic properties of the film. It also provides control over the lateral geometry, enabling the realization of arbitrary geometries for shape-engineering of 2D magnets (Section 4.5.1).

The lateral geometries are defined by e-beam lithography on a commercial $\langle 111 \rangle$ Ge wafer. The orientation is chosen for its surface termination matching the crystalline symmetry of the Ge honeycomb lattice of EuGe$_2$. Prior to processing, the substrate is cleaned for 10 min in 37 % HCl solution to surface terminate the Ge with hydrogen for improved resist adhesion. This termination is required as the common e-beam resist, hydrogen silsesquioxane (HSQ, commercial name FOX-16, DuPont), exhibits poor adhesion to Ge [155]. The resist is spun onto the substrate and heated for 5 min at 120 °C. After that, the substrate is exposed with the e-beam (dose 200 µC/cm^2,
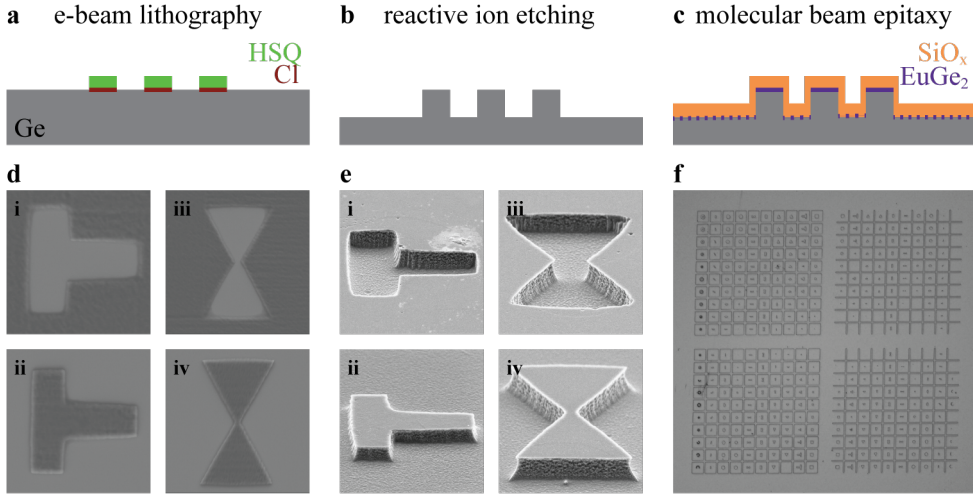

Figure 4.2.: Fabrication of MBE Grown EuGe$_2$ on a Patterned Substrate. a, b, c Schematic of the three-step fabrication process: definition of the pattern by e-beam lithography, transfer of the pattern to the substrate by reactive ion etching, overgrowth of EuGe$_2$ and a protective layer of SiO$_x$ by molecular beam epitaxy. **d, e** Scanning electron microscope images of the lithographic mask and the patterned substrate. **f** Optical microscope image of the final sample with a 1 mm × 1 mm write field consisting of 400 different structures.

acceleration voltage $30\,\mathrm{kV}$). The exposed film is developed for $30\,\mathrm{s}$ in $25\,\%$ tetramethylammonium hydroxide, resulting in lithographic masks as shown in Fig. 4.2 **d**.

The mask is transferred to the substrate using an inductively coupled plasma (ICP) RIE. Ge is etched by an SF_6 plasma [156], using the commercial plasma chamber etcher 500 SI 500. SF_6 is introduced into the plasma chamber (gas flow $20\,\mathrm{sscm}$, pressure $1.33\,\mathrm{Pa}$) and ionized by an inductively coupled microwave power (ICP power $100\,\mathrm{W}$). The ions, accelerated toward the substrate by a radio frequency (RF) magnetic field (RF power $100\,\mathrm{W}$), etch the exposed part of the Ge wafer not covered by the lithographic mask. Etch times ranging from $30\,\mathrm{s}$ to $60\,\mathrm{s}$ result in structure heights of $180(10)\,\mathrm{nm}$ to $390(30)\,\mathrm{nm}$ indicating a linear etch rate. The remaining mask is removed in a $60\,\mathrm{min}$ bath of $2\,\%$ HF (Fig. 4.2 **e**).

The patterning process allows the realization of geometries down to feature sizes of around $500\,\mathrm{nm}$, limited by the e-beam resist and the plasma process as explained in the following. Although the substrate is hydrogen terminated, the adhesion of the HSQ remains a limitation for small feature sizes due to the relatively high e-beam doses needed, leading to overexposure of small features. This issue could be addressed by using spatially inhomogeneous doses that are optimized for each individual geometry, taking into consideration that sharp features require a lower dose. Another limitation arises from the etching process: the SF_6 plasma etches primarily along the $\langle 111 \rangle$ direction but also slowly along the $\langle 110 \rangle$ direction, resulting in an undercut of the structures. Consequently, small features are lost during the etching process, leading to less well-defined geometries. The etching process also roughens the exposed Ge surface, which can be exploited in the MBE process, as an ordered magnetic film forms only on the unexposed flat surface. Thus, the etching process acts as an effective spatial filter for the MBE growth.

The final growth of the single-layer EuGe$_2$ on the patterned substrate by MBE follows the recipe for film growth published in detail in previous work [143, 144]. The final film is covered with a $20\,\mathrm{nm}$ layer of SiO$_x$ to prevent any degradation in air (see [144] for further details)[2].

4.3. Magnetic Properties of the Monolayer

The patterned substrate provides a boundary that allows S-NVM to evaluate the magnetic properties of the single-layer EuGe$_2$ based on its stray magnetic field. However, it is not immediately apparent whether the patterning process alters the magnetic properties of the film. The following section demonstrates that the main magnetic properties of EuGe$_2$ are preserved and that previously observed anomalies, the reduced saturation magnetization [144] and the external field response [117], are reproduced. Furthermore, these anomalies can be understood as EuGe$_2$ being a disordered 2D magnet.

4.3.1. Easy-Plane Anisotropy

Circular and rectangular structures are well suited for characterization purposes. The rectangular structure allows an analytical estimation of the magnetization strength,

---

[2]The MBE growth has been performed by the authors of the work [144]

while the circular structure is ideal for studying the symmetries of the magnetic system.

The measured stray magnetic field emanating from the edge of the circular structure is consistent with the expected easy-plane anisotropy of $EuGe_2$ (Fig. 4.3). Under a weak external magnetic field $B_{ext} = 5\,mT$ applied along the projection of the NV axis in the in-plane direction, the observed stray field is consistent with an in-plane magnetized film, with its magnetization direction parallel to B_{ext} (Fig. 4.3 **c, d**). Conversely, when B_{ext} is applied in the out-of-plane direction, almost no stray magnetic field is observed and the remaining weak signal retains signatures of an in-plane magnetization (Fig. 4.3 **e**). Consequently, the Zeeman energy is insufficient to tilt the spins in the out-of-plane direction, and the spins maintain their preferred orien-
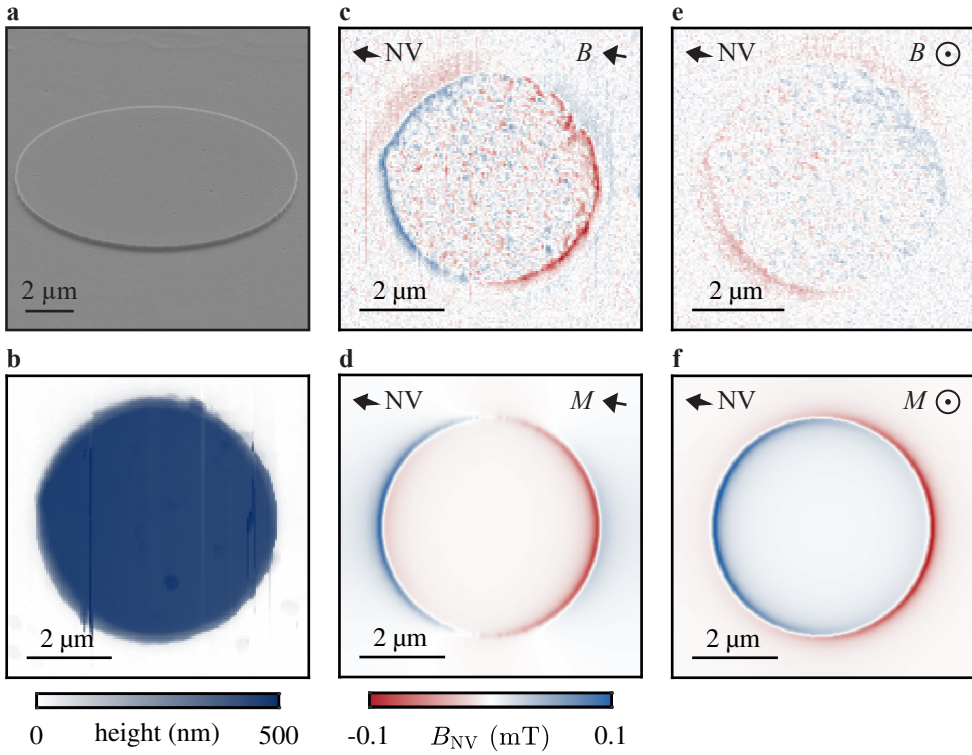

Figure 4.3.: Stray Magnetic Field Images of a Circular Structure. a Scanning electron microscope image of a circular $EuGe_2$ structure (viewed at a 70° angle). **b** Atomic force microscope image obtained simultaneously with the S-NVM measurement of a structure similar to that shown in a. **c, e** Stray magnetic field image of the circular structure. An external magnetic field of $B_{ext} = 5\,mT$ is applied along the projection of the NV axis in the in-plane direction (c) and in the out-of-plane direction (e) as indicated by the arrows. **d, f** Simulation of the stray magnetic field in which the magnetization direction follows the direction of B_{ext}. Note that the application of an out-of-plane field does not result in an out-of-plane magnetization (e, f).

tation along the in-plane direction, consistent with the strong easy-plane anisotropy reported in previous studies of the film properties [144]. Importantly, in all acquired data sets, where B_{ext} is applied along an in-plane direction, the magnetization consistently aligns with the direction of B_{ext}, with no discernible preferred orientation within the plane. This suggests that any potential uniaxial in-plane anisotropy is minimal, as evidenced by the absence of a coercive field within the resolution of the employed vector magnet (see Section 4.4.1).

In addition to the stray magnetic field arising from the edge of the structure, the interior of the magnetic film exhibits a complex magnetic texture. This texture indicates local variations in the magnetization that may be due to magnetic domains or structural disorder. Thus, the stray field observed at the edge describes the average magnetization $\langle M \rangle$ of the magnetic film. Interestingly, the observed texture is only present on the top surface of the structures, suggesting that the fabrication process, in particular the RIE step, serves as a spatial filter: An ordered magnetic film is selectively and exclusively deposited on areas not exposed to the SF$_6$ plasma.
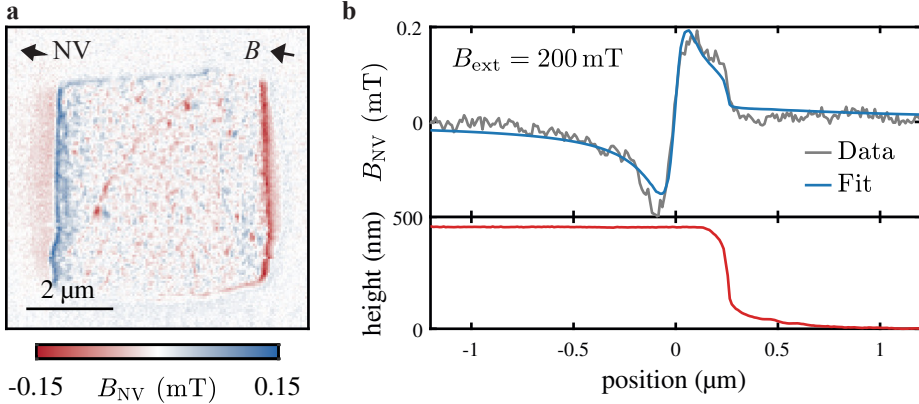
4.3.2. Characteristics of the Average Magnetization

Figure 4.4.: Stray Magnetic Field of a Rectangular Structure. a Stray magnetic field image of a rectangular structure while an external field of $B_{ext} = 5\,\text{mT}$ is applied along the directions indicated by the arrows. **b** Line cut taken at $B_{ext} = 200\,\text{mT}$ with a $\langle 110 \rangle$ NV tip. Stray field from the edge of the structure and an analytical fit to extract $\langle M \rangle$ (top panel), taking into account the topography in the line cut (bottom panel).

The stray field from the edge of a rectangular structure can be calculated analytically, and thus it is used to determine the average magnetization $\langle M \rangle$ of single-layer EuGe$_2$. Similar to the stray field observed at the circular structure, the magnetization direction is in-plane and aligned with the external magnetic field (Fig. 4.4 **a**). To reliably determine $\langle M \rangle$, the topography must be explicitly taken into account, which precludes the use of reconstruction algorithms that assume constant height measurements of the stray field. However, the stray field from the structure can be
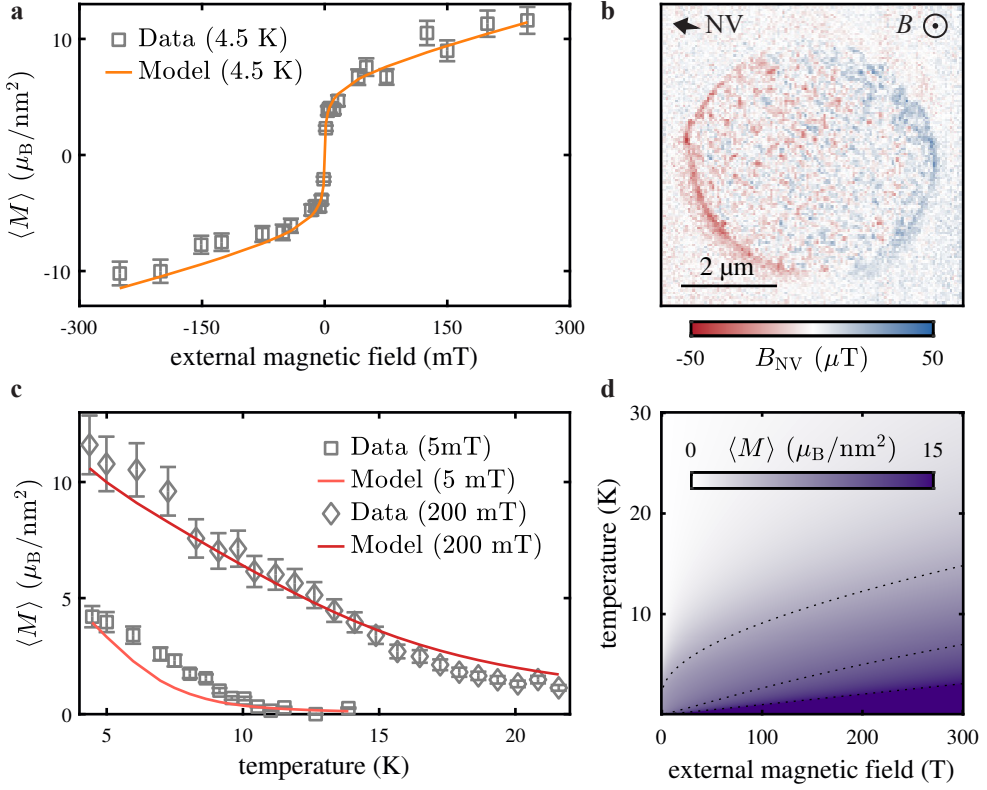
Figure 4.5.: Dependence of Average Magnetization on External Field and Temperature. a Dependence of $\langle M \rangle$ on B_{ext} acquired at $T = 4.5\,\text{K}$, the line corresponds to the model of a disordered 2D magnet (see Section 4.3.3). Uncertainties are estimated by the deviation between measurements under identical experimental conditions. **b** Magnetic stray field image acquired with an external field $B_{\text{ext}} = 0.5\,\text{mT}$ applied in the out-of-plane direction to approximate zero field conditions. **c** Dependence of $\langle M \rangle$ on T at $B_{\text{ext}} = 5\,\text{mT}$ and $B_{\text{ext}} = 200\,\text{mT}$ similar to a. **d** $\langle M \rangle$ as a function of T and B_{ext} as predicted by the model description. Dotted lines represent isolines for $\langle M \rangle = 5, 10, 15\,\mu_{\text{B}}/\text{nm}^2$.

approximated by a magnetic edge (according Eq. (3.5), Section 3.3.1). Utilizing the in-plane symmetry of the magnetic film and the previously determined NV orientation, the only fitting parameters are $\langle M \rangle$ and the NV-sample distance d_{NV}. According to the fit, at $B_{\text{ext}} = 200\,\text{mT}$ and $T = 4.5\,\text{K}$ single-layer EuGe$_2$ exhibits an average magnetization $\langle M \rangle = 11.6(7)\,\mu_{\text{B}}/\text{nm}^2$ ($d_{\text{NV}} = 63(6)\,\text{nm}$, Fig. 4.4 **b**). This magnetization is significantly lower than the saturation magnetization of a fully polarized Eu layer $M_{\text{Sat}} = 48.8\,\mu_{\text{B}}/\text{nm}^2$, but is consistent with previous film characterizations [144].

To further explore the characteristics of the average magnetization, the dependence of $\langle M \rangle$ on B_{ext} is examined (Fig. 4.5 **a**). For this purpose, several line cuts are recorded across a fixed sample position at various magnetic fields (similar to

Fig. 4.4 **b**). The resulting field dependence shows two noteworthy features: First, no coercive field B_{coer} is detected within the precision of the vector magnet, yielding an upper bound $B_{\text{coer}} < 1.3\,\text{mT}$. This low coercive field suggests a low uniaxial in-plane anisotropy, for which the breakdown of long-range magnetic order is expected in the limit of vanishing anisotropy (see Section 4.3.4). To assess the presence of a remanent magnetization, the circular structure is imaged at $B_{\text{ext}} = 0.5\,\text{mT}$ applied out-of-plane to sufficiently split the NV resonances. Even with an in-plane field significantly less than $0.5\,\text{mT}$, the structure exhibits signatures of an in-plane magnetized film (Fig. 4.5 **b**). Second, at moderate external fields $B_{\text{ext}} > 50\,\text{mT}$, $\langle M \rangle$ does not saturate, but instead shows a linear dependence on B_{ext}. This finding is consistent with previous results from X-ray magnetic circular dichroism measurements, where this behavior is explained by an AFM contribution to the total magnetization, leading to the proposal of the coexistence of different magnetic states within the film [117].

The temperature dependence of the average magnetization, obtained by a similar series of line cuts, also shows a clear field dependence (Fig. 4.5 **c**). Additionally, no single sharp critical temperature is observed, as would be expected for a homogeneous FM ordered magnet. Instead, the onset of FM ordering is field dependent, with a smooth transition to higher temperatures typical of a disordered magnetic film [157]. This interpretation aligns with the nanoscale magnetic texture observed on top of the structures, suggesting that single-layer EuGe$_2$ could indeed be described by a disordered 2D magnet model, as developed in the following section.

4.3.3. Description as a Disordered 2D Magnet

The description of the average magnetization $\langle M \rangle$ of a disordered 2D magnet is based on the Arrott-Noakes equation, which describes the FM order of the film, and on the assumption of a probability distribution of the critical temperature to account for the observed disorder.

Due to the observed breakdown of long-range magnetic order and the field dependence of the average magnetization, $\langle M \rangle$ cannot be described by a simple power law for the critical transition. Instead, an explicit consideration of the external magnetic field B_{ext} is required, and the empirical Arrott-Noakes equation (Eq. (3.3), Section 3.1) provides a suitable formalism that explicitly accounts for B_{ext}. However, this equation would predict long-range FM order at zero field, and thus does not account for the expected breakdown of long-range magnetic order in systems with low in-plane anisotropy. Therefore, it is only valid for sufficiently high B_{ext} to stabilize the FM system, which reflects the used experimental conditions.

To include disorder in the model, a probability distribution of the critical temperature $p(T_c)$ is introduced, following the approach used for granular films [157]. The average magnetization $\langle M \rangle$ is expressed by

$$\langle M(T, B_{\text{ext}}) \rangle = \int_0^\infty p(T_c)\, M(T, B_{\text{ext}}, T_c)\, \mathrm{d}T_c, \tag{4.1}$$

where the magnetization M is given by Eq. (3.3). To fit the disorder model to the measurement of $\langle M \rangle$, Eq. (4.1) is discretized

$$\langle M(T, B_{\text{ext}}) \rangle \approx \sum_i p_i(T_c^i)\, M(T, B_{\text{ext}}, T_c^i)\, \Delta T_c, \tag{4.2}$$

where $p(T_c)$ is discretized into bins of width ΔT_c and the integral over the distribution is replaced by the sum over the different bins. Since Eq. (3.3) diverges for $T_c = 0$, the magnetization in the corresponding bin is replaced by the Brillouin function for the Eu ion

$$M_{T_c=0}(T, B_{\text{ext}}) = M_{\text{PM}} \left(\frac{2J+1}{2J} \coth \left(\frac{2J+1}{2J} x \right) - \frac{1}{2J} \coth \left(\frac{1}{2J} x \right) \right)$$

$$x = \frac{J \, g \, \mu_B \, B_{\text{ext}}}{k_B \, T}, \tag{4.3}$$

where $J = 7/2$ for the spin of the Eu ion, g the gyromagnetic ratio, μ_B the Bohr magneton, and k_B the Boltzmann constant. M_{PM} represents the magnetization described by Eq. (4.3) and is interpreted as a paramagnetic contribution to the average magnetization $\langle M \rangle$.

The so-defined model is employed to fit the temperature and field dependence of the average magnetization, as shown in Fig. 4.5. The fitting parameters are summarized in Table A.1. The overall agreement of the model with the data is reasonable, mostly within the estimated uncertainty of the measurement. However, systematic deviations between model and data are observed at small fields $B_{\text{ext}} \leq 5\,\text{mT}$, indicating that the simplified model does not fully capture the physics in this field range. This demonstrates an important limitation of this model, as it cannot reproduce the expected breakdown of long-range magnetic order for systems with low in-plane anisotropy.

The model contains six fitting parameters and the additional fitting parameter $p_i(T_c^i)$ for each discretization bin of the critical temperature ΔT_c. Thus, the fitting procedure is prone to the issue of overfitting. However, three consistency checks support the validity of the fitting procedure and suggest that numerical artifacts resulting from overfitting are not critical:

1. Although the exact probability distribution depends on the number of bins N (Fig. 4.6 **a**), the mean $\langle T_c \rangle$ of the distribution and its variance $\langle T_c^2 \rangle^{1/2}$ converge well (Fig. 4.6 **b**). Furthermore, the mean and variance are consistent with an approximate Gaussian distribution for $p(T_c)$, which requires only two fitting parameters for the probability distribution.

2. For $B_{\text{ext}} \to 0$, the model predicts a saturation magnetization of M_{Sat}

$$M_{\text{Sat}} = M_0 \left(\frac{a}{b} \right)^\beta + M_{\text{PM}} := M_{\text{FM}} + M_{\text{PM}} = 43.9(92)\,\mu_B/\text{nm}^2. \tag{4.4}$$

   This matches the expected saturation magnetization of a fully polarized Eu ion of $48.8\,\mu_B/\text{nm}^2$ within the fit uncertainties.

3. The obtained scaling parameters $\beta = 0.250(27)$ and $\gamma = 2.78(42)$ agree with previously reported empirical scaling parameters $\beta = 0.227$ and $\gamma = 2.2$ for similar low in-plane anisotropy systems [116] and theoretical estimates from the high temperature behavior of the 2D-XY spin model $\beta = 0.231$ and $\gamma = 2.4$ [158].

The description of single-layer EuGe$_2$ as a disordered FM system suggests that only a small fraction of the Eu spins are FM ordered. Thus, the reduced average magnetization is explained by the low overall FM ratio $M_{\text{FM}}/M_{\text{PM}} = 16.4(43)\,\%$. The
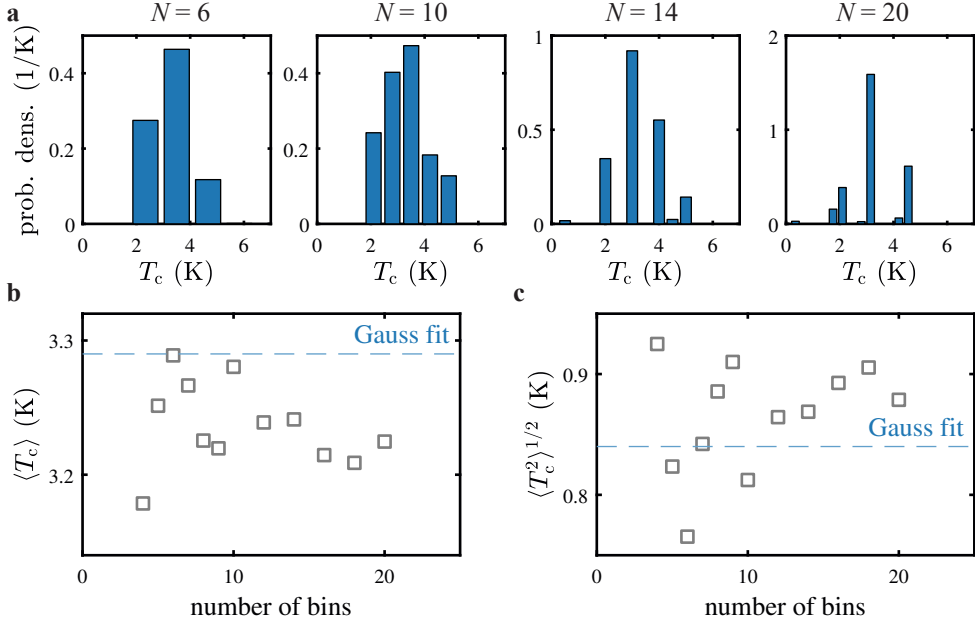
Figure 4.6.: Convergence of the Probability Distribution of the Critical Temperature. a Obtained probability distributions $p(T_c)$ by fitting the model to the measurements for various numbers of discretization bins $N = 6, 10, 14, 20$. Overfitting artifacts are observed when N becomes too large (here $N > 10$), resulting in unstable probability distributions for $N = 14, 20$. **b** Mean $\langle T_c \rangle$ of the probability distribution as a function of the number of bins N. The dashed line shows the value obtained by assuming a Gaussian distribution of T_c. **c** Variance $\langle T_c^2 \rangle^{1/2}$ of the same probability distributions.

observation that a probability distribution of T_c can reproduce the field and temperature dependence of $\langle M \rangle$ suggests that the observed local inhomogeneities could be explained by local variations of T_c, typical for magnetic films with local disorder and granular structures. Similar observations of a low FM ratio are also reported by Averyanov et al. [117] using non-local X-ray magnetic circular dichroism measurements. However, in contrast to the presented model, Averyanov et al. propose the coexistence of AFM and FM order in this material as a possible microscopic mechanism. The next section provides a detailed analysis of the nanoscale magnetic texture to elucidate the microscopic magnetic description. Before delving into this analysis, the section on the average magnetic properties of single-layer EuGe$_2$ concludes with a discussion of the observed low or vanishing uniaxial in-plane anisotropy.

4.3.4. Uniaxial In-Plane Anisotropy

In Section 4.3.1 it is shown that single-layer EuGe$_2$ exhibits an easy-plane anisotropy, where the spin orientation of the Eu ion aligns parallel to the sample surface. An unresolved question concerns the presence of a possible additional uniaxial in-plane

anisotropy, as this factor determines the theoretical model for the 2D EuGe$_2$. Two main observations suggest a very low in-plane anisotropy: first, the orientation of the magnetization follows the applied external field, indicating that the Zeeman energy is significantly larger than the intrinsic anisotropy (Fig. 4.3), second, the system exhibits a low or vanishing coercive field with $B_{\text{coer}} < 1.3$ mT (Fig. 4.5 a). These observations are consistent with previous reports of low or vanishing anisotropy [144].

In a simple magnetostatic description, the coercive field of an in-plane magnetized film can be directly related to a uniaxial in-plane anisotropy K_u according to the Stoner-Wohlfarth model [159]. The energy of such a homogeneous FM film contains two terms, Zeeman and anisotropy energy, which depend on the orientation of the magnetization M:

$$\Delta E(\varphi) = E_{\text{anisotropy}} + E_{\text{Zeeman}}$$
$$= K_u V \sin(\varphi - \theta) - B_{\text{ext}} M V \cos\varphi \qquad (4.5)$$

where V is the volume of the magnetized film, φ is the angle between M and the external magnetic field B_{ext}, and θ is the angle between the anisotropy axis and B_{ext}. The magnetization orients such that the energy is minimized at a given B_{ext}. In general, in a hysteresis measurement, the magnetization does not follow the external field directly because the anisotropy energy provides an energetic barrier to the rotation of the magnetization. This barrier is only overcome at the coercive field. The magnitude of the coercive field then depends only on the strength of K_u and the direction of its axis θ, being largest when B_{ext} and the anisotropy axis are parallel ($\theta = 0$).

To estimate an upper bound for K_u for single-layer EuGe$_2$, micromagnetic simulations are performed that resemble the magnetic properties and experimental con-
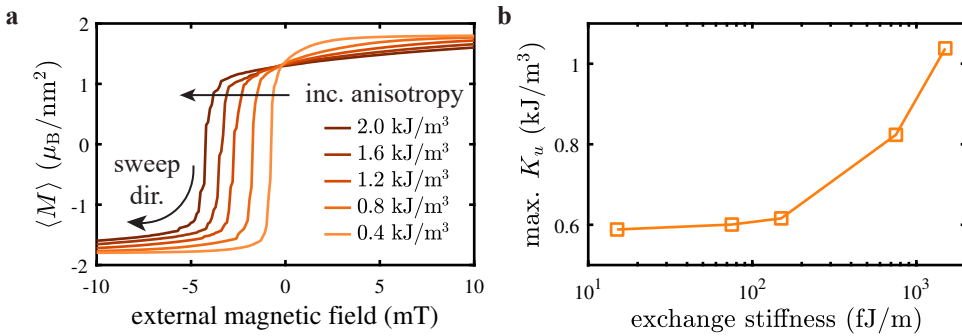

Figure 4.7.: Estimate of the Upper Bound of the Uniaxial In-Plane Anisotropy by Micromagnetic Simulations. a Micromagnetic simulations of different external magnetic field sweeps with varying uniaxial in-plane anisotropy. The higher the assumed anisotropy of the system, the higher the coercive field. **b** Upper bound of the uniaxial in-plane anisotropy estimated from the upper bound of the coercive field of the data shown in Fig. 4.5 a with $B_{\text{coer}} < 1.3$ mT as a function of the assumed exchange stiffness. As expected from the Stoner-Wohlfarth model, the exchange stiffness has no significant influence on the upper bound of the anisotropy.

ditions of the field dependent measurements of the average magnetization $\langle M \rangle$.[3] The simulations are performed using the MuMax3 software package, which calculates the time- and space-dependent magnetization in nanoscale magnets using finite-difference discretization [160–162]. The EuGe$_2$ layer is approximated by a 0.2 nm thick layer, comparable to its lattice site, with lateral dimensions of several nanometers. The magnetization value is set according to the experimentally determined magnetization for a given temperature. The exchange stiffness A_{ex} is estimated from the critical temperature T_{c} and the lattice constant a of the EuGe$_2$ layer to $A_{\mathrm{ex}} \approx k_{\mathrm{B}} T_{\mathrm{c}} / 2a \approx 1.5 \, \mathrm{pJ/m}$ [79, p. 235].

Using this MuMax3 model for the single-layer EuGe$_2$, the inversion of the magnetization as a function of K_u is simulated, and the resulting coercive field is used to set an upper bound on K_u, that is consistent with the upper bound of the coercive field extracted from the measurement (Fig. 4.5 **a**). Because the direction of the anisotropy axis θ is unknown, the film is approximated by small areas with uniform but randomly distributed θ. The areas are obtained by a Voronoi tessellation with structure sizes of $\approx 80 \, \mathrm{nm}$, reflecting the characteristic length scales of the observed magnetic texture (details in Section 4.4.1). As expected from the Stoner-Wohlfarth model, an increasing uniaxial anisotropy K_u provides a stronger energetic barrier to the field reversal of the magnetization (Fig. 4.7 **a**), resulting in a larger coercive field B_{coer}. Using the experimentally determined upper bound of $B_{\mathrm{coer}} < 1.3 \, \mathrm{mT}$, the uniaxial in-plane anisotropy is found to be smaller than $K_u < 0.7 \, \mathrm{kJ/m}^3$, corresponding to $< 0.3 \, \mathrm{\mu eV/Eu}$ ion. This is a remarkably low K_u, because magnetic anisotropies are typically in the range of a few tens to several hundreds microelectronvolts per unit cell [163]. As expected from the Stoner-Wohlfarth model, the bound depends only weakly on the exact exchange stiffness A_{ex}, since even a two orders of magnitude variation results in a variation of about 50 % for the anisotropy (Fig. 4.7 **b**), justifying the initial basic estimate. Note that this bound determined here is limited by the resolution of the vector magnet used for the experiments, and it is not excluded that the true uniaxial anisotropy is significantly smaller.

In the limit $K_u \to 0$, the theoretical description of the system transitions to the 2D-XY spin model, where a breakdown of FM order is expected, and instead long-range spin correlations occur, described by the Berezinskii-Kosterlitz-Thouless (BKT) transition [164–166]. This system is theoretically described by a lattice consisting of spin vectors $\mathbf{S_r}$ of fixed length, confined to the sample plane and sitting at a position $\mathbf{r}$ where they can rotate freely. The state of each spin is defined by a single angle $\varphi_{\mathbf{r}}$ relative to an arbitrary axis. The Hamiltonian $\hat{H}$ of the system is expressed by

$$\hat{H} = -\frac{JS}{2} \sum_{|\mathbf{r}-\mathbf{r}'|} \cos(\varphi_{\mathbf{r}} - \varphi_{\mathbf{r}'}) \tag{4.6}$$

where J is the exchange constant and S is the magnitude of the spin vector [164]. Although the energy is minimized for parallel alignment of neighboring spins, favoring FM order, similar to the isotropic spin model [84], the spin wave excitation spectrum is gapless, leading to the destruction of FM order even at $T \to 0$ [166]. However, the 2D-XY Hamiltonian permits long-range spin correlations, which are established by

---

[3]micromagnetic simulations are performed by B. Gross.

the metastable formation of vortex-antivortex pairs, expressed by two vortices with opposite vorticity $q \in \mathbb{N}_0$, described by

$$\oint \varphi(\mathbf{r}) \, d\mathbf{r} = 2\pi \, q. \tag{4.7}$$

The formation of these pairs leads to a non-zero spin correlation length below a critical temperature T_c and resembles a phase transition [165, 166].

However, long-range FM order in the ideal 2D-XY spin system can be stabilized, for instance, by symmetry-breaking external magnetic fields B_{ext} or finite-size effects. The former introduces an effective anisotropy axis through the Zeeman energy, opening a gap in the spin wave spectrum that allows for ferromagnetic ordering [22]. Finite sample sizes similarly constrain the spin wave spectrum, and FM order is established once the dimensions of the sample decrease below the spin correlation length of the system. This is a typical scenario even for micron-sized samples [89]. Once the FM order is stabilized, the magnetization can be described by the typical scaling parameters β and γ as in Eq. (3.3). The obtained values for single-layer EuGe$_2$, $\beta = 0.250(27)$ and $\gamma = 2.78(42)$, are in good agreement with empirically reported values for low in-plane anisotropy systems of $\beta = 0.227$ and $\gamma = 2.2$[116] and theoretical estimates of $\beta = 0.231$ and $\gamma = 2.4$ [158]. However, Eq. (3.3) does not describe the breakdown of FM order as B_{ext} approaches zero field, and consequently the disordered model for EuGe$_2$ is expected to hold only for non-zero fields. To describe the breakdown towards zero-field conditions, further theoretical and experimental work is required to accurately describe the transition of single-layer EuGe$_2$ to 2D-XY physics.

Nevertheless, the reasonable agreement of the model with the data shown in Fig. 4.5, the agreement of the scaling parameters reported in literature, the low coercive field, and the breakdown of FM order at zero field indicate that single-layer EuGe$_2$ may indeed be a suitable material system to study 2D-XY physics in the future. The next section focuses on the nanoscale magnetic texture that prevents the observation of 2D-XY physics on length scales accessible to S-NVM. It is shown how the texture results from the proposed critical temperature distribution describing a disordered 2D magnet.

4.4. Magnetic Grain Structure

In the preceding sections, several observations indicate that disorder within the single layer of EuGe$_2$ is an important contribution to the observed stray field: The magnetic texture on the film suggests local variations in magnetization (Fig. 4.3 **c** and Fig. 4.4 **a**). The dependence of the average magnetization $\langle M \rangle$ on the external magnetic field implies a coexistence of PM and FM order in the film (Fig. 4.5 **a**, also [117]). In addition, the absence of a sharp critical transition suggests a local distribution of T_c (Fig. 4.5 **c**). The latter two observations are consistent with a disordered FM model as discussed in Section 4.3.3. In this section, the magnetic texture is examined in more detail and a spatial interpretation for the disordered model is formulated. It is found that a magnetic grain structure with varying T_c adequately describes the anomalies observed on single-layer EuGe$_2$.

4.4.1. Nucleation of the Magnetic Texture

High resolution images, with a pixel size of $10\,\mathrm{nm}$, capturing the magnetic texture are obtained at various sample positions and under different experimental conditions (Fig. 4.8). The texture is independent of the magnetic field history and the typical length scale of the inhomogeneities is about $80 - 150\,\mathrm{nm}$. The spatial pattern is characteristic of a local variation of the magnetization strength.

The nucleation of the magnetic texture is found to be independent of the magnetic field history, thus it is not a spontaneous process, but is determined by the local environment of the sample, for example by defects or grains. To elucidate the phenomenology of the nucleation process, the magnetic texture is initialized by a field cooling cycle (Fig. 4.8 **a**) and by inversion of the external field (Fig. 4.8 **b**). The former process destroys the initial FM order by heating the sample for $10\,\mathrm{min}$ to $> 10\,\mathrm{K}$ above its T_c. The latter process reinitializes the order by reorienting the direction of the FM phase. No change in the magnetic texture is observed in either measurement. This behavior is typical of defect structures that act as pinning sites for domain formation or the formation of different magnetic phases, or grain structures that exhibit local variations in the magnetic properties. Structural irregularities of the Ge substrate are a likely source of the defect structure, such as atomic terraces, which have been reported in previous work on this system [144]. Such terraces separate different regions of the magnetized film with a boundary given by the atomic step. The exact microscopic environment of each region would then give rise to locally varying magnetic properties, for example induced by finite-size effects [17].

The observed spatial pattern is characteristic of inhomogeneities with length scales of $80 - 150\,\mathrm{nm}$ caused by a variation in magnetization strength. The characteristic length scale is estimated from the statistics of the Fourier image (Section 3.3.3 and Appendix A.2 for more details). The mean spatial frequency $\langle k \rangle$ corresponds to a typical length scale of $78(12)\,\mathrm{nm}$ of the pattern shown in Fig. 4.8. However, the length scales vary between $80 - 150\,\mathrm{nm}$ at different positions and geometries, indicating that the overall underlying defect or grain structure is not homogeneous across the entire substrate.

An elongation of the magnetic texture is observed, which is perpendicular to the external field and the NV direction. This is consistent with a local variation in mag-
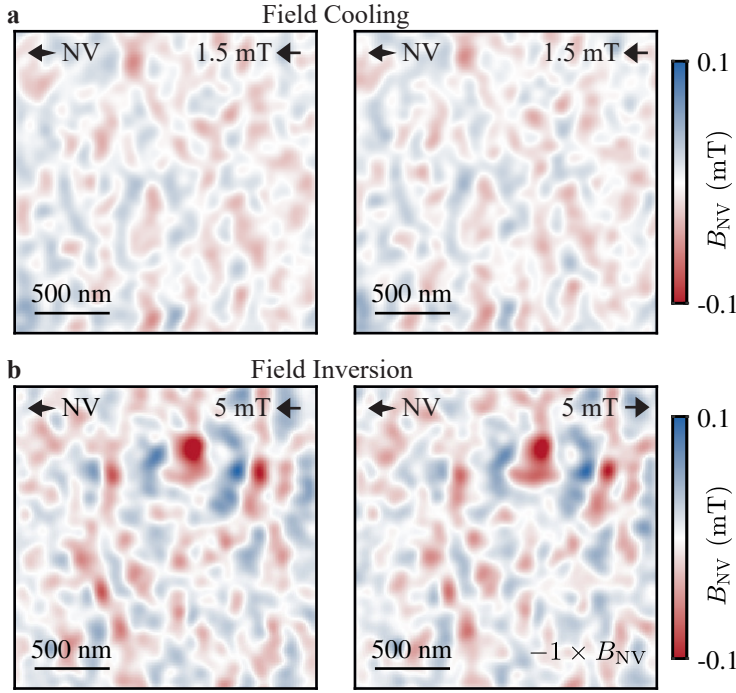
Figure 4.8.: Nucleation of the Magnetic Texture. a Consecutive measurements at the same spatial position in the center of a rectangular structure, taken at $T = 4.5\,\mathrm{K}$ and $B_{\mathrm{ext}} = 1.5\,\mathrm{mT}$. Between the measurements the sample is heated for $10\,\mathrm{min}$ to $> 10\,\mathrm{K}$ above its T_{c}. **b** Consecutive measurements at the same spatial position in the center of a circular structure, taken at $T = 4.5\,\mathrm{K}$ and $B_{\mathrm{ext}} = \pm 5\,\mathrm{mT}$. To facilitate comparison, the color bar of the second image is inverted.

netization strength, but inconsistent with a variation in magnetization orientation. The latter would result in a more isotropic stray field pattern, which is inconsistent with the observed magnetic texture (see also Section 3.3.3). Furthermore, the stabilization of locally varying magnetization orientations requires a non-zero uniaxial anisotropy K_u, which would lead to an observable coercive field, contradicting the field dependent measurements of $\langle M \rangle$ (Fig. 4.5 **a**). In contrast, the local variation of the magnetization strength is consistent with a local variation of T_{c}, because at a given temperature such a variation results in a variation of the degree of FM ordering and thus of the magnetization strength. Similarly, the coexistence of different magnetic phases, such as PM/AFM and FM regions, results in a variation of the magnetization strength, which is also consistent with the observed stray field pattern.

4.4.2. Simulation of the Magnetic Texture

To replicate the stray field texture, the model of a disordered 2D magnet determined from the measurements of the average magnetization $\langle M \rangle$ (Fig. 4.5) needs to be translated into a spatial representation. In the following, the observed distribution
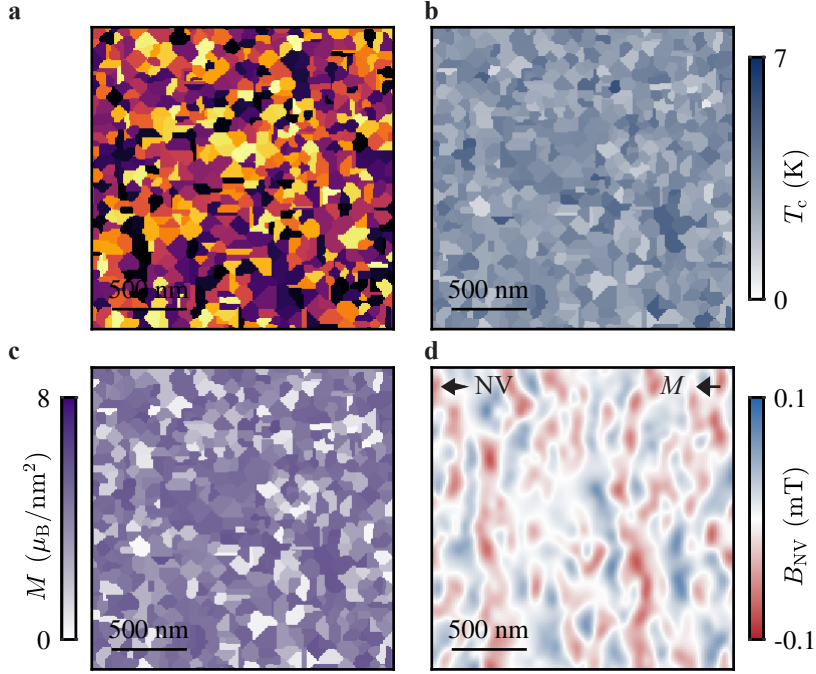
Figure 4.9.: Workflow of the Simulation of the Magnetic Texture. a Voronoi tessellation of the area reflecting the geometric parameter determined from the statistics of the Fourier spectrum. **b** Each tile is assigned a critical temperature T_c according to the probability distribution determined from the disordered 2D model (Fig. 4.6). **c** At a given temperature and external field, the T_c of each tile is converted into a homogeneous magnetization according to the Eq. (3.3). For the map shown, the PM and FM contributions are added to each individual tile. **d** The resulting magnetization map is converted to a stray field map using the previously determined NV parameter.

of critical temperatures is interpreted as a spatial separation of homogeneous areas, each exhibiting a single, random critical temperature T_c.

Initially, the magnetized film is divided into small tiles using a Voronoi tessellation (Fig. 4.9 **a**), a standard method for simulating nanocrystalline samples or grain structures. Random seed points are distributed across the simulation area, and the geometric cells are constructed by assigning each spatial point to its nearest seed. Consequently, each cell contains all points that are closer to a specific seed than to any other seed. For a random seed distribution, the size distribution of the cells resembles a Poisson distribution, which is an acceptable approximation of typical size distributions in nanocrystalline samples [167]. The seed density is chosen so that the resulting stray field image has the same mean spatial frequency $\langle k \rangle$ as the measurements of the stray field texture (details in Appendix A.2).

Next, each cell is assigned a critical temperature according to the distribution obtained by the disorder model (Fig. 4.6). Since the exact distribution depends on
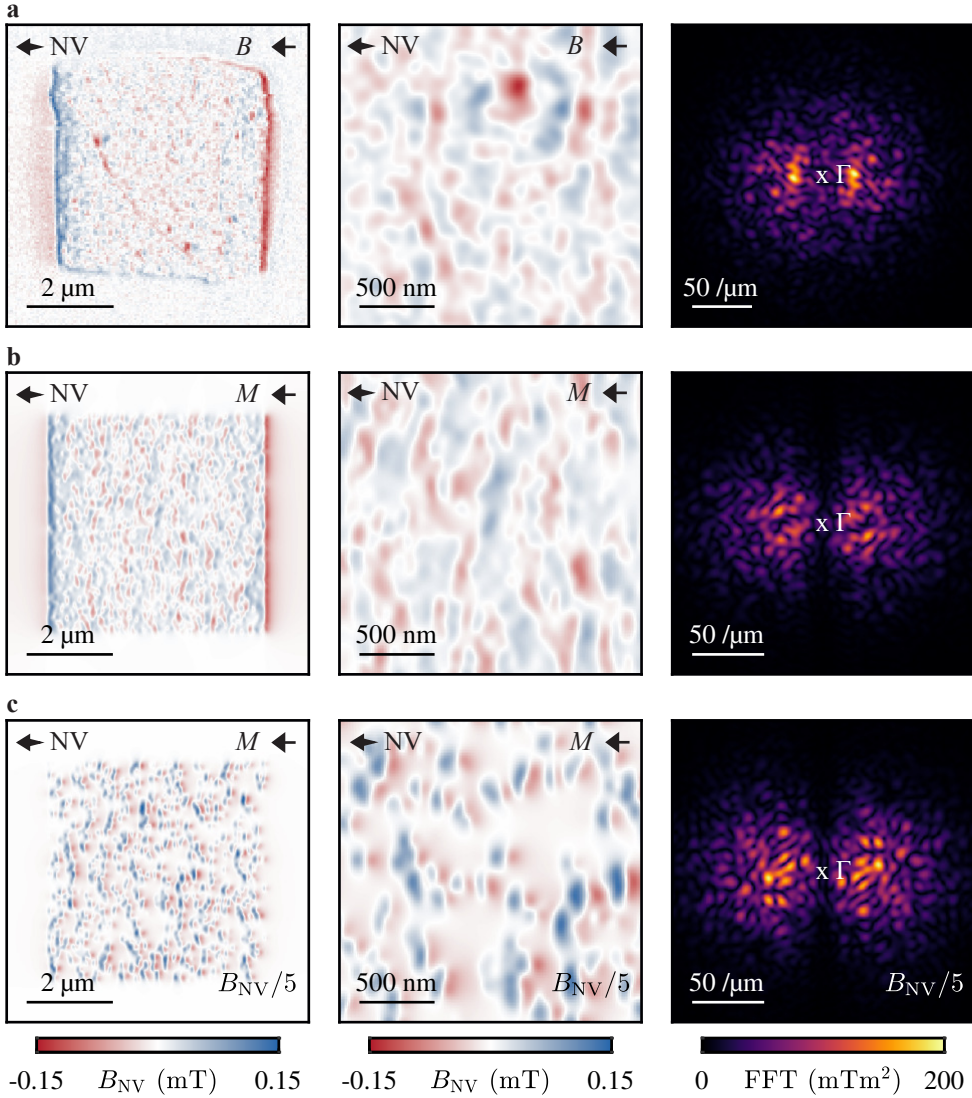
Figure 4.10.: Comparison Between the Data and the Simulation. a Measurement of the stray field from the rectangular structure (left), its internal magnetic texture (middle), and the corresponding Fourier image (right). Γ indicates the origin of the Fourier spectrum. Measurements are taken at $B_{ext} = 5\,mT$ and $T = 4.5\,K$. **b** Simulation of the data assigning to each tile of the corresponding Voronoi tessellation both a PM and a FM contribution according to the disordered model of single-layer $EuGe_2$. **c** Simulation of the data interpreting the PM and FM contributions obtained by the model as spatially separated regions. The stray field is scaled by a factor of five to facilitate comparison.

the discretization of the probability distribution, $p(T_c)$ is approximated by a Gaussian distribution reflecting the numerically robust mean $\langle T_c \rangle$ and its variance $\langle T_c^2 \rangle^{1/2}$. The corresponding T_c-map (Fig. 4.9 **b**) is converted to a magnetization map using Eq. (3.3) with the parameter determined by the disordered model, as summarized in Table A.1. The temperature T and the magnetic field B_{ext} are set according to the experimental conditions (Fig. 4.9 **c**). Using the previously determined NV parameters $d_{\text{NV}}, \varphi_{\text{NV}}, \theta_{\text{NV}}$, and the easy-plane anisotropy of the magnetization, the stray magnetic field is calculated using standard Fourier techniques (Fig. 4.9 **d** and Section 3.3.1). The resulting stray field images are analyzed by the statistics of the field and spatial frequency distribution, with uncertainties estimated by several simulation runs using nominally the same input parameters.

The macroscopic measurement of the average magnetization (Fig. 4.5) does not define how to incorporate the observed coexistence of FM and PM order into the model. Two scenarios are considered: first, spatially separated regions with FM and PM order, and second, regions with simultaneous FM and PM order.

In the first scenario, the different contributions are interpreted as spatially separated regions, implying that PM and FM phases coexist within the film. This coexistence of separated phases is proposed by Averyanov et al. [117], but is also compatible with a grain structure description where individual grains possess either FM or PM order. For this modeling, each tile is assigned either a PM state described by the Brillouin function Eq. (4.3) or an FM state described by the Arrott-Noakes equation (Eq. (3.3)) according to the experimental FM ratio $p_{\text{FM}}/p_{\text{PM}} = 16.4(43)\%$ with p_i being the probability to find either FM or PM order. To maintain the correct average magnetization, the magnetization of each tile is scaled according to its probability, with $M_{\text{FM}}^{\text{tile}} = M_{\text{FM}}/p_{\text{FM}}$ and similarly $M_{\text{PM}}^{\text{tile}} = M_{\text{PM}}/p_{\text{PM}}$. Although such a model reflects the correct $\langle M \rangle$ and Fourier characteristics, it fails to accurately describe the stray field statistics because it results in localized spots of large local magnetization as the main source of the stray field (Fig. 4.10 **c**). This leads to an overestimation of the maximum stray field strength by a factor of five and to a too inhomogeneous stray field at the structure edge compared to the measurements. Consequently, the hypothesis of two separate types of phases or grains coexisting within the film is incompatible with the data.

In the second scenario, the PM and FM contributions are assigned simultaneously to each individual tile. This model accurately reproduces key statistical parameters of the stray field statistics of the data, including the variance of the stray field $\langle B_{\text{NV}}^2 \rangle_{\text{model}}^{1/2} = 19.1(11)\,\mu\text{T}$ and the mean spatial frequency $\langle k \rangle_{\text{model}} = 18.8(6)\,\mu\text{m}^{-1}$, which are in reasonable quantitative agreement with the data ($\langle B_{\text{NV}}^2 \rangle_{\text{data}}^{1/2} = 23.2(14)\,\mu\text{T}$, $\langle k \rangle_{\text{data}} = 19.8(6)\,\mu\text{m}^{-1}$, respectively). In addition, the stray field from the structure edge is well captured by the model (Fig. 4.10 **b**). Overall, the model is compatible with the $\langle M \rangle$ measurements and the observed magnetic texture.

Although the simultaneous PM and FM order of each tile describes the acquired data, it raises the question of how to interpret such an order. One plausible explanation is that each tile possesses an internal magnetic structure, with parts of the tile being FM ordered and other parts being PM ordered, with the typical size of these parts being significantly smaller than d_{NV}. A likely internal structure for a tile is given by a grain structure with a core-shell structure, where only the center of

the grain forms a stable FM core, surrounded by a PM-ordered shell near the grain boundary. A plausible origin for such a grain boundary is the reported terraces in the Ge substrate [144]. Using the obtained dimension d_{grain} and the FM ratio, the core diameter d_{core} is estimated using

$$\frac{d_{\text{core}}^2}{d_{\text{grain}}^2} \approx \frac{M_{\text{FM}}}{M_{\text{FM}} + M_{\text{PM}}} \tag{4.8}$$

and results in $d_{\text{core}} \approx 30\,\text{nm}$ for the investigated sample. The core-shell model implies that the FM ratio is grain size dependent and increases with increasing d_{grain}. Therefore, if there is a way to control d_{grain}, S-NVM could indirectly test this hypothesis, as the ratio should change in accordance with a change in the Fourier spectrum of the magnetic pattern. However, such a test is beyond the scope of this thesis.

4.4.3. Magnetic Field Dependence of the Magnetic Texture

The dependence of the magnetic texture on the external magnetic field B_{ext} further confirms that the texture is spatially fixed and does not evolve with field changes. Notably, the strength of the stray field variance does not follow the behavior of the average magnetization $\langle M \rangle$, indicating that the film becomes magnetically more homogeneous with increasing magnetic field (Fig. 4.11). This trend is qualitatively reproduced by simulating the pattern as a grain structure with varying T_{c}, although quantitative differences remain at both low and high B_{ext} (Fig. 4.12).

Multiple stray field images are acquired on a rectangular structure to study the field dependence (Fig. 4.11). Due to the limited performance of the NV sensor in strong perpendicular fields, two separate NV tips are used: A standard $\langle 100 \rangle$ tip is used for low B_{ext}, and a special in-plane $\langle 110 \rangle$ tip is used for high B_{ext}, resulting in two different data sets. Each set is recorded on a different region of a rectangular structure, while maintaining a constant scan position within each set. The data sets are analyzed according to the procedure described in Appendix A.2.

No spatial evolution of the texture is observed with B_{ext}, and the mean spatial frequency $\langle k \rangle$ remains constant (Fig. 4.11 **b**). This strengthens the interpretation that the texture does not form spontaneously, but is pinned by the local environment. The absence of an evolution indicates local disorder and a variation in the magnetic properties of the film, as opposed to a pinned separated phase or domain picture. In the latter case, switching events of single units are expected to be the underlying mechanism for the film to become more homogeneous [168]. However, such events locally alter the observed stray field pattern, leading to an evolution of the pattern with B_{ext}.

It is worth noting that the elongation of the texture is more pronounced in the data set recorded with the $\langle 110 \rangle$ tip compared to the $\langle 100 \rangle$ tip (Fig. 4.11 **c, d**). This is an artifact of the NV orientation: The $\langle 110 \rangle$ tip is more sensitive to the in-plane stray field component of the texture, which is expected to be less isotropic than the out-of-plane component (Fig. 3.2 **b**). However, the average $\langle |k| \rangle$ is independent of the NV orientation and thus serves as a reliable indicator of the structural dimensions of the magnetic texture (Appendix A.2).

The dependence of the stray field variance $\langle B_{\text{NV}}^2 \rangle^{1/2}$ on B_{ext} (Fig. 4.11 **a**) shows a different scaling than $\langle M \rangle$ (Fig. 4.5 **a**) and becomes relatively more homogeneous
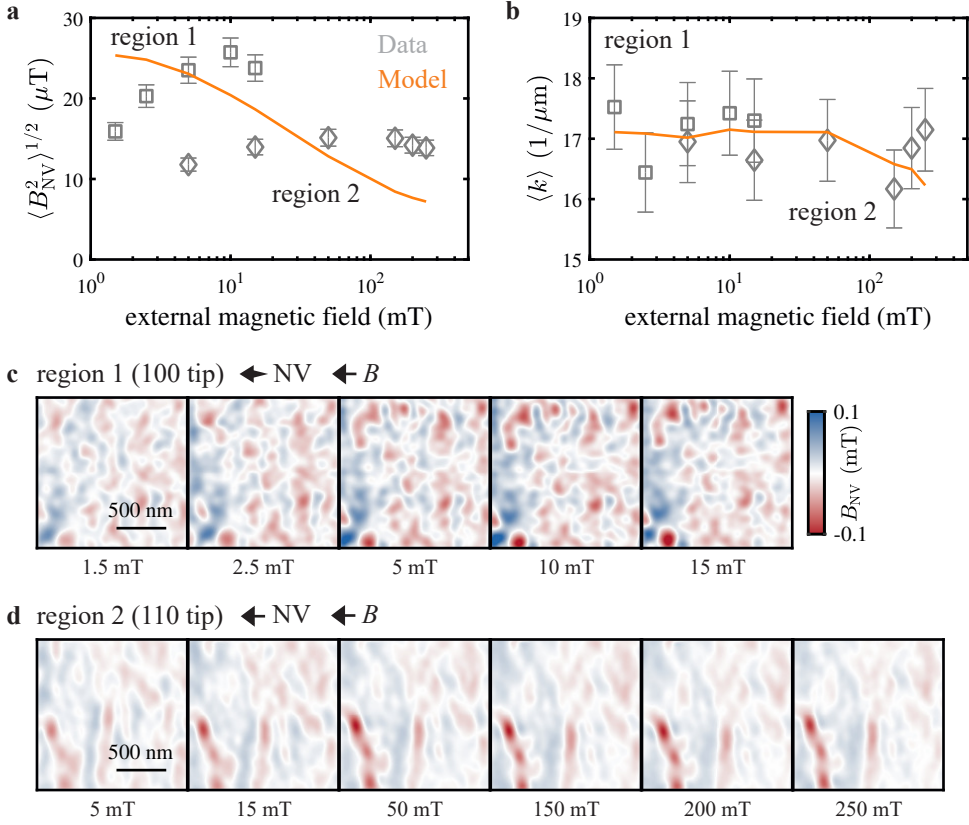
Figure 4.11.: Field Dependence of the Magnetic Texture. a Dependence of the variance of the stray field $\langle B_{NV}^2 \rangle^{1/2}$ on the external magnetic field B_{ext} of two different regions on the rectangular structure acquired with a standard $\langle 100 \rangle$ tip for low B_{ext} (c) and a special in-plane $\langle 110 \rangle$ tip for high B_{ext} (d). The line shows the prediction of the disorder model, which is only valid for non-zero $B_{ext} \gg 0$. **b** Corresponding mean spatial frequency $\langle k \rangle$ of the data sets. **c** Magnetic texture as a function of B_{ext} acquired with a $\langle 100 \rangle$ tip at region 1 on the rectangular structure. **d** Magnetic texture as a function of B_{ext} acquired with a $\langle 110 \rangle$ tip at region 2 on the rectangular structure. The color bar of the data sets c and d is identical.

with increasing field. Both data sets of the stray field variance exhibit a similar qualitative trend: at low fields $\langle B_{NV}^2 \rangle^{1/2}$ increases strongly, since the FM order requires stabilization by a Zeeman-induced anisotropy, as discussed in the previous section. Unlike $\langle M \rangle$, which continues to increase at higher B_{ext}, $\langle B_{NV}^2 \rangle^{1/2}$ saturates at moderate B_{ext} and then starts to decrease at higher B_{ext}. Thus, the texture becomes more homogeneous with increasing field relative to $\langle M \rangle$. This trend can be understood by a varying T_c in different regions: At lower magnetic fields $\partial M / \partial B_{ext}$ and its dependence on T_c are larger compared to higher fields. Ultimately, at even higher fields, the magnetization converges to M_{Sat} independent of T_c, resulting in a homogeneous

magnetic film.

Notably, although both data sets of the field dependent texture exhibit the same qualitative trend, their quantitative strength of $\langle B_{\mathrm{NV}}^2 \rangle^{1/2}$ differs significantly by a factor of two (Fig. 4.11 **a**). This deviation cannot be explained by the different NV orientations, since the latter have only a small influence on $\langle B_{\mathrm{NV}}^2 \rangle^{1/2}$. Similarly, the consistent mean spatial frequency in both data sets indicates consistent NV-sample distances. Therefore, it is likely that the deviation results from the different spatial positions, indicating that the degree of magnetic inhomogeneity itself is not completely homogeneous over the entire sample area.

Using the probability distribution for the critical temperature $p(T_{\mathrm{c}})$ obtained from the analysis of the average magnetization $\langle M \rangle$, the corresponding magnetization distribution $p(M)$ at a given temperature T and external field B_{ext} is given by

$$p(M)\,\Delta M = p(T_{\mathrm{c}}) \left(\frac{\partial M(T_{\mathrm{c}}, B_{\mathrm{ext}}, T)}{\partial T_{\mathrm{c}}} \right)_{B_{\mathrm{ext}}, T} \Delta T_{\mathrm{c}}. \tag{4.9}$$

For $T = 4.5\,\mathrm{K}$, different magnetization distributions are shown in Fig. 4.12 **a**. As expected, $\langle M \rangle$ increases with increasing B_{ext} because the stabilizing effect of the Zeeman energy becomes larger. In addition, B_{ext} aligns the PM contribution in the direction of B_{ext}. In contrast to $\langle M \rangle$, the variance $\langle M^2 \rangle^{1/2}$ decreases with increasing B_{ext} because the distribution becomes narrower for high external fields.

This behavior can be understood as a result of the variance in T_{c}, which describes the magnetic inhomogeneities. A difference in T_{c} does not affect the saturation magnetization M_{Sat}, which is the same for all grains in the model. Therefore, in the limiting case for $B_{\mathrm{ext}} \to \infty$, the distribution in M converges to a homogeneous film. The main effect of a varying T_{c} is that the saturation behavior of each grain is different, meaning the lower T_{c}, the less external field is required to fully saturate the FM order. Since near the critical temperature and close to zero field, the magnetic susceptibility $\partial M/\partial B_{\mathrm{ext}}$ is largest, small differences in T_{c} result in relatively larger differences in M, resulting in a broader magnetization distribution and larger $\langle M^2 \rangle^{1/2}$ compared to larger B_{ext}, where the susceptibility is smaller. Overall, the proposed model thus reflects the same qualitative field dependence as the single-layer EuGe$_2$, since for both the data and the simulation the increase in $\langle M \rangle$ is accompanied by a decrease in the inhomogeneities (as expressed by $\langle B_{\mathrm{NV}}^2 \rangle^{1/2}$ for the data and $\langle M^2 \rangle^{1/2}$ for the simulation).

To quantitatively compare the magnetic inhomogeneities in the model and the data, $\langle M^2 \rangle^{1/2}$ of the model and $\langle B_{\mathrm{NV}}^2 \rangle^{1/2}$ of the data must be related. Using the equivalent Voronoi tessellation, which reflects $\langle k \rangle$ of the data, there exists a unique Gaussian distribution of M (characterized by $\langle M^2 \rangle^{1/2}$) that reproduces the $\langle B_{\mathrm{NV}}^2 \rangle^{1/2}$ of the data (details in Appendix A.2). This $\langle M^2 \rangle^{1/2}$ is chosen for the comparison shown in Fig. 4.12 **b**. Similarly, the same Voronoi tessellation can be used to simulate the magnetic texture using the obtained $p(M)$ of the model, determining the resulting $\langle B_{\mathrm{NV}}^2 \rangle^{1/2}$ and $\langle k \rangle$ of the model used for the comparison shown in Fig. 4.11 **a, b**. All statistical parameters are summarized in Table A.3.

The model and data show good quantitative agreement for $\langle k \rangle$ and $\langle B_{\mathrm{NV}}^2 \rangle^{1/2}$ at moderate fields, but significant quantitative deviations remain at low and high external magnetic fields. As expected for both simulation and data, $\langle k \rangle$ is fully reproduced
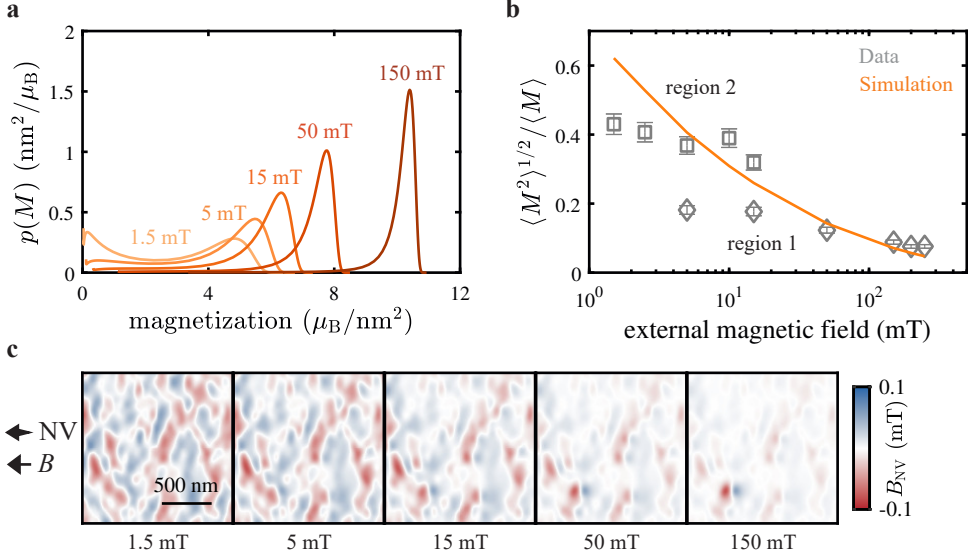
Figure 4.12.: Field Dependence of the Magnetization Distribution. a Probability distribution of the magnetization as a function of B_{ext} at $T = 4.5\,K$ using Eq. (3.3), the corresponding model parameters, and the distribution of T_c determined from the analysis of $\langle M \rangle$. **b** Evolution of the relative variance of the magnetization $\langle M^2 \rangle^{1/2}/\langle M \rangle$ with B_{ext} for the simulation (line) and the data. **c** Simulation of the stray field texture with B_{ext} for single-layer EuGe$_2$.

within the estimated uncertainties, since the spatial frequencies do not depend on the underlying mechanism of the magnetic inhomogeneity and only reflect the geometry of the pattern. Moreover, at moderate fields $B_{ext} = 5 - 50\,mT$, the magnitude of $\langle B_{NV}^2 \rangle^{1/2}$ is well captured and the deviations between model and data are smaller than the differences within the two data sets at different positions themselves. However, at low fields, the model predicts overly large values of $\langle B_{NV}^2 \rangle^{1/2}$, indicating that the low-field behavior and the resulting breakdown of FM order are not captured in the proposed model, as discussed in the previous section. Conversely, at high fields, the model predicts a more homogeneous film compared to the data. A possible explanation is that, in addition to the grain structure, there are defects that alter the saturation magnetization, such as voids in the film or AFM-coupled islands of bilayer EuGe$_2$. Such defects would follow the scaling of $\langle M \rangle$ and thus become more pronounced at high fields. To account for the offset of $\Delta \langle B_{NV}^2 \rangle^{1/2} \approx 5 - 10\,\mu T$, a defect area of about $5 - 10\,\%$ (estimated from Fig. A.3 **d**) is sufficient, which is consistent with the M_{Sat} obtained by the model compared to the fully polarized EuGe$_2$ layer.

   In summary, although the model does not exactly match the observed stray field quantitatively, it captures the qualitative trend and describes the correct magnitude of the stray field pattern. The deviations are of similar order of magnitude as the deviations between different data sets from various regions, making the proposed description of EuGe$_2$ as a disordered 2D magnet with locally varying T_c a

reasonable model to describe both the macroscopic $\langle M \rangle$ and the magnetic texture characterized by $\langle M^2 \rangle^{1/2}$.

4.5. Summary and Outlook

In this chapter, the nanoscale magnetism of single-layer EuGe$_2$ is investigated using scanning NV magnetometry. The results reveal that its magnetic properties are well described by a disordered 2D magnetic film.

The growth of the magnetic material on a patterned substrate by MBE enables the simultaneous determination of the macroscopic average film properties and the investigation of the nanoscale magnetic inhomogeneities. A lithographic patterning process is developed in which geometries of well-defined lateral shape are etched into the Ge substrate by reactive ion etching prior to the established MBE process. This allows the realization of appropriate geometries to study the properties of the EuGe$_2$ layer: The easy-plane anisotropy of the material is confirmed on a circular geometry, while the magnetization as a function of external magnetic field and temperature is determined on a rectangular structure. Although only an upper bound on the coercive field is determined, the observed breakdown of the FM order towards zero field is indicative of magnetic systems with low uniaxial in-plane anisotropy approximated by the 2D-XY spin model. An upper bound on this anisotropy is estimated using a micromagnetic model for the film.

Given the local magnetic inhomogeneities observed in the film, a description for a disordered 2D magnet is developed using the general Arrott-Noakes equation and a probability distribution of the critical temperature T_c. This model describes the average magnetization $\langle M \rangle$ at non-zero external fields where the FM order is stabilized. Similar to previously published results, the reduced saturation magnetization of the EuGe$_2$ film can be understood by a large fraction of spins being PM or AFM ordered. This model is transferred to the local inhomogeneities by defining grains with different values of T_c reflecting the determined distribution for $\langle M \rangle$. The stray field statistics of the inhomogeneities are well reproduced and the qualitative field dependence of the structure is accurately captured. However, this agreement is only achieved when the PM contribution is attributed to each individual grain, rather than assuming the coexistence of two separate grain species. Overall, both the macroscopic average magnetization and the nanoscale inhomogeneities are well described by the developed model of single-layer EuGe$_2$ as a disordered 2D magnet.

Important open questions remain about the origin and physical nature of the observed disorder and how it can be controlled to realize larger homogeneous magnetic regions. One plausible mechanism is that structural disorder from the Ge substrate is transferred into the magnetic film by atomic steps in the substrate, leading to line defects that result in a magnetic grain structure. So far, the material has been studied at the atomic scale, where the honeycomb structure of the material is maintained for several unit cells, although atomic steps have also been observed at this length scale [144]. Atomic force microscopy or scanning tunneling microscopy, both on the substrate and on the magnetic film at length scales of $80 - 150$ nm, are suitable methods to link the observed magnetic inhomogeneities to their structural origin.

The coexistence of FM and PM order within a single grain requires further investigation. One proposed internal spatial structure of a grain involves an FM core surrounded by a PM shell. However, direct imaging of such a structure requires a spatial resolution significantly smaller than the grain size $< d_{\mathrm{grain}}$, a regime currently inaccessible to scanning NV magnetometry and competing techniques. An indirect approach to studying the internal structure is to relate d_{grain} to the FM ratio.

While the proposed description adequately explains the single-layer EuGe$_2$ at moderate external fields, it falls short in describing the breakdown of FM order toward zero field that is expected for the 2D-XY model. Addressing the description of a disordered 2D-XY system, including the finite-size effects related to grain size, poses a complex theoretical problem beyond the scope of the current work. Nevertheless, single-layer EuGe$_2$, with its remarkably low uniaxial anisotropy, serves as a good model system to test various theoretical proposals. In particular, the emergence of vortex-antivortex pairs associated with the BKT transition is a fundamental phenomenon not yet observed in 2D magnets. Since these pairs do not produce any significant stray field, it is difficult to image them directly, but the magnetic noise resulting from the creation and annihilation of these pairs is a suitable target for scanning NV magnetometry.

Further open questions are whether and in which regime the control of the lateral shape can be utilized to manipulate the magnetic state of the EuGe$_2$ film, and how the few-layer magnetism transitions to the AFM bulk properties. Both questions are briefly discussed in the following two outlook sections.

4.5.1. Shape-Engineering

The demonstrated ability to control the lateral geometry of a 2D magnet paves the way for shape-engineering these materials into functional forms. Precise control of the lateral size is crucial for the integration of 2D magnets into more complex heterostructures and represents a severe limitation of mechanically exfoliated magnets, where the size is defined by the flake shape [113]. On the other hand, a well-defined geometry offers the opportunity to engineer anisotropy directions by influencing the dipolar energy resulting from finite-sized samples. This enables, for example, the realization of bistable magnetic elements, the reliable domain formation in T-shaped structures [169], or the creation of more exotic spin textures like artificial spin ices [170].

In 2D systems with low or vanishing crystalline uniaxial in-plane anisotropy, the equilibrium magnetization direction is determined by the field-induced Zeeman energy and the dipolar energy resulting from the stray field generated by a magnetized structure. In an anisotropic lateral geometry, the dipolar energy exhibits a dependence on the magnetization direction, introducing an effective anisotropy axis referred to as shape anisotropy. For elliptical geometries, the long axis a defines the magnetically easy axis, because a stray field arises only from the magnetization component perpendicular to the geometry edge. This projection is smaller for the a-axis compared to the short axis b, which forms the magnetically hard axis. The magnetization direction in an external field can be described in the Stoner-Wohlfarth formalism with a shape-induced anisotropy axis (Eq. (4.5)). Consequently, when the field is applied along the short axis b, the energetic cost associated with tilting the magnetization away from the shape-induced anisotropy axis a results in a canting of the magnetization direction
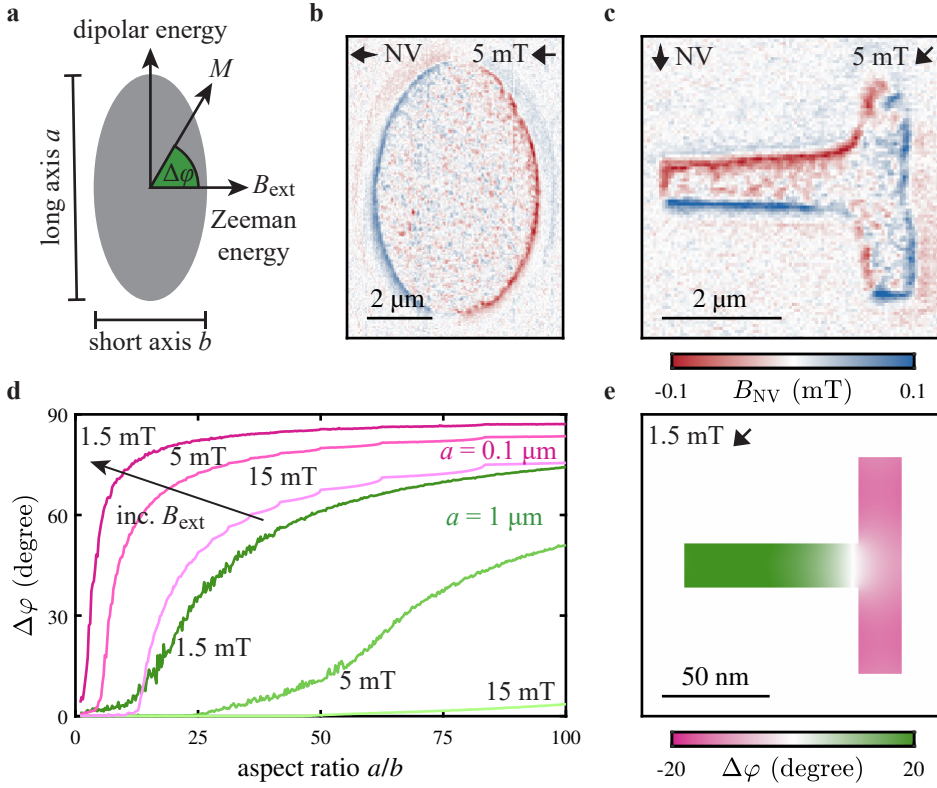
Figure 4.13.: Shape-Engineering of 2D Magnets. **a** For an elliptical geometry without magnetocrystalline anisotropy, the direction of the magnetization is determined by the competition between the field-induced Zeeman energy and the dipolar energy resulting from the lateral geometry. **b** Stray magnetic field arising from an elliptical structure with an aspect ratio of two. At $B_{ext} = 5\,\mathrm{mT}$, the Zeeman energy is the dominant term and no effect of shape anisotropy is observed. **c** Stray magnetic field arising from a T-shape structure with an aspect ratio of five. No effect of shape anisotropy is observed. **d** Canting angle $\Delta\varphi$ as a function of aspect ratio for different micromagnetic simulations of elliptical structures with different long axes, $a = 0.1\,\mu\mathrm{m}$ (pink) and $a = 1.0\,\mu\mathrm{m}$ (green) at different B_{ext} encoded by the color saturation. **e** Micromagnetic simulation of a T-shape resulting in two spatial domains with different magnetization orientations separated by a domain wall.

$\Delta\varphi$ with respect to the field direction (Fig. 4.13 **a**). A similar anisotropy axis can be defined for a rectangular structure or for a T-shape. The latter consists of two spatial regions of the structure with orthogonal anisotropy axes, allowing controlled nucleation of domain walls between these regions [169].

Utilizing the presented pre-patterning approach, such geometries can be achieved with feature sizes down to about $500\,\mathrm{nm}$, limited by the etching process itself and the weak adhesion between the e-beam resist and the Ge substrate (Section 4.2). Stray

magnetic field images of an elliptical and a T-shaped structure (Fig. 4.13 **b, c**) show no deviation between the magnetization direction and the external field, indicating that at these sizes the dominant energetic term remains the field-induced Zeeman energy.

To evaluate the regime of the lateral geometry where shape anisotropy induces significant canting, the micromagnetic model for single-layer EuGe$_2$ is applied to various elliptical structures (Fig. 4.13 **d**). For a long axis $a = 1\,\mu$m, large aspect ratios $\gg 10$ are required to induce a tilt greater than 30°. For moderate aspect ratios < 5, the long axis must not exceed 0.1 μm to induce a significant canting of $\approx 45°$. In conclusion, structure sizes of $10-50$ nm are required to induce a significant shape anisotropy into single-layer EuGe$_2$. This enables the realization of a T-structure as depicted in Fig. 4.13 **e**. There are two separate regions of different magnetization orientation, separated by a domain wall. While the current process is limited to feature sizes of about 500 nm, further development of the lithographic process and etch chemistry should make the required regime accessible by e-beam lithography.

4.5.2. Anomalies of the Bilayer

Macroscopic measurements reveal anomalies of the magnetization also for the bilayer EuGe$_2$ and the few-layer limit EuGe$_2$: a decrease of the transition temperature compared to the bulk value and a non-zero FM moment for the bilayer are reported, in contrast to the bulk description where adjacent layers couple AFM, resulting in a zero net moment for an even number of layers [144].
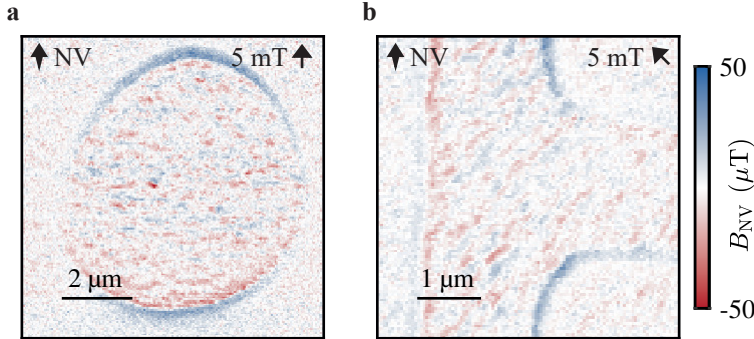
Figure 4.14.: Stray Magnetic Field Images of Bilayer EuGe$_2$. a Stray magnetic field image of a circular structure on which a bilayer of EuGe$_2$ is grown, acquired at $B_{\mathrm{ext}} = 5$ mT and $T = 4.5$ K. The directions of the NV and the external field are indicated by the arrows. **b** Stray magnetic field image of a T-shaped structure under the same conditions as a. Both structures show a clear FM signal with local inhomogeneities similar to the case of single-layer EuGe$_2$.

Stray magnetic field images of bilayer EuGe$_2$ grown on a similar pre-patterned substrate as described in Section 4.2 confirm a non-zero magnetic moment for the bilayer, along with magnetic inhomogeneities resembling those observed for single-layer EuGe$_2$ (Fig. 4.14). Similar to the single-layer case, the direction of the

measured magnetization follows the externally applied magnetic field, indicating that bilayer EuGe$_2$ also exhibits an easy-plane anisotropy with negligible uniaxial in-plane anisotropy. The observed signal strength is approximately one third of that in the single-layer case, suggesting partial compensation of the magnetic moments of both layers, consistent with the expected AFM interlayer coupling. However, to observe a net magnetic moment ΔM, the two layers must exhibit different magnetic properties such that $\Delta M = |M_{\text{top}} - M_{\text{bottom}}| > 0$. The differences between the two layers could stem from distinct surface effects, considering that the bottom layer is in contact with the Ge substrate, while the top layer interfaces with the SiO$_x$ encapsulation. An alternative explanation proposed by Averyanov et al. [154] suggests that AFM and FM phases coexist in the few-layer limit, based on the observation of intrinsic exchange bias. In this picture, the observed net magnetic moment results from regions where the interlayer coupling is FM, which can also explain the local inhomogeneities observed on the sample surface. However, similar to the single-layer case, the strength of the inhomogeneities seems too weak to be consistent with the coexistence of strong magnetic moments from FM areas with a vanishing moment from AFM-coupled areas. Conversely, a description of a disordered bilayer film equivalent to the single-layer allows for weaker magnetic field inhomogeneities that seem more consistent with the stray field images.

In a complementary set of experiments, nanowire magnetic force microscopy (NW-MFM) images are also acquired on the structured bilayer sample[4]. NWs with typical lengths of a few µm and diameters of < 100 nm are excellent force sensors that can also be exploited for magnetic imaging, similar to conventional MFM. The final segment of an NW is grown with a magnetic material so that the NW can interact with a magnetic surface [171, 172]. Contrary to conventional MFM, the NW is brought into contact in a pendulum geometry in which the two mechanical flexural modes are thermally excited. The amplitude A and the frequency shift $\Delta \nu$ are read out optically and are characteristic of the various interactions of the sample surface and the NW tip. In the case of a magnetic surface, $\Delta \nu$ is proportional to the magnetic force and lateral field gradients, but also to the in-phase magnetic susceptibility χ', which describes the induced magnetization by the magnetic NW itself. The damping of the amplitude A/A_0, where A_0 is the free amplitude, is characteristic of the out-of-phase magnetic susceptibility χ'', which is typically associated with dissipative phenomena [150].

NW-MFM images of structured bilayer EuGe$_2$ samples reveal nanoscale magnetic inhomogeneities in both frequency shift and damping of the amplitude oscillation, with a distinct temperature dependence [150]. At $B = 0$ T, the combined resonance frequency shift of the two flexural modes indicates a phase transition starting at around 10 K with a peak at 6.8 K (Fig. 4.15 **a**). Since the magnetic field of the NW tip can be up to tens of mT and no strong signal is observed at the structure edge, $\Delta \nu$ indicates a change in χ' rather than a stray field gradient of the bilayer sample. Similarly, the damping of the oscillation amplitude A/A_0 shows a clear temperature dependence starting at 13 K with a peak at 9.8 K (Fig. 4.15 **b**), associated with emerging dissipative phenomena linked to an out-of-phase magnetic susceptibility χ''. Both

---

[4]NW-MFM measurements are performed by Mattiat and Schneider and presented in [150].
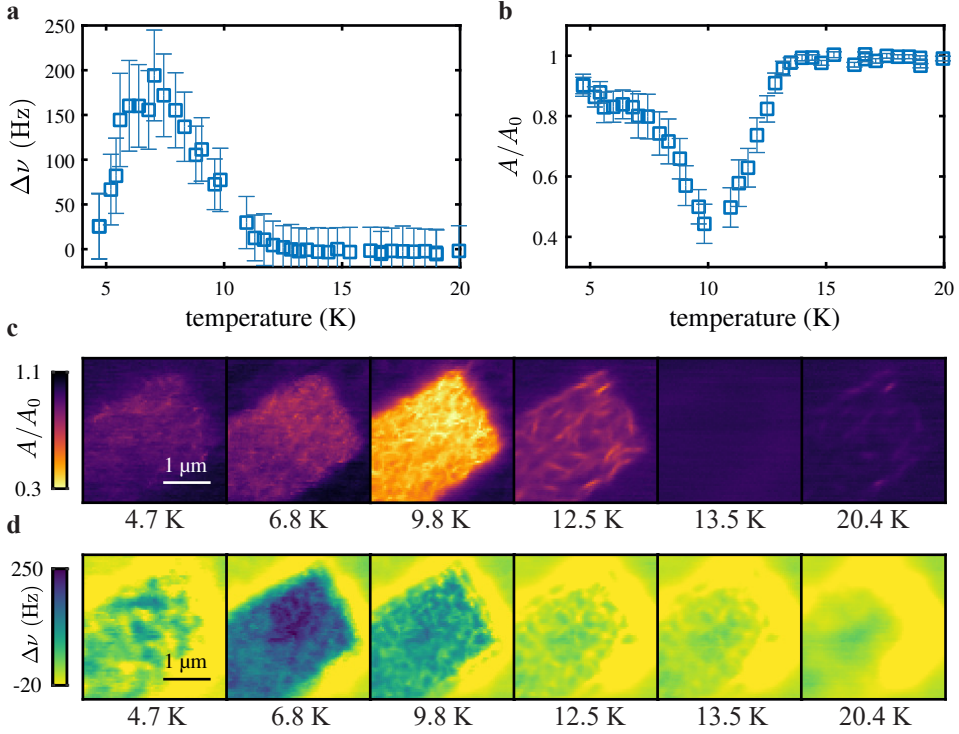
Figure 4.15.: Temperature Dependence of the NW-MFM Signal of the Bilayer EuGe$_2$. **a** Temperature dependent frequency shift $\Delta\nu$ of the two flexural modes of the oscillating nanowire acquired at $B_{\text{ext}} = 0\,\text{T}$, averaged over the area of a rectangular geometry. The signal reaches a maximum at $T = 6.8\,\text{K}$. **b** Temperature dependent attenuation of the amplitude A/A_0 of the two flexural modes of the oscillating nanowire, averaged over the area of a rectangular geometry. The signal reaches a minimum at $T = 9.8\,\text{K}$. **c** Selection of images showing the damping of the nanowire amplitude at various temperatures. Local inhomogeneities are visible with characteristic inverse spatial frequencies of $120 - 900\,\text{nm}$. **d** Selection of images depicting the frequency shift of the nanowire resonance frequency at different temperatures. Local inhomogeneities are visible with characteristic inverse spatial frequencies of $250 - 500\,\text{nm}$ (adapted from [150]).

the temperature dependence of $\Delta\nu$ and A/A_0 indicate a magnetic phase transition coinciding with the appearance of an FM moment in bilayer EuGe$_2$ [144]. In both data channels of the NW-MFM images (Fig. 4.15 **c, d**) of a rectangular geometry, local inhomogeneities are present, indicating an inhomogeneous magnetic state consistent with a magnetic grain structure inferred from the S-NVM data. The spatial frequencies of these images, ranging from $120-900\,\text{nm}$, are slightly higher but of similar order of magnitude to those estimated from S-NVM measurements on the single layer, suggesting a plausible common underlying mechanism. In principle, however, the NW-MFM data are also consistent with other sources of local inhomogeneities,

such as domain formation, coexisting magnetic phases, or other magnetic disorder.

Despite these findings, a comprehensive understanding of bilayer $EuGe_2$ requires further investigation. Three key questions need to be addressed: First, are there signatures of disorder in the bilayer, and how would finite-size effects alter its magnetic properties? Second, can surface effects or disorder modify the interlayer coupling between the top and bottom layers, allowing simultaneous FM and AFM ordering within the film? Third, do surface effects significantly change the magnetic properties of the adjacent layers, leading to different magnetic properties of the top and bottom layers? Overall, the inhomogeneous magnetic state of $EuGe_2$ in the few-layer limit presents intriguing research questions that require future theoretical and experimental work to provide a comprehensive description of the nanoscale magnetism of $EuGe_2$.

5. Origin of Exchange Bias in MnPS$_3$/Fe$_3$GeTe$_2$ Heterostructure

The stacking of two-dimensional (2D) materials to form van der Waals (vdW) heterostructures offers great opportunities to realize novel device architectures with unconventional properties and new physical phenomena. The vdW nature of the interlayer bonding enables stacking of diverse materials without the lattice mismatch and strain constraints of conventional heterostructures. It also allows the realization of atomically sharp interfaces and gives rise to the possibility of controlling the interlayer coupling by stacking order or twist angle [77]. The extension of the class of 2D materials to magnetic 2D materials presents further promising prospects in the field of spintronics and opto-spintronics [78, 108]. For instance, the observation of giant tunneling magnetoresistance in CrI$_3$ due to its ferromagnetic (FM) intralayer and antiferromagnetic (AFM) interlayer coupling [173] enables the realization of spin filters [173] and spin tunneling field-effect transistors [111] as fundamental building blocks for spintronic devices. Finally, the combination of two different 2D magnets with atomically sharp interfaces gives rise to various interfacial phenomena that can modify the magnetic properties of the involved materials by magnetic proximity effects, highlighting the potential of 2D magnetic vdW heterostructures [23].

Exchange bias (EB) is an interfacial phenomenon that typically occurs between an FM and an AFM material interface with Curie temperature T_c and Néel temperature T_N. Field cooling of such a heterostructure can lead to pinning of the FM spins adjacent to the AFM spins, resulting in a shift of the coercive field B_{coer} of the FM layer by an exchange bias field B_{EB} at temperatures $\ll T_N, T_c$. This state is typically metastable, but often persists for multiple hysteresis cycles and converges to a limiting EB field B_{EB}^∞ after a so-called training effect. EB is of technological interest because it can stabilize the magnetic order of a FM or facilitate its switching by controlling the AFM layer, and has been used in read heads of recording devices and magnetoresistive random access memories [174]. Beyond this simple phenomenological description, the underlying mechanism of EB is difficult to describe. In most systems, it involves a magnetic proximity effect changing the magnetism of the adjacent layers, uncompensated surface spins, defects, or grain structures. All of these mechanisms can similarly lead to observable EB, requiring hard-to-obtain knowledge of the interface [175].

The clean and atomically sharp interfaces of 2D vdW heterostructures offer a unique opportunity to study this interfacial phenomenon and open new possibilities to control and tune 2D magnetism. So far, EB has been observed and utilized in several 2D vdW heterostructures: The EB effect in a 2D vdW AFM MnPSe$_3$ and vdW FM Fe$_3$GeTe$_2$ (FGT) heterostructure, attributed to a magnetic proximity effect, enhances the Curie temperature of the FM system, indicating a pathway towards room temperature 2D magnetism [101]. In another heterostructure

formed by the vdW AFM CrSBr and the vdW FM FGT, the exchange bias provides sufficient symmetry breaking to enable deterministic spin-orbit torque switching of the magnetic FGT state at zero magnetic field, offering opportunities for spintronic applications [112]. EB has also been observed in an AFM-ordered $MnPS_3$/FGT heterostructure. However, the origin of this effect remains unclear, because the Heisenberg-type AFM order of $MnPS_3$ does not break the symmetry at the interface. Therefore, it has been proposed that uncompensated surface spins are the origin of the observed EB effect [176].

In this chapter, the origin of the exchange bias in such a $MnPS_3$/FGT heterostructure is investigated by scanning nitrogen-vacancy magnetometry (S-NVM). It is found that already isolated $MnPS_3$ possesses a net magnetic moment in addition to its bulk AFM ordering. The correlation between the temperature dependence of this moment and the dependence of the EB in the heterostructure indicates that this moment is the origin of the observed EB[1].

5.1. Exchange Bias in FGT/$MnPS_3$ Heterostructure

While exchange bias has been observed in FGT/$MnPS_3$ heterostructures [101, 176], the magnetic structure of $MnPS_3$ does not inherently provide magnetic pinning sites at the surface due to the compensating AFM order of the spins within the layer (Section 5.2). Consequently, the AFM order does not favor any particular direction of the FM order in the underlying FGT. Therefore, either the magnetic properties of the $MnPS_3$ are altered in the presence of the FGT by the magnetic proximity effect, or the surface of the material deviates from the ideal magnetic structure, providing uncompensated spins, for example by defects or surface effects, as suggested by Hu et al. [176]. An additional anomaly in the magnetic susceptibility is observed at temperatures $T \approx 40\,K \ll T_N$ by different groups, leading to proposals of an additional magnetic phase transition: Chaudhuri et al. [178] report an in-plane susceptibility despite the absence of a net magnetic moment. The temperature dependence of the observed electron spin resonance in $MnPS_3$ follows the scaling of 2D-XY model, suggesting a possible BKT transition. Contrary, Han et al. [179] describe a non-zero magnetic moment with a coercive field along the out-of-plane direction, indicating an out-of-plane symmetry. They propose an asynchronous rotation of two AFM-coupled spins due to the broken symmetry caused by the canting of the spin ground state. Although such a rotation can describe their phenomenology, it remains unclear why such a rotation exhibits a hysteresis and a separate phase transition.

In this section, such a heterostructure is investigated and it is found that the occurrence of the exchange bias coincides with the presence of an uncompensated moment in bulk $MnPS_3$, indicating that this moment is the underlying reason for the exchange bias in this type of heterostructure [2]. The sample geometry follows the typical geometry for anomalous Hall effect (AHE) measurements (Fig. 5.1 **a, b**): The heterostructure of the metallic FGT and semiconducting $MnPS_3$ [3] is placed on several electrical

---

[1]the S-NVM results are part of the study led by A. Puthirath Balan [177]

[2]the sample is fabricated and characterized by the collaborators A. Puthirath Balan and A. Kumar (University of Mainz), who also performed the SQUID measurements

[3]both $MnPS_3$ and FGT flakes are grown by the collaborators A. Bonanni (University of Linz) and B. Lotsch (Max-Planck Institute for Solid state Research, Stuttgart)
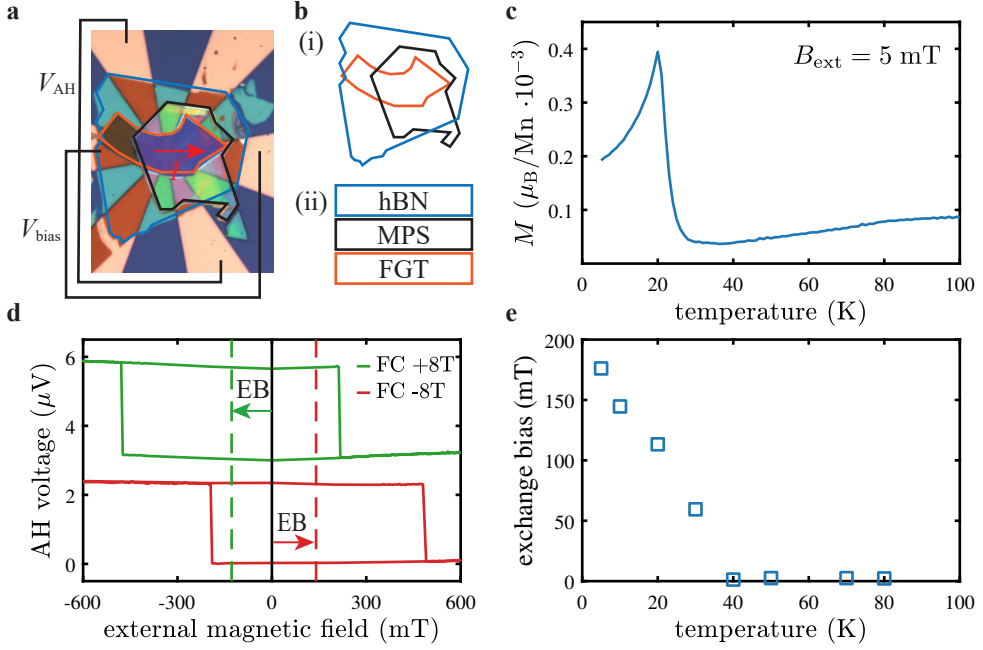
Figure 5.1.: Exchange Bias in FGT/MnPS$_3$ Heterostructure. **a** Microscope image of the investigated device. An FGT flake is electrically contacted in a typical geometry for anomalous Hall effect measurements. A bias voltage is applied to induce a current in the FGT, producing an anomalous Hall voltage perpendicular to the direction of the current flow. A MnPS$_3$ flake is stacked on top of the FGT flake, which is subsequently encapsulated by a hBN flake. **b** Schematic top view (i) and side view (ii) of the investigated flake. **c** Temperature dependence of the magnetization of a MnPS$_3$ bulk crystal at $B_{ext} = 5$ mT. The ordering temperature of the magnetic moment occurs at $T \approx 35$ K $\ll T_N$. **d** Anomalous Hall effect measurements on the FGT/MnPS$_3$ heterostructure after field cooling at ± 8 T, showing a clear exchange bias set by the polarity of the field cooling cycle. **e** Temperature dependence of the exchange bias. The onset of the exchange bias coincides with the ordering temperature of the magnetic moment.

contacts. A bias voltage V_{bias} applied to the FGT induces a current in the flake. Due to the broken time-reversal symmetry caused by the FM ordering, the current also induces a voltage perpendicular to the flow direction V_{AH}, which depends on the FM state of the FGT and can be described in terms of the AHE [180]. The sample is encapsulated by an hBN flake to prevent degradation of the heterostructure.

The anomalous Hall V_{AH} depends on the polarity of the FM ordering, and is thus directly related to the FM state of the FGT. Subsequent hysteresis cycles after field cooling (FC) of the sample at ± 8 T show a clear exchange bias in the heterostructure, as the hysteresis curves are not symmetrically centered around $B_{ext} = 0$ T (Fig. 5.1 **d**). The observed exchange biases of 128 mT (FC at -8 T) and -140 mT (FC at $+8$ T) are set by its polarity, but have the opposite polarity as the FC cycle (negative EB).

As the magnitude of the FC field is larger than the spin-flip field of $MnPS_3$, it seems plausible that the direction is set by the spin-flip state of the $MnPS_3$ after FC.

To further explore the observed EB, the temperature dependence of the EB is investigated. The exchange bias occurs at temperatures below the Nèel temperature of $MnPS_3$ at $T \approx 35\,K \ll T_N = 78\,K$ (Fig. 5.1 **e**). Therefore, the AFM ordering of the $MnPS_3$ cannot be the direct mechanism for the EB. In addition, bulk crystal $MnPS_3$ is investigated in a superconducting quantum interference device (SQUID) magnetometer at $B_{ext} = 5\,mT$ as a function of temperature (Fig. 5.1 **c**). In agreement with previous reports, a phase transition occurs at temperatures around $35\,K$ that results in a non-zero magnetic moment of $MnPS_3$. The occurrence of this moment coincides well with the onset of EB in the heterostructure, suggesting that this moment is the underlying mechanism for EB.

For this, the uncompensated moment observed in bulk crystal must persist in the 2D limit relevant to the heterostructure. Before presenting the S-NVM data of $MnPS_3$ flakes, the magnetic properties of this material are briefly introduced in the following section.

5.2. Properties of $MnPS_3$

$MnPS_3$ is an exfoliable, layered 2D material with AFM ordering of the manganese (Mn) ions below a Néel temperature $T_N = 78\,K$. Its bulk properties have been extensively studied by Mössbauer spectroscopy [181] and neutron diffraction [182], and its properties persist down to the monolayer [183].

$MnPS_3$ possesses a layered crystal structure where the Mn ions form a honeycomb lattice, each covalently bonded to six surrounding sulfur (S) ions that are vertically displaced symmetrically to two equivalent atomic planes (Fig. 5.2 **a, b**). In the center of each honeycomb cell are two covalently bonded phosphorus ions. They are also vertically displaced symmetrically from the Mn ions and bonded to three sulfur ions. Different layers are bonded by vdW forces, with separate layers being horizontally displaced at an angle of $\beta = 107.5°$ to the layer plane. Consequently, $MnPS_3$ forms a monoclinic crystal structure of the $C2/m$ space group with lattice constants $a = 0.607\,nm$, $b = 1.052\,nm$, $c = 0.689\,nm$, $\alpha = \gamma = 90°$ and $\beta = 107.5°$ [182].

In this structural configuration, the Mn ion carries a net magnetic moment of $S = 5/2$. At $T_N = 78\,K$, the material undergoes a magnetic phase transition from a PM to an AFM state. The nearest neighbor coupling is AFM, forming an ideal Heisenberg AFM on the honeycomb lattice, while the weaker interlayer coupling between the spins is FM [182]. The magnetic system exhibits uniaxial anisotropy with the spins almost aligned in the out-of-plane direction. However, the spins are canted about an angle of $\delta = 25°$ to its natural symmetry of the c-axis ($\approx 8°$ to the layer normal, Fig. 5.2 **c**), indicating dipolar and single-ion anisotropies typical for Mn ions. This canting breaks the magnetic inversion center, allowing for a linear magnetoelectric effect [184]. Upon application of an external field along the anisotropy axis, the system undergoes a spin-flop transition at $B_{flop} = 5.3\,T$, showing that the anisotropy energy is significantly smaller than the exchange energy, a property maintained down to the monolayer [183].
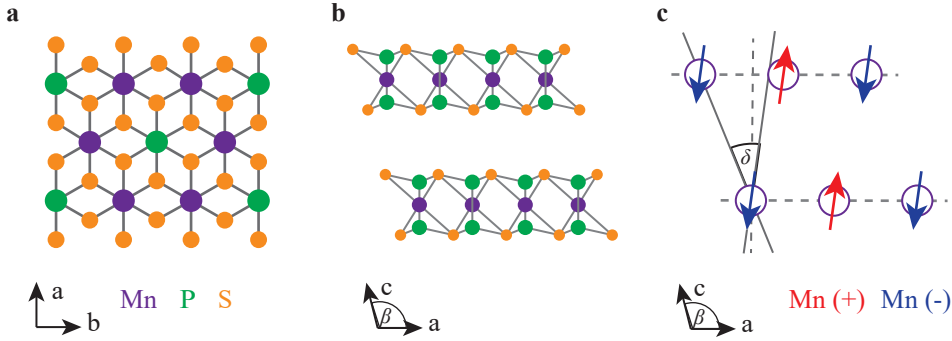
Figure 5.2.: Atomic Structure of MnPS$_3$. **a** Top view of the MnPS$_3$ structure: The manganese (Mn) ions form a honeycomb lattice with two phosphorus (P) ions in the center. Additionally, each Mn ion is bonded to six neighboring sulfur (S) ions, resulting in the overall monoclinic crystal structure of the space group $C2/m$. **b** Side view of the MnPS$_3$ structure. The Mn ions form the central plane of a single layer, which is surrounded by two layers of P and S ions, respectively, which are vertically displaced symmetrically around the Mn layer. The entire MnPS$_3$ layer is vertically displaced along the c-axis, which forms an angle $\beta = 107.5°$ with the layer plane. **c** Magnetic structure of MnPS$_3$: The Mn ions carry a net magnetic moment of $S = 5/2$, which couples AFM to an ideal Heisenberg AFM within the layer. The interlayer coupling between the Mn ions is FM. The moments possess a uniaxial anisotropy, that is canted about $\delta = 25°$ to the c-axis (about 8° to the layer normal).

5.3. Magnetic Moment of MnPS$_3$

So far, the unusual phase transition and the uncompensated moment have only been observed in bulk single crystal MnPS$_3$, and it is unclear whether such a phase transition also occurs in few-layer MnPS$_3$. In this section, it is shown that few-layer MnPS$_3$ does indeed exhibit a non-zero net magnetic moment at low temperatures, and its basic phenomenology is characterized.

5.3.1. Symmetry of the Magnetic Moment

S-NVM is performed on both a heterostructure of FGT/MnPS$_3$ and isolated MnPS$_3$ at a base temperature of $T = 5\,\mathrm{K} \ll T_\mathrm{N}^\mathrm{MPS} < T_\mathrm{c}^\mathrm{FGT}$. No magnetic signal is observed from the FGT flake, while both MnPS$_3$ flakes exhibit a clear stray field signature, indicating a non-zero net magnetic moment of MnPS$_3$.

A microscope image and a schematic of the investigated sample are shown in Fig. 5.3 **a** and **b**, respectively[4]. The sample consists of two different MnPS$_3$ flakes of $\approx 50\,\mathrm{nm}$ height with a lateral extent of about $5 - 10\,\mathrm{\mu m}$, typical for flakes used for spintronics experiments such as the exchange bias studies. One flake is placed on a thin $< 10\,\mathrm{nm}$ FGT flake, significantly larger than the MnPS$_3$ flake, ensuring that

---

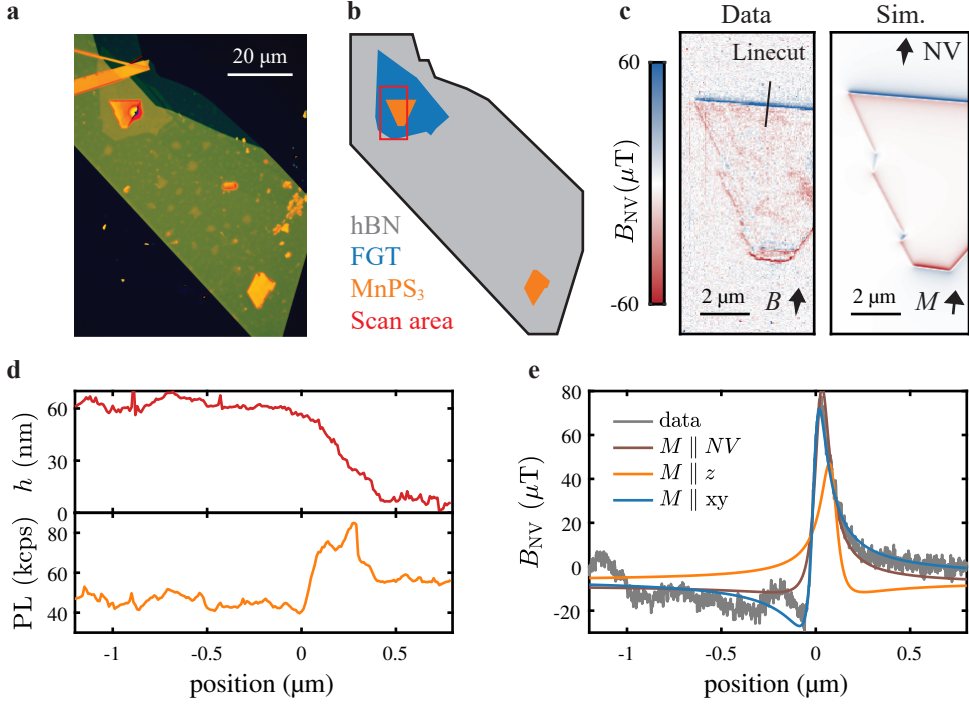[4]the samples are fabricated by the collaborators A. Puthirath Balan and A. Kumar (University of Mainz)

Figure 5.3.: Magnetic Moment of MnPS$_3$. **a** Microscope image of the investigated sample. **b** Schematic of the sample shown in a: The sample consists of two MnPS$_3$ flakes of similar thickness. The upper one is placed on a thin (3-layer) FGT flake. The entire sample is encapsulated by hBN. The red box indicates the scanning area. **c** Stray magnetic field observed on the MnPS$_3$ at an external field $B_{ext} = 150$ mT applied parallel to the NV axis at a base temperature $T \approx 5$ K (left) and the simulated stray field of the flake assuming an in-plane magnetization (right). The FGT flake shows no stray field signature. The line indicates the position of the line cut shown in d, e. **d** Topography and photoluminescence (PL) of the line cut shown in c. The flake has a height of about 50 nm. The PL is quenched on the MnPS$_3$ flake. **e** Stray magnetic field signal of the line cut shown in c. Various magnetization orientations are used to fit the stray field signature. The best fit is found with the magnetization oriented along an in-plane direction.

potential stray magnetic fields from the edge of the FM-ordered FGT do not affect the signal from the interface of the heterostructure. To prevent degradation of the sample due to exposure of air, both flakes are covered with a thin layer of hexagonal boron nitride (hBN) (≈ 10 nm). The sample is stacked on a conventional silicon oxide wafer in the inert atmosphere of a glove box.

Stray field images acquired at $T = 5$ K and $B_{ext} = 150$ mT applied parallel to the NV axis on this sample reveal a similar magnetic signature on the MnPS$_3$ /FGT interface and on the pure MnPS$_3$, indicating an uncompensated magnetic moment of MnPS$_3$. At the same time, the FGT shows no magnetic signal. The latter is unex-

pected since FGT is known to order FM well above the measurement temperature of $5\,\mathrm{K} \ll T_\mathrm{c}^\mathrm{FGT}$ [185], and therefore a strong magnetic signal is expected well above the image noise level. To exclude negative effects on the magnetization of the FGT due to S-NVM, out-of-contact scans are performed to avoid any mechanical stress on the sample and to diminish the laser intensity that exposes the FGT. None of the measurements show any magnetic signal, indicating that disturbances of NV magnetometry are not responsible for the lack of FM ordering of FGT, as suggested by other S-NVM work on pure FGT [138] and by measurements using more invasive widefield NV magnetometry [186], both of which report a clear magnetic signal on FGT. An alternative explanation is oxidation of the flake prior to the measurements and subsequent degradation of the magnetic properties of the sample. This is typical for FGT exposed to air [187], although the investigated samples are encapsulated by hBN.

Although the FGT shows no FM ordering, a clear magnetic signature is observed for both MnPS$_3$ flakes. In the ideal atomic picture (Fig. 5.3 **c**), MnPS$_3$ forms a Heisenberg AFM with neighboring spins compensating each other, hence no net magnetic moment is expected for this material. However, the stray field images (Fig. 5.3 **c** and Fig. 5.4) indicate an uncompensated moment in MnPS$_3$ similar to observations in bulk crystals [178, 179]. To estimate the strength and symmetry of the uncompensated moment, line cuts are taken across the sample edge. The three different magnetization orientations - parallel to the NV axis, parallel to the out-of-plane axis, and parallel to the projection of the NV axis to the in-plane direction - are fitted to the magnetic signal (Fig. 5.3 **e**, fit results in Table A.2). The best agreement between the fit and the data is found for an in-plane orientation of the magnetization, expressed by the lowest mean squared error of the fit. For this model, a magnetization of $M = 2.17(4)\,\mu_\mathrm{B}/\mathrm{nm}^2$ and an NV distance $d_\mathrm{NV} = 44(2)\,\mathrm{nm}$ are found. Using these parameters, a simulation of the stray magnetic field is performed using the shape of the flake (Fig. 5.3 **c**). The good qualitative agreement between this simulation and the measurement, together with the good quantitative agreement of the fit results, indicate that the uncompensated moment points along the in-plane direction and has an easy-plane anisotropy, consistent with the observed anisotropy observed in the bulk measurements by Chaudhuri et al. [178], and contrary to the measurements by Han et al. [179], which indicate an out-of-plane uniaxial anisotropy.

The MnPS$_3$ flake also alters the photonic environment of the NV center, causing a reduction in the collected photoluminescence (PL) intensity when the NV is in contact with the MnPS$_3$ flake. When the line cut across the edge is acquired, the topography and the properties of the NV center are simultaneously (Fig. 5.3 **d**) recorded. The height of the MnPS$_3$ flake is estimated to be about $h = 57.5(45)\,\mathrm{nm}$ from the vertical tip motion. Simultaneously, a decrease in PL intensity is observed. While an average $I_\mathrm{PL}^\mathrm{FGT} = 56.1(13)\,\mathrm{kcps}$ is observed at the hBN/FGT interface, only a $I_\mathrm{PL}^\mathrm{FGT} = 45.8(27)\,\mathrm{kcps}$ is measured at the hBN/MnPS$_3$ interface, resulting in a PL difference of $\Delta I_\mathrm{PL} = 10.3(30)\,\mathrm{kcps}$. The potential presence of magnetic noise at the transition frequency of the NV can drive the spin transition and thus increase the population in the darker upper spin levels [188]. Such a process also acts as a source of decoherence and is accompanied by an increase in the resonance width $\delta\nu$ and a decrease in the optical contrast C. However, within the margin of uncertainty, neither a change in the resonance width $\Delta\nu = -1.5(42)\,\mathrm{MHz}$ nor a change in the

optical contrast $\Delta C = 0.9(12)\,\%$ is observed, indicating that magnetic noise is not the underlying mechanism of the PL quenching. Hence, the drop in PL is due to a change in the photonic environment, leading, for example, to an increase in the NV radiative lifetime or a change in the dielectric properties of the cavity formed by the apex of the diamond tip and the sample interface. Further investigations are required to fully understand this phenomenon, such as a direct measurement of the radiative lifetime of the NV or the dielectric properties of the surface by ellipsometry. However, these are beyond the scope of this work, which mainly focuses on understanding the uncompensated magnetic moment of $MnPS_3$.

5.3.2. Remanence of the Magnetic Moment

To further understand the physical behavior of the uncompensated magnetic moment in $MnPS_3$, its dependence on the magnetic field history is investigated. Close to zero field, both the bulk crystal (SQUID magnetometry) and the investigated flake (S-NVM) exhibit a remanent magnetic moment. However, in the bulk crystal the magnetic moment shows a hysteretic behavior and can be switched, while in the few-layer limit the state of the magnetic moment remains constant for all tested field cycles.

To study the field dependence of the observed magnetic moment, a bulk crystal $MnPS_3$, identical to the crystal used for the sample fabrication, is studied by SQUID magnetometry at $T = 5\,K$ and a magnetic hysteresis loop is obtained as a function of out-of-plane and in-plane field (Fig. 5.4 **a**). Three regimes are observable: At high external fields $B_{ext} > 100\,mT$, the typical field dependence of an AFM with out-of-plane uniaxial anisotropy is obtained: No additional magnetization is induced by an out-of-plane field, because the Zeeman energy for the antiparallel aligned spin is not sufficient to overcome the energetic barrier set by the anisotropy energy until the spin-flop field ($B_{flop} = 5.3\,T$ [183]) is reached, where a magnetization can be induced. Conversely, an in-plane field applied parallel to the hard axis of the magnet leads to continuous canting of the antiparallel spins, resulting in a linear field response. At low external fields $B_{ext} < 100\,mT$, a magnetic moment is observed that shows a linear field response near zero field and saturates at moderate fields ($B_{ext} \approx 100\,mT$), typical of a PM response. The low saturation field indicates a large total PM moment $J \gg 5/2 = S_{Mn}$, which would be significantly larger than the spin moment of the Mn ion S_{Mn} (Fig. 5.4 **a**). Finally, close to zero field, the magnetization of the bulk crystal shows a hysteresis behavior with a remanent magnetization at zero field consistent with an FM ordered uncompensated moment. Remarkably, the uncompensated moment found in bulk crystal does not show a specific symmetry axis, as the remanent magnetic moment is identical for both the in-plane and out-of-plane sweep directions.

A similar hysteresis loop is determined on the $MnPS_3$ flake using S-NVM and a similar remanent magnetic moment is observed, although the moment does not show the same hysteretic behavior compared to the bulk crystal. Four consecutive measurements of the isolated $MnPS_3$ flake are taken with the field applied along the NV direction, following the hysteresis cycle $B_{ext} = 150\,mT \rightarrow -5\,mT \rightarrow -150\,mT \rightarrow 5\,mT$ (Fig. 5.4 **e**). Although the observed magnetization of the flake is inverted at $B_{ext} = \pm 150\,mT$ (sign change of B_{NV} at the edge), the magnetization at $B_{ext} = \pm 5\,mT$ exhibits the same polarity, providing direct evidence for a non-zero re-

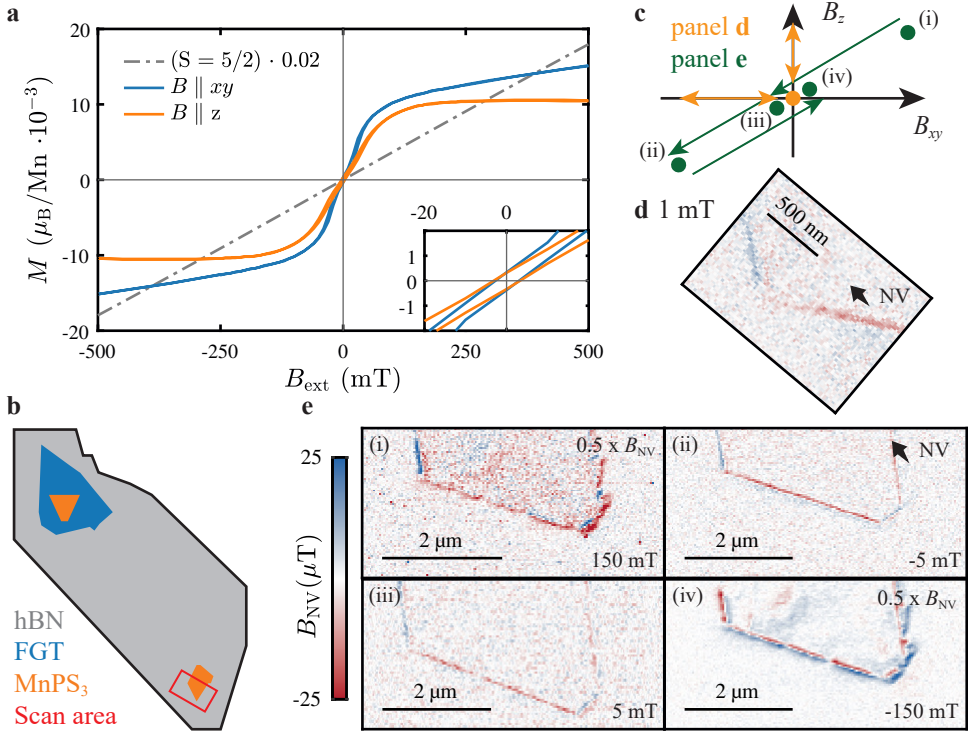**Figure 5.4.: Remanence of the Magnetic Moment of MnPS$_3$.** **a** SQUID magnetometry data taken on a bulk MnPS$_3$ crystal for a full hysteresis cycle of the external field applied along the out-of-plane and in-plane directions. For both directions, the magnetization shows a linear field dependence with a hysteretic behavior at low magnetic fields (inset). For comparison, the PM model for the Mn ion with S = 5/2 is added (scaled by 0.02 for comparison). **b** A schematic of the investigated sample by S-NVM. The red box indicates the scan area. **c** Schematic of the magnetic field history used for the data set in d (orange) and e (green). The arrows indicate the field history, while the circles indicate the measurement positions. **d** Exemplary stray magnetic field map acquired at $B_{ext} = 1\,\text{mT}$ after various field cycles. No change in magnetic state is induced by the magnetic field history. **e** Consecutive stray field images acquired at various external fields applied along the NV direction following a hysteresis cycle. Though the magnetization orientation switches at $B_{ext} = \pm 150\,\text{mT}$, the remanent magnetization remains constant. For comparison, the stray field images at high field are divided by a factor of two.

manent magnetic moment. Interestingly, the polarity of the remanent moment seems to be unaffected by a switch in total magnetization induced by a strong magnetic field. To investigate the possibility of manipulating the remanent moment, a separate set of images is acquired at the same flake at $B_{ext} = 1\,\text{mT}$ with changes in the magnetic field history: Prior to each measurement, either the maximum in-plane field of $B_{ext}^{ip} = \pm 500\,\text{mT}$ or the maximum out-of-plane field $B_{ext}^{oop} = \pm 500\,\text{mT}$ is ap-

plied in either polarity, limited by the maximum field that is reachable with the used vector magnet. In all four measurements, the polarity remains the same as shown in Fig. 5.4 **c**. Consequently, the field required to manipulate the remanent magnetic state must be greater than $B_{flip} \gg 500\,mT$. Potentially, the remanent magnetic moment is bound to the AFM state of the $MnPS_3$. In this case, the required field to flip the moment would be on the order of the spin-flop field $B_{flop} = 5.3\,T$. However, this is in contrast to the bulk measurement, where much smaller fields are sufficient to flip the polarization of the remanent moment.

5.3.3. Field Dependence of the Magnetic Moment

From the measurements of the hysteresis loop of the bulk crystal as well as the isolated $MnPS_3$ flake, it is apparent that the strength of the uncompensated moment shows a strong field dependence close to zero field. Successive images at various external fields show a similar linear dependence as observed in the bulk measurements. The order of magnitude of the strength of the remanent moment and the linear field response is consistent between the bulk and the flake, indicating that the moment is a volume rather than a surface property.
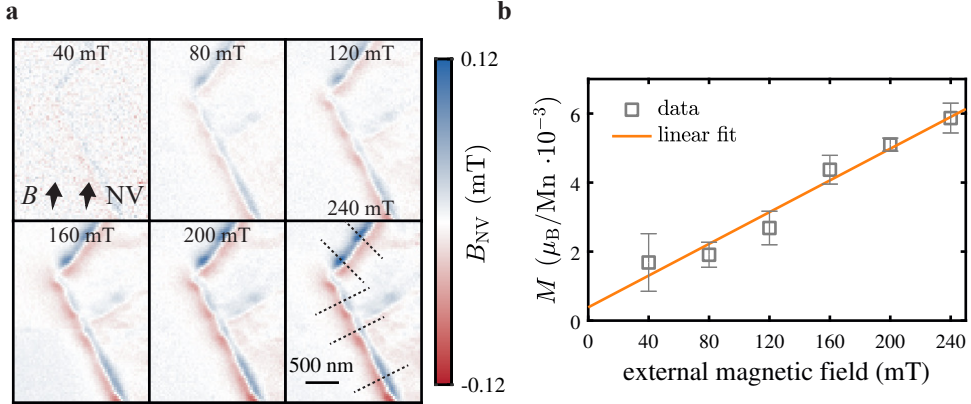

Figure 5.5.: Field Dependence of the Uncompensated Moment of $MnPS_3$. **a** Successive images obtained from the isolated $MnPS_3$ flake at various applied magnetic fields along the NV axis, as indicated by the arrows. The dotted lines at $B_{ext} = 240\,mT$ indicate the positions of the line cuts, used to estimate the signal strength. **b** Signal strength as estimated from the line cuts shown in a. Depicted uncertainties are the standard deviation between the line cuts. The axis has been normalized by the magnetization obtained from the line cut shown in Fig. 5.3 **e**. A linear function is fitted to the data points.

To investigate the field dependence, several images of the isolated $MnPS_3$ flake are acquired at the same spatial position as in the previous section, with the field applied along the NV axis (Fig. 5.5 **a**). With increasing field, the stray field magnitude of the flake increases, but also reveals large spatial inhomogeneities over the range of a few hundred nanometers. The inhomogeneities do not change their spatial location and

are therefore likely bound to the structure or topography of the flake. To account for the inhomogeneities, line cuts are taken at separate positions and the signal strength is estimated from the amplitude of the stray magnetic field signal. The fit to the stray field (Fig. 5.3 **e**) is used to calibrate the stray field amplitude. The total magnetization follows an approximately linear field dependence, so a linear model is fitted to describe the data (Fig. 5.5 **b**).

From the stray field signal itself it is not possible to distinguish between a surface and a volume magnetization of $MnPS_3$. However, the comparison with the SQUID data indicates that the magnetization is a volume property. For comparison, the SQUID data are used to extract a remanent magnetic moment and a linear response for the field dependence near zero field. Assuming a volume magnetization, a remanent moment of $M_{rem}^{SQUID} = 0.30(10) \cdot 10^{-3}\,\mu_B/Mn$ and a linear response of $(\partial M/\partial B_{ext})^{SQUID} = 0.143(3)\,\mu_B/T/Mn$ are found. These values are in the same order of magnitude as those extracted from the flake, which exhibits a remanent moment of $M_{rem}^{flake} = 0.37(35) \cdot 10^{-3}\,\mu_B/Mn$ ($M_{rem}^{fit} = 0.38(35) \cdot 10^{-3}\,\mu_B/Mn$), determined from the signal strength of the remanent moment and the linear fit, respectively, and a linear response of $(\partial M/\partial B_{ext})^{fit} = 0.023(2)\,\mu_B/T/Mn$. The quantitative deviations seem reasonable considering that one measurement is performed on a bulk crystal while the other is conducted on a few-layer flake. The agreement in order of magnitude for both the linear response and the remanent moment indicates that the uncompensated moment is a volume property. Conversely, in the case of surface magnetization, due to the different surface-to-volume ratio between the bulk crystal and the flake, the observed stray field from the flake would have to be significantly larger to agree with the SQUID data.

In summary, the S-NVM measurements on the $MnPS_3$ reveal that the material exhibits a small remanent magnetic moment with a linear field response and an in-plane orientation, contrary to the ideal Heisenberg AFM picture. A similar observation is also made on the bulk crystal with SQUID measurements. The agreement in the order of magnitude of the field response and the remanent moment suggests that this is a volume property. An important inconsistency remains unexplained, as the bulk crystal shows a hysteretic behavior, which is not present in the flake. Hence, the question of how to manipulate this remanent moment in the few-layer limit remains open for further investigation.

5.4. Summary and Outlook

In this section, the origin of the observed exchange bias in the $FGT/MnPS_3$ heterostructure is investigated. In agreement with previous reports on bulk crystal $MnPS_3$, S-NVM reveals the presence of a non-zero uncompensated magnetic moment in the few-layer limit of $MnPS_3$, next to its Heisenberg-type AFM ordering. This moment exhibits an easy-plane anisotropy, aligning its spins within the sample plane. Its strength shows a linear field response with a remanence comparable to bulk crystal measurements, suggesting that the moment is a bulk rather than a surface property. Unlike in the bulk crystal, no hysteretic behavior is observed in the few-layer limit. Consequently, the external field required to switch the polarity of the remanent moment must be greater than $B_{ext} \gg 500\,mT$ in both

the in-plane and out-of-plane directions. This is in contrast to the bulk crystal where such fields are sufficient to reveal a hysteretic behavior, a discrepancy that requires further investigation.

The correlation of the temperature dependence of the uncompensated moment with the temperature dependence of the exchange bias suggests that the moment is the underlying mechanism for the latter. The moment potentially acts as a pinning site for the FM-ordered FGT spins, stabilizing their orientation against the induced Zeeman energy of a counteracting field, giving rise to an exchange bias in the hysteresis cycle. Conversely, due to the symmetry of the AFM order of $MnPS_3$, the compensated AFM-ordered spins cannot act as pinning sites and induce an exchange bias, consistent with the coincidence of the temperature dependence of the moment and the exchange bias. Similarly, an exchange bias induced by a proximity effect at the FGT/$MnPS_3$ interface seems to be an unlikely explanation for the exchange bias, as in this scenario exchange bias would be observed for all temperatures below T_N.

While S-NVM confirms the existence of an uncompensated moment in $MnPS_3$, further research is needed to fully understand its properties. Immediate questions include whether this uncompensated moment is an intrinsic property of $MnPS_3$ or whether it is due to impurities introduced during the crystal growth process. Moreover, as the uncompensated moment is a bulk property that persists in the few-layer limit, it is an open question whether this moment persists down to the single-layer limit and whether it shows a dependence on the layer number. Additionally, to fully exploit the potential for its use in heterostructures and more complex spintronic device architectures, it is necessary to understand how the remanent moment can be manipulated. In particular, it is important to understand whether its polarity is bound to the AFM state of the $MnPS_3$ and thus can be initialized by it, or whether it has an independent coercive field unrelated to the spin-flop field of $MnPS_3$. If it is bound to the AFM state of $MnPS_3$, it could serve as an indirect probe for nanoscale investigations of the magnetic state of $MnPS_3$, which is difficult to do directly due to its compensated AFM order. Finally, since the moment can induce exchange bias in the FGT/$MnPS_3$ heterostructure and does presumably not depend on the details of the FGT interface, $MnPS_3$ may be a suitable material to induce exchange bias in other 2D magnetic systems.

In conclusion, the confirmed existence of an uncompensated moment in the 2D vdW material $MnPS_3$ by S-NVM raises many further questions about the fundamental nature of the moment and opens the prospect of exploiting such a moment for further integration into 2D vdW heterostructures.

6. Conclusion

Two-dimensional magnetic systems represent an emerging research field for both fundamental studies and technological advancement [80]. The stacking of different 2D van der Waals materials with atomically clean interfaces to form heterostructures offers a rich landscape of physical phenomena, such as the proximity effect or the exchange bias [23]. However, due to their atomically thin nature, they exhibit a weak magnetic signal and a fragile magnetic state, posing significant challenges for characterization techniques [24]. In this thesis, scanning NV magnetometry is shown to be a suitable tool for the investigation of this class of materials. S-NVM is capable to shine light on anomalies observed in macroscopic measurements, as demonstrated in the study of the coexistence of different magnetic orders in MBE grown $EuGe_2$ and in the exploration of the origin of the exchange bias in the $MnPS_3/Fe_3GeTe_2$ heterostructure.

In the first part of this thesis, the applicability of S-NVM to the study of 2D magnetism is evaluated. The unique properties of the NV, including its all-optical spin initialization and spin state readout, its long spin coherence, and the linear Zeeman effect of the spin triplet, make it a suitable qubit for precise and calibration-free measurements of the external magnetic field. Integration into an all-diamond AFM tip facilitates the NV to be brought into close contact with a magnetic surface, allowing the recording of the arising stray field with a resolution of tens of nanometers. While the stray field does not uniquely define a 2D magnetization, it can be quantitatively inferred under common experimental constraints. The sensitivity provided is sufficient to detect even weak ferromagnetic order, while the spatial resolution permits the study of various nanoscale phenomena. Although the photophysics of the NV restricts the operating range of S-NVM in an intermediate temperature range $(20-60\,\mathrm{K})$, S-NVM can probe 2D magnets over the entire relevant temperature range from a few kelvins to above room temperature by applying an appropriate external magnetic field. A major limitation for the exploration of the magnetic phase space is the fact that magnetometry is only possible in an external field parallel to the quantization axis of the NV. This requires the use of multiple tips with different NV orientations to probe 2D magnetizations along their intrinsic symmetry axes. Although S-NVM operation requires AFM contact, exposure of the sample to optical power and microwave radiation, the perturbations induced by S-NVM operations are generally negligible, leaving the magnetic state of the sample undisturbed, establishing S-NVM as a competitive imaging technique for 2D magnetic systems.

As a first example, S-NVM is employed to study the single layer of the MBE grown 2D magnet $EuGe_2$. Consistent with previous macroscopic characterizations, the average magnetization is reduced with respect to a fully saturated magnetic layer and exhibits an additional paramagnetic response. $EuGe_2$ is described by an easy-plane anisotropy with negligible uniaxial in-plane anisotropy, as inferred from the vanishing coercive field. Therefore, $EuGe_2$ is a potential candidate for an XY magnet. Additionally, S-NVM reveals a complex, spatially fixed magnetic texture attributed to

structural disorder. Both the macroscopic properties and the microscopic texture are well described by a disordered model based on the general Arrott-Noakes equation and a grain structure with an individual critical temperature for each grain. However, the observed additional paramagnetic response is inconsistent with spatially coexisting magnetic order, but consistent with an intrinsic property of each grain. This could imply an internal structure of such a grain with a PM shell and an FM core below the spatial resolution of S-NVM. Similar disorder is observed in the bilayer $EuGe_2$, suggesting that disorder is crucial for understanding the transition from the bulk properties of $EuGe_2$ to the few-layer limit. Finally, the study concludes by exploring the introduction of an anisotropy axis into the system through the lateral geometry of the 2D magnet. No relevant shape anisotropy is induced with the created geometries, and micromagnetic simulations suggest that structures on the scale of tens of nanometers are required to induce a relevant anisotropy axis in the 2D magnet.

In a second example, the high sensitivity of S-NVM is exploited to elucidate the origin of the exchange bias in the $MnPS_3$/FGT heterostructure. Although the magnetic order of $MnPS_3$ does not provide pinning sites for the FM order of FGT, anomalous Hall effect measurements reveal an exchange bias in FGT. Temperature dependent SQUID magnetometry data on bulk $MnPS_3$ show the appearance of a weak magnetic moment below the Néel temperature, which correlates well with the temperature dependence of the exchange bias. S-NVM confirms the presence of this moment in the few-layer limit relevant to the heterostructure. The moment points along the in-plane direction, and its strength and field dependence are consistent with the moment being a bulk property. Notably, while the orientation of the moment is rotated by the external field, its remanent moment remains unaffected by the field conditions accessible in the setup. It remains an open question how to manipulate this remanent moment. However, field cooling cycles of the heterostructure suggest that the orientation of the moment may be linked to the AFM state of $MnPS_3$. Although the origin of the uncompensated moment itself remains unclear and is subject of further experimental and theoretical work, it presents a plausible mechanism for the observed exchange bias in the $MnPS_3$/FGT heterostructure.

Overall, the two examples presented, along with other work on 2D magnetism using S-NVM demonstrate its viability for exploring this exciting new class of materials. This thesis concludes with a brief outlook on the future of S-NVM for the study of 2D magnetism: What aspects of S-NVM need to be addressed to make the technique more viable for the study of 2D magnets? What open questions in the field of 2D magnetism could be addressed in the future?

Several technical developments are of interest for exploring 2D magnetism by S-NVM. General improvements in the technique in terms of sensitivity and spatial resolution (see Section 2.5 for a discussion of the various viable approaches) will benefit future studies of 2D magnets: While the current sensitivity is already sufficient to detect the weak magnetic signal from single-layer materials, higher sensitivity will speed up the imaging process. Improvements in spatial resolution could facilitate the resolution of the internal structure of spin textures such as skyrmions, domains or grains, although this will require the stabilization of near-surface NVs and novel tip designs. Although the NV is most commonly used for magnetometry, its ground state splitting is also sensitive to electric fields and temperature, allowing nanoscale

imaging of these quantities as well [189, 190]. Multimodal sensing would allow the correlation of the magnetic state with a local electric field or temperature, useful, for example, in nanoscale studies of 2D multiferroics [191]. One of the major advantages of S-NVM is the low impact of the method on the fragile magnetism of the sample. However, the optical and microwave power can still perturb the magnetic state of the sample. By exploiting the ground state level anticrossing, microwave-free magnetometry is feasible [192], and the required optical power can be significantly reduced by resonant excitation [193]. Although such schemes have been demonstrated, further development is required to apply them in relevant measurement scenarios. As seen in Section 3.4.1, the photophysics severely limits the operating range of S-NVM. Since the exact positions of the anticrossings depend on the strain and electric field experienced by the NV, electronic gating of the NV could be used to move the anticrossings to a field and temperature range that is not relevant for a given measurement scenario. Alternatively, other defects in diamond are suitable for single-spin magnetometry, such as the tin-vacancy [194] or the silicon-vacancy center [195], which can circumvent some of the limitations of the NV.

One of the major advantages that S-NVM can offer in the field of 2D magnetism is the ability to quantitatively image nanoscale magnetic phenomena [25]. For example, the observation of domain formation and evolution in $CrBr_3$ has allowed to assign this process to the presence of pinning sites and defects [103]. The study of domain walls and their propagation in more pristine flakes could reveal further fundamental information about the material, such as exchange and anisotropy constants, which determine the micromagnetic behavior. The observation of a magnetic phase wall and its propagation in bilayer CrSBr could be an interesting model system to study the micromagnetic landscape [102].

2D magnets can also host non-trivial chiral spin textures that result from the antisymmetric exchange Dzyaloshinskii-Moriya interaction, as reported in $Cr_2Ge_2Te_6$ [105]. However, such DMIs can also be engineered in 2D vdW heterostructures, where a 2D magnet is stacked on a 2D material containing heavy elements that induce strong spin-orbit coupling [106]. Heterostructures also allow the application of a strong electric field that breaks the inversion symmetry in the 2D material, allowing the existence of chiral spin textures [196, 197]. S-NVM could probe these textures by directly imaging them and thus determine their size, internal structure, or local distribution. Magnetic correlations arising in Moiré patterns also give rise to non-trivial spin textures that are difficult to image directly [99, 198]. Although S-NVM has already shown that it is possible to image a magnetic Moiré pattern in CrI_3 [27], the typical low Moiré periodicity of just a few nanometers pushes S-NVM to its spatial resolution limit. However, the great promise of such patterns in fundamental physics [107], motivates further experiments with S-NVM.

An interesting topic in the field of 2D magnetism is the study of spin dynamics and spin waves, because they allow the determination of important material parameters such as exchange interaction, magnetic anisotropy, spin-orbit coupling, and govern the dynamics of spintronic devices [137]. First experiments using the NV center have been demonstrated to study the spin wave noise spectrum [199] and to directly image their propagation through a magnetic film [19, 20]. However, direct imaging of spin waves by NVs requires that their frequency spectrum overlaps with the electron spin resonance of the NV. This is difficult to achieve in practice since typical spin wave

frequencies are on the order of tens of gigahertz, but AFM 2D $CrCl_3$ shows a spin wave spectrum that could be probed by S-NVM [200]. Instead of directly imaging spin waves, the NV is also susceptible to magnetic noise, e.g. by a reduction of its longitudinal spin relaxation time [188]. This could be used to study the incoherent magnetic noise arising from a thermal spin bath. It could even be used as an indirect measure to study the proposed creation and annihilation of vortex-antivortex pairs associated with the BKT transition in XY magnets [164, 165].

This thesis demonstrates that exploiting quantum theory to realize the unique measurement technique of scanning nitrogen-vacancy magnetometry provides fascinating insights into the emerging field of 2D magnetism. Although many technical challenges remain to be overcome and require further experimental and theoretical afford, the great promise of 2D magnets in both fundamental physics and technological development will motivate and inspire future work of researchers. "The important thing is not to stop questioning. Curiosity has its own reason for existence" (Albert Einstein[1]).

---

[1] *Old Man's Advice to Youth: 'Never Lose a Holy Curiosity*, LIFE Magazine, p. 64 (1955).

A. Appendix

A.1. Experimental Setup

The scanning NV magnetometry setup used to acquire the data of this thesis, consists of a commercial atomic force microscope system (AttoCube, ASC500) with a home-built implementation of NV magnetometry embedded in two different commercial cryostat solutions (AttoCube, attoLiquid1000 and attoDry2200).

For the experiments, NV tips are fabricated according to the recipe published elsewhere [29, 64]. The NV is embedded in an all-diamond atomic force tip, which is shaped into a parabolic reflector with a base diameter of 200-500 nm to facilitate optical collection efficiency. For the high-field measurements discussed in Chapter 4, a commercial tip with the NV axis oriented in-plane (QNami) is used.

For the excitation path, the emission of a 532 nm laser (Laser Quantum GEM) is controlled by an acousto-optic modulator and connected by optical fibers to a home-built optical head. The laser beam is collimated by a 0.81 NA objective (Attocube LT-APO) and subsequently focused onto the NV. A typical laser power of 10-100 µW is applied. The resulting fluorescence is collected by the same objective and separated by a dichroic mirror (Thorlabs DMLP567). The photons are detected by an avalanche photodiode (Excelitas SPCM-AQRH-33) after passing an additional long pass filter (Thorlabs FELH0600).

A microwave signal is used to drive the NV spin transition, which is generated by a signal generator (SRS SG384), modulated and controlled by an IQ modulator (Polyphase Microwave AM0350A), amplified (Minicircuit ZHL-42W+) and transmitted to a bond wire at approximately 50-200 µm distance from the tip (Fig. A.1 **c**). Both the laser AOM and the microwave are controlled by an arbitrary waveform generator (Spectrum instrumentation DN2.663-04).

For AFM operation, the NV tip is mounted on a quartz capillary and glued to a commercial quartz tuning fork (Fig. A.1 **b**). The tuning fork is operated in shear mode with amplitude feedback and is controlled by a commercial AFM driver (Attocube, ASC 500). A typical setpoint for amplitude modulation is 80 % of the free amplitude out of contact. For such a setpoint, no damage of the sample is observed after scanning. The tip and sample are positioned by piezo positioners and piezo scanners (Attocube), providing a scan range of 15 µm x 15 µm at 4.3 K (Fig. A.1 **e**).

To obtain the stray magnetic field image of the sample, the Zeeman splitting of the NV at each pixel is determined using a pulsed optically detected magnetic resonance measurement scheme. The NV is excited with a 500 µs laser pulse to initialize the spin to the $m_s = 0$ state. A near-resonant microwave π-pulse is then applied to the NV, and the resulting spin state is read out by a second laser pulse, which also acts as a re-initialization pulse for the following cycle. A feedback protocol is used to track the resonance frequency of the NV (as described in Section 2.4).

The complete AFM setup is placed inside a sample chamber with a He atmosphere ($100\,\text{mbar}$ at room temperature), which is placed in a cryostat. Two commercial cryostats are used for the experiments: The liquid bath cryostat (Attocube, attoLiquid1000) with a base temperature of $4.3\,\text{K}$ and a $0.5\,\text{T}$ vector magnet (described in detail in [136]) and the closed-cycle cryostat (Attocube, attoDry2200) with a variable temperature insert with a base temperature of $1.8\,\text{K}$ and a $1.0\,\text{T}$ vector magnet.
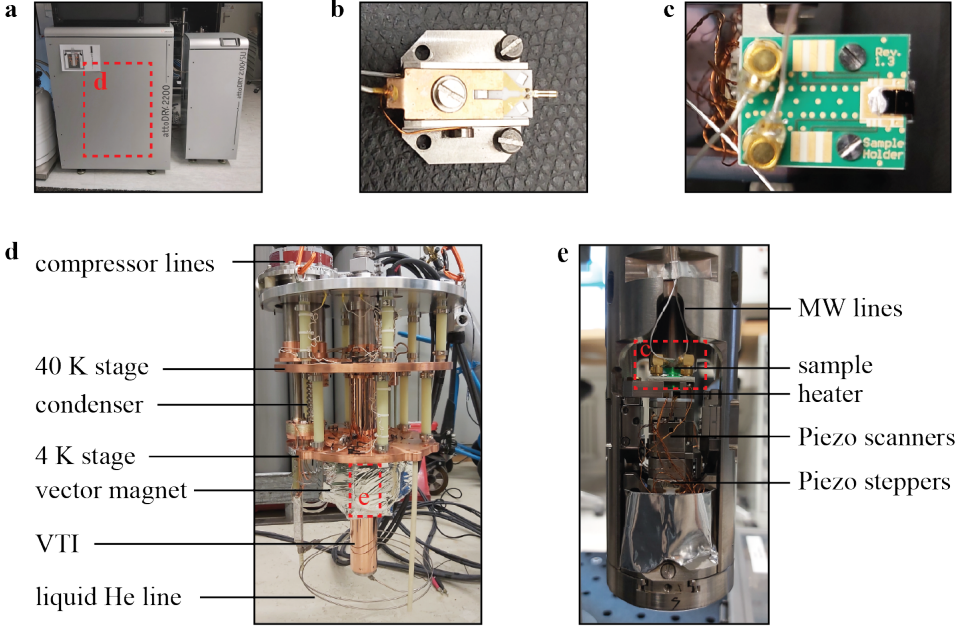

Figure A.1.: Images of the Experimental Setup. **a** The attoDry2200 system installed in the laboratory, consisting of the cryostat and its control unit. **b** The AFM head. An NV tip (as shown in Fig. 2.4 **b**) is attached to a commercial tuning fork. The piezo-driven TF motion results in an electrical signal that is used for AFM feedback. **c** Sample chip: The sample is glued to a PCB that can be contacted with RF lines. An antenna wire is bound close to the area of interest. **d** Inside view of the cryostat: Compressor lines cool the vector magnet and various thermal stages, while the $4\,\text{K}$ stage is used to condense helium for the primary cycle that provides cooling for the sample chamber. **e** Sample stack consisting of the sample chip, a heating stage, and the various piezo scanners and steppers. A similar stack is used to control the tip.

The attoDry2200 operates with two different helium cycles (Fig. A.1 **a, d**): In the primary cycle, helium is compressed by an external compressor and then adiabatically expanded through a heat exchanger, which provides the refrigeration power to cool the vector magnet, a $4\,\text{K}$ and a $40\,\text{K}$ stage inside the cryostat. The temperature limit is set by the liquidation temperature of helium. To achieve an even lower base temperature, the helium circulates through the secondary cycle, which is thermally

coupled to the 4 K stage at the condenser, where the Helium of the secondary cycle is condensed. The liquid helium flows to the inlet of the variable temperature insert (VTI) where it evaporates. The evaporation provides additional cooling power to the VTI, which cools the sample chamber via exchange gas to a base temperature of 1.8 K. The VTI itself contains an external heater that can be used to heat the sample chamber from the base temperature to room temperature, allowing S-NVM over the full temperature range compared to the attoLiquid system where only operation near the base temperature is possible. The sample temperature in both systems is determined by a resistive thermocouple (Cernox) located below the sample and connected to a resistive heater that provides limited additional temperature control in the range of a few kelvin.

A.2. Statistical Analysis of Stray Field Patterns

As discussed in Section 3.3.3, when the changes in magnetization are on the order of the NV distance d_{NV}, a direct reconstruction of the underlying pattern is impossible due to the lack of recorded high spatial frequencies. Nevertheless, a statistical analysis of the stray field pattern is possible. The technical details of such an analysis are presented in the following.
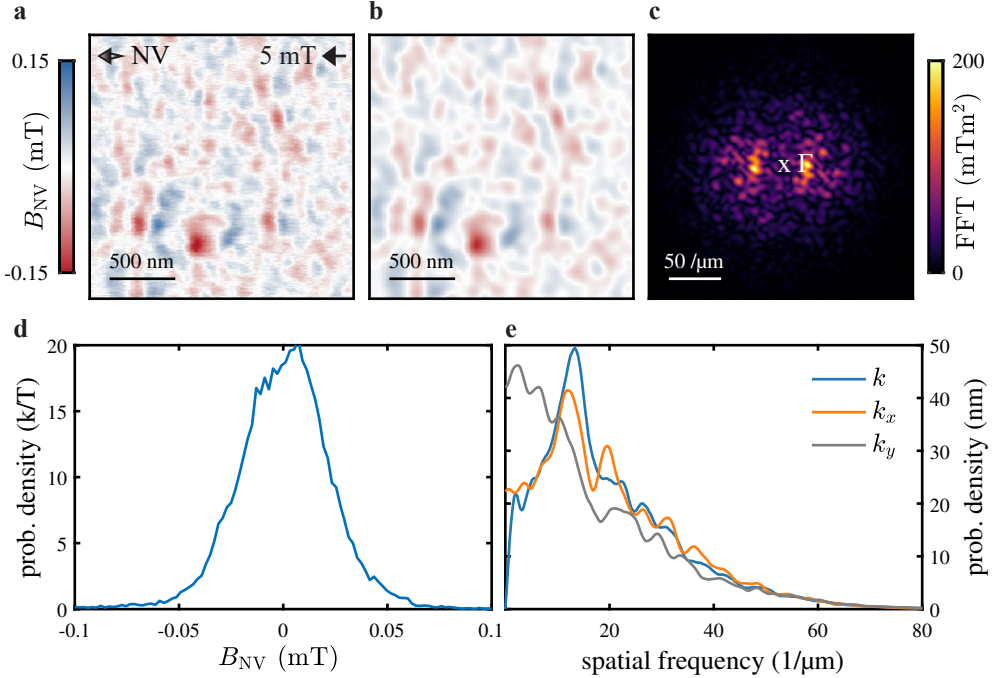

Figure A.2.: Characterization of the Stray Field Pattern. a Raw data of an acquired stray field pattern with pixel size $\Delta x = \Delta y = 10\,\text{nm}$. **b** Stray field pattern after applying a Hanning filter to the data in a. The cut-off frequency is set to the NV distance $k_{cut} = 2\pi/d_{NV}$ (here $d_{NV} = 63\,\text{nm}$). **c** Fourier image of the filtered stray field map b. Γ indicates the origin. **d** Probability distribution of the stray field values shown in the map b. **e** Probability distribution of the Fourier components of the stray field map extracted from c.

To study such patterns, nanoscale magnetic field images are recorded with high spatial resolution (Fig. A.2 **a**). According to the Nyquist theorem, the sampling frequency must exceed $2k_{cut}$ to record the detectable spatial frequencies $k < k_{cut}$. While $k_{cut} = 2\pi/d_{NV}$ is set by the NV distance, a pixel size greater than $\Delta x = d_{NV}/2$ is required. Here, a pixel size of $\Delta x = \Delta y = 10\,\text{nm}$ is chosen to comfortably fulfill this criterion.

In a first step, the distribution of the magnetic field magnitudes and the contained spatial frequencies are extracted. Due to the high sampling rate, the stray field images contain spatial frequencies to which the NV center is insensitive ($k < 2\pi/d_{NV}$)

and thus are artifacts of the experimental conditions. These frequencies are typically rejected by cut-off filters for high frequencies [124]. Here, these frequencies are removed by applying a Hanning filter with the cut-off frequency set by the NV-sample distance d_{NV}

$$
\begin{aligned}
W(k < 2\pi/d_{NV}) &= 0.5 \cdot (1 + \cos(k \, d_{NV}/2)) \\
W(k > 2\pi/d_{NV}) &= 0.
\end{aligned}
\tag{A.1}
$$

The filtered magnetic field image and its corresponding Fourier image (Fig. A.2 **b, c**) are used to extract the probability densities for the magnetic field magnitudes B_{NV} and the corresponding spatial frequencies k, k_x, k_y in the Fourier spectrum (Fig. A.2 **d, e**). These distributions $P(x)$ are characterized by their resulting k-th order moments

$$
\langle x \rangle^k = \int_{-\infty}^{\infty} \left(x - \langle x \rangle^1 \right)^k P(x) \mathrm{d}x,
\tag{A.2}
$$

where $x \in \{B_{NV}, k, k_x, k_y\}$. These moments allow to compare the statistics of different stochastic magnetic field patterns.

Nanoscale stray field patterns indicate local inhomogeneities in the magnetization. In general, three different nanoscale mechanisms (Fig. A.3 **a**) can produce a stray field pattern: a locally varying magnetization strength, magnetization orientation, change of magnetic state, or any combination of these three. The distributions of these inhomogeneities depend on their exact physical origin and can be quite different. In the following, the distributions are restricted to a rather general and basic stochastic model. Stochastic properties are drawn from a Gaussian distribution of the magnetization strength characterized by its variance $\langle M^2 \rangle^{1/2}$, orientation $\langle \varphi^2 \rangle^{1/2}$, or a paramagnetic and ferromagnetic state is drawn from a binomial distribution characterized by its FM ratio. The spatial pattern is generated by a Voronoi tessellation with a characteristic tile size.

To gain an understanding of the stray field pattern resulting from different inhomogeneities, stray field simulations are performed where the characteristic parameters are varied in an appropriate parameter range. Different tilings with different characteristic tile sizes are created. Each tile is assigned a random magnetic property and the corresponding stray field image of the magnetization pattern is calculated using standard Fourier techniques (see Section 3.3.1 for details). For comparison, the assumed NV parameters and the average magnetization are kept constant, as these can typically be well determined in control experiments. The resulting stray field patterns are characterized by their statistical moments according to Eq. (A.2).

The full parameter searches for the three different stochastic models are summarized in Fig. A.2 **c, d, e**. As expected, the first moment of the spatial frequency distribution $\langle k \rangle$ depends mainly on the tiling size of the Voronoi tessellation. Interestingly, this moment is also insensitive to the choice of a particular model (Fig. A.3 **b**), allowing to estimate the underlying geometric parameter without any assumptions about the physical origin of the local magnetization variation. Thus, this establishes the corresponding tiling size for each experimentally observed stray field pattern. Conversely, the stray field strength depends on the magnetic model and can
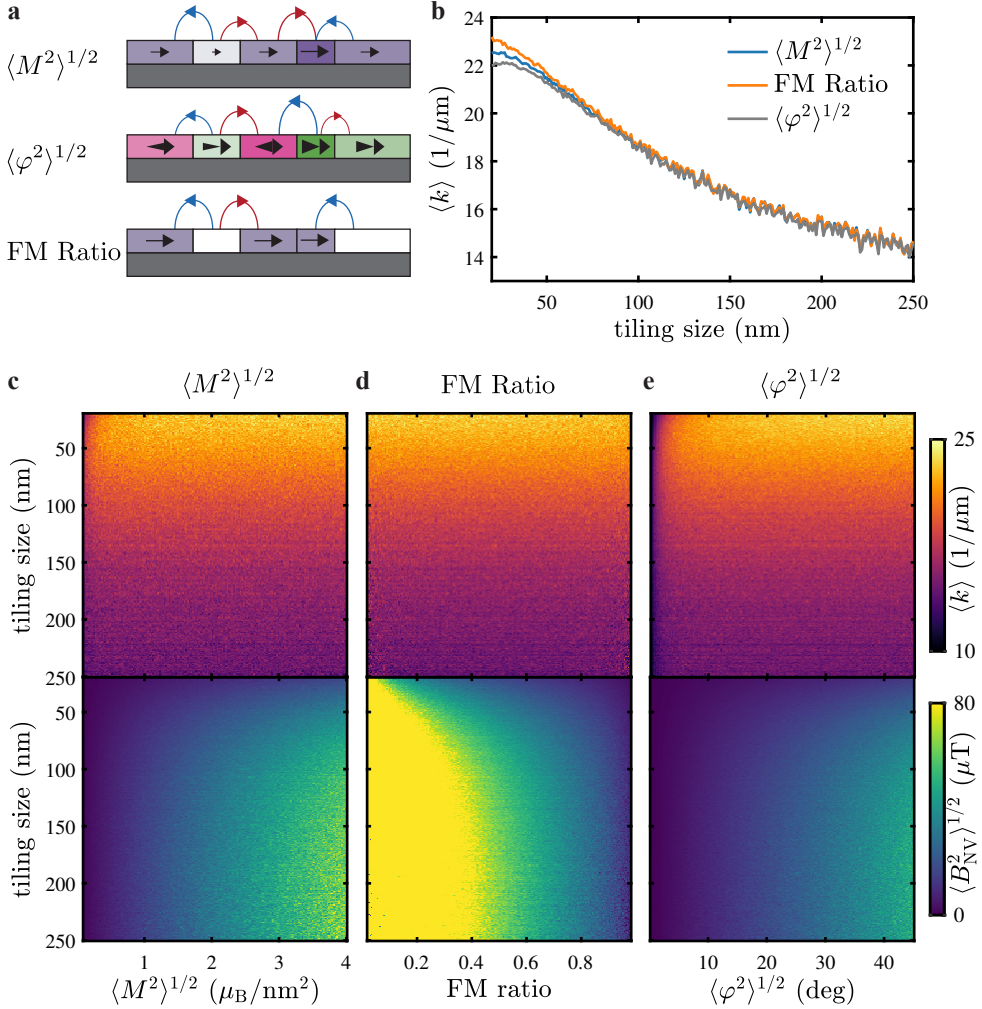
Figure A.3.: Simulation of Different Stray Field Patterns. **a** Schematic of different magnetic sources to produce a stochastic stray field pattern: A stray field arise when the magnetization either varies in strength, orientation, or changes from a non-magnetic to a ferromagnetic state. **b** Dependence of the first moment of the spatial frequencies $\langle k \rangle$ for the different magnetic models. The characteristic spatial frequency of a stochastic pattern is to a good approximation independent of the underlying nanoscale source. **c** Full parameter searches for a Gaussian distribution of the magnetization strength characterized by its variance $\langle M^2 \rangle^{1/2}$. **d** Full parameter searches for a Gaussian distribution of the magnetization orientation characterized by its variance $\langle \varphi^2 \rangle^{1/2}$. **e** Full parameter searches for a binomial distribution of a non-magnetic and ferromagnetic state characterized by its FM ratio. All maps in c, d, e have the mean magnetization $\langle M \rangle = 4\,\mu_{\mathrm{B}}/\mathrm{nm}^2$.

thus be used to distinguish between different nanoscale sources. For symmetry reasons, the first moment of the field distribution $\langle B_{NV} \rangle$ is zero (absence of magnetic monopoles, $\nabla \cdot \mathbf{B} = 0$). However, the second moment $\langle B_{NV}^2 \rangle^{1/2}$ is non-zero and indicates the distribution of the magnetic properties. For tiling sizes larger than the NV distance, $\langle B_{NV}^2 \rangle^{1/2}$ shows a linear dependence on tiling size and increases with increasing $\langle M^2 \rangle^{1/2}$ and $\langle \varphi^2 \rangle^{1/2}$ or decreasing FM ratios. For tiling sizes smaller than the NV distance, the NV becomes less sensitive to the dominant spatial frequencies and the dependence of $\langle B_{NV}^2 \rangle^{1/2}$ on tiling size is also affected by the spatial filter function defined by d_{NV}. In general, wider distributions are required to obtain a similar strength in the field distribution, but $\langle B_{NV}^2 \rangle^{1/2}$ still shows a clear monotonic dependence on the distribution of the magnetic properties in this range.

Consequently, the moments $\langle B_{NV}^2 \rangle^{1/2}$ and $\langle k \rangle$ can be used to optimize the simulation of each model to match the empirical data as closely as possible. $\langle k \rangle$ is a good approximation of the characteristic length scale and is therefore used to set the tiling size of the Voronoi tessellation. The model parameters $\langle M^2 \rangle^{1/2}$, $\langle \varphi^2 \rangle^{1/2}$ or the FM ratio are fixed at a given tiling size according to the second moment of the field distribution $\langle B_{NV}^2 \rangle^{1/2}$. This allows the observed moments of the field dependence of any stray field data to be related to a well-defined parameter set of one of the three nanoscale source models (see Fig. 3.3 for an example). If this parameter can be fixed by control experiments, different nanoscale sources can be distinguished as shown in Section 4.4. Thus, the stochastic analysis of the stray field pattern can provide valuable information about a physical system, although the spatial resolution of S-NVM is not sufficient to fully reconstruct the underlying magnetization pattern.

A.3. Data Tables

Table A.1.: Model Parameters for Single-Layer EuGe$_2$. Extracted parameters from fitting Eq. (3.3) and Eq. (4.2) to the measurements shown in Fig. 4.5. Uncertainties are estimated from the covariance matrix. $\langle T_c \rangle$ and $\langle T_c^2 \rangle^{1/2}$ are obtained by assuming a Gaussian distribution.

fit parameter		
a	0.277(25)	T^{β}
b	5.2(13)	T^{β}
β	0.250(27)	
γ	2.78(42)	
M_0	12.2(10)	μ_B/nm^2
M_{PM}	37.3(92)	μ_B/nm^2
$\langle T_c \rangle$	3.29(17)	K
$\langle T_c^2 \rangle^{1/2}$	0.84(37)	K

Table A.2.: Fit Results from the Line Cuts on MnPS$_3$. Fit results obtained by fitting the line cuts shown in Fig. 5.3 **e** to a magnetic edge (Eq. (3.5)), assuming the three magnetization orientations parallel to the NV axis, parallel to the out-of-plane direction, and parallel to the projection of the NV axis to the in-plane direction.

direction	M	d_{NV}	mean squared error
	(μ_B/nm^2)	(nm)	(μT)
$M \parallel$ NV	2.26(6)	48(2)	7.06
$M \parallel$ z	1.50(14)	51(6)	15.02
$M \parallel$ xy	2.17(4)	44(2)	5.37

Table A.3.: Comparison of the Statistical Properties of the Stray Field Images and the Simulated Magnetic Textures Using the Model for the Single-Layer EuGe$_2$.

data set	B_{ext}	$\langle B_{\text{NV}}^2\rangle_{\text{Data}}^{1/2}$	$\langle B_{\text{NV}}^2\rangle_{\text{Model}}^{1/2}$	$\langle k\rangle_{\text{Data}}$	$\langle k\rangle_{\text{Model}}$	grain size	tip
	(mT)	(μT)	(μT)	(1/μm)	(1/μm)	(nm)	
Fig. 4.8 a	1.5	14.1(14)	21.0(08)	19.8(6)	20.0(6)	78(12)	100
Fig. 4.8 b	5	23.2(14)	19.1(11)	19.8(6)	18.8(6)	78(12)	100
Fig. 4.11 c	1.5	15.9(12)	25.4(12)	17.5(7)	17.1(7)	133(20)	100
	2.5	20.3(16)	24.8(14)	16.4(6)	17.1(6)	133(20)	100
	5	23.5(19)	23.1(16)	17.2(7)	17.0(6)	133(20)	100
	10	25.7(20)	20.4(17)	17.4(7)	17.1(6)	133(20)	100
	15	23.8(19)	18.6(18)	17.3(7)	17.1(6)	133(20)	100
Fig. 4.11 d	5	11.8(09)	22.0(16)	17.0(7)	17.1(6)	144(24)	110
	15	14.0(11)	17.7(19)	16.6(7)	17.0(6)	144(24)	110
	50	15.1(12)	12.4(20)	17.0(6)	16.9(8)	144(24)	110
	150	15.1(12)	8.1(17)	16.2(6)	16.3(8)	144(24)	110
	200	14.2(11)	7.1(18)	16.8(7)	16.0(8)	144(24)	110
	250	13.9(18)	6.8(18)	17.1(7)	15.8(9)	144(24)	110

B. Bibliography

[1] European Commission, *The EU's Quantum Technologies Flagships* (Publications Office, LU) (2022).

[2] C. Becher, W. Gao, S. Kar, C. D. Marciniak, T. Monz, J. G. Bartholomew, P. Goldner, H. Loh, E. Marcellina, K. E. J. Goh, T. S. Koh, B. Weber, Z. Mu, J.-Y. Tsai, Q. Yan, T. Huber-Loyola, S. Höfling, S. Gyger, S. Steinhauer, and V. Zwiller, *2023 roadmap for materials for quantum technologies*, Materials for Quantum Technology **3**, 012501 (2023).

[3] K. Bongs, S. Bennett, and A. Lohmann, *Quantum sensors will start a revolution — if we deploy them right*, Nature **617**, 672 (2023).

[4] M. S. Safronova and D. Budker, *Quantum technologies and the elephants*, Quantum Science and Technology **6**, 040401 (2021).

[5] C. L. Degen, F. Reinhard, and P. Cappellaro, *Quantum sensing*, Review of Modern Physics **89**, 035002 (2017).

[6] P. Maletinsky, S. Hong, M. S. Grinolds, B. Hausmann, M. D. Lukin, R. L. Walsworth, M. Loncar, and A. Yacoby, *A robust scanning diamond sensor for nanoscale imaging with single nitrogen-vacancy centres*, Nature Nanotechnology **7**, 320 (2012).

[7] L. Rondin, J.-P. Tetienne, T. Hingant, J.-F. Roch, P. Maletinsky, and V. Jacques, *Magnetometry with nitrogen-vacancy defects in diamond*, Reports on Progress in Physics **77**, 056503 (2014).

[8] G. Balasubramanian, I. Y. Chan, R. Kolesov, M. Al-Hmoud, J. Tisler, C. Shin, C. Kim, A. Wojcik, P. R. Hemmer, A. Krueger, T. Hanke, A. Leitenstorfer, R. Bratschitsch, F. Jelezko, and J. Wrachtrup, *Nanoscale imaging magnetometry with diamond spins under ambient conditions*, Nature **455**, 648 (2008).

[9] L. Rondin, J.-P. Tetienne, P. Spinicelli, C. Dal Savio, K. Karrai, G. Dantelle, A. Thiaville, S. Rohart, J.-F. Roch, and V. Jacques, *Nanoscale magnetic field mapping with a single spin scanning probe magnetometer*, Applied Physics Letters **100**, 153118 (2012).

[10] K. Chang, A. Eichler, J. Rhensius, L. Lorenzelli, and C. L. Degen, *Nanoscale Imaging of Current Density with a Single-Spin Magnetometer*, Nano Letters **17**, 2367 (2017).

[11] P. Appel, M. Ganzhorn, E. Neu, and P. Maletinsky, *Nanoscale microwave imaging with a single electron spin in diamond*, New Journal of Physics **17**, 112001 (2015).

[12] F. Casola, T. van der Sar, and A. Yacoby, *Probing condensed matter physics with magnetometry based on nitrogen-vacancy centres in diamond*, Nature Reviews Materials **3**, 17088 (2018).

[13] D. Rohner, L. Thiel, B. Müller, M. Kasperczyk, R. Kleiner, D. Koelle, and P. Maletinsky, *Real-Space Probing of the Local Magnetic Response of Thin-Film Superconductors Using Single Spin Magnetometry*, Sensors **18**, 3790 (2018).

[14] L. Thiel, D. Rohner, M. Ganzhorn, P. Appel, E. Neu, B. Müller, R. Kleiner, D. Koelle, and P. Maletinsky, *Quantitative nanoscale vortex imaging using a cryogenic quantum magnetometer*, Nature Nanotechnology **11**, 677 (2016).

[15] I. Gross, W. Akhtar, V. Garcia, L. J. Martínez, S. Chouaieb, K. Garcia, C. Carrétéro, A. Barthélémy, P. Appel, P. Maletinsky, J.-V. Kim, J. Y. Chauleau, N. Jaouen, M. Viret, M. Bibes, S. Fusil, and V. Jacques, *Real-space imaging of non-collinear antiferromagnetic order with a single-spin magnetometer*, Nature **549**, 252 (2017).

[16] N. Hedrich, K. Wagner, O. V. Pylypovskyi, B. J. Shields, T. Kosub, D. D. Sheka, D. Makarov, and P. Maletinsky, *Nanoscale mechanics of antiferromagnetic domain walls*, Nature Physics **17**, 574 (2021).

[17] A. Jenkins, S. Baumann, H. Zhou, S. A. Meynell, Y. Daipeng, K. Watanabe, T. Taniguchi, A. Lucas, A. F. Young, and A. C. Bleszynski Jayich, *Imaging the Breakdown of Ohmic Transport in Graphene*, Physical Review Letters **129**, 087701 (2022).

[18] M. Palm, W. Huxter, P. Welter, S. Ernst, P. Scheidegger, S. Diesch, K. Chang, P. Rickhaus, T. Taniguchi, K. Watanabe, K. Ensslin, and C. Degen, *Imaging of Submicroampere Currents in Bilayer Graphene Using a Scanning Diamond Magnetometer*, Physical Review Applied **17**, 054008 (2022).

[19] I. Bertelli, B. G. Simon, T. Yu, J. Aarts, G. E. W. Bauer, Y. M. Blanter, and T. van der Sar, *Imaging Spin-Wave Damping Underneath Metals Using Electron Spins in Diamond*, Advanced Quantum Technologies **4**, 2100094 (2021).

[20] T. X. Zhou, J. J. Carmiggelt, L. M. Gächter, I. Esterlis, D. Sels, R. J. Stöhr, C. Du, D. Fernandez, J. F. Rodriguez-Nieva, and F. Büttner, *A magnon scattering platform*, Proceedings of the National Academy of Sciences **118**, e2019473118 (2021).

[21] B. Huang, G. Clark, E. Navarro-Moratalla, D. R. Klein, R. Cheng, K. L. Seyler, D. Zhong, E. Schmidgall, M. A. McGuire, D. H. Cobden, W. Yao, D. Xiao, P. Jarillo-Herrero, and X. Xu, *Layer-dependent ferromagnetism in a van der Waals crystal down to the monolayer limit*, Nature **546**, 270 (2017).

[22] C. Gong, L. Li, Z. Li, H. Ji, A. Stern, Y. Xia, T. Cao, W. Bao, C. Wang, Y. Wang, Z. Q. Qiu, R. J. Cava, S. G. Louie, J. Xia, and X. Zhang, *Discovery of intrinsic ferromagnetism in two-dimensional van der Waals crystals*, Nature **546**, 265 (2017).

[23] M. Gibertini, M. Koperski, A. F. Morpurgo, and K. S. Novoselov, *Magnetic 2D materials and heterostructures*, Nature Nanotechnology **14**, 408 (2019).

[24] E. Marchiori, L. Ceccarelli, N. Rossi, L. Lorenzelli, C. L. Degen, and M. Poggio, *Nanoscale magnetic field imaging for 2D materials*, Nature Reviews Physics **4**, 49 (2021).

[25] A. Laraoui and K. Ambal, *Opportunities for nitrogen-vacancy-assisted magnetometry to study magnetism in 2D van der Waals magnets*, Applied Physics Letters **121**, 060502 (2022).

[26] L. Thiel, Z. Wang, M. A. Tschudin, D. Rohner, I. Gutiérrez-Lezama, N. Ubrig, M. Gibertini, E. Giannini, A. F. Morpurgo, and P. Maletinsky, *Probing magnetism in 2D materials at the nanoscale with single-spin microscopy*, Science **364**, 973 (2019).

[27] T. Song, Q.-C. Sun, E. Anderson, C. Wang, J. Qian, T. Taniguchi, K. Watanabe, M. A. McGuire, R. Stöhr, D. Xiao, T. Cao, J. Wrachtrup, and X. Xu, *Direct visualization of magnetic domains and moiré magnetism in twisted 2D magnets*, Science **374**, 1140 (2021).

[28] M. W. Doherty, N. B. Manson, P. Delaney, F. Jelezko, J. Wrachtrup, and L. C. Hollenberg, *The nitrogen-vacancy colour centre in diamond*, Physics Reports **528**, 1 (2013).

[29] P. Appel, E. Neu, M. Ganzhorn, A. Barfuss, M. Batzer, M. Gratz, A. Tschöpe, and P. Maletinsky, *Fabrication of all diamond scanning probes for nanoscale magnetometry*, Review of Scientific Instruments **87**, 063703 (2016).

[30] P. J. Scheidegger, S. Diesch, M. L. Palm, and C. L. Degen, *Scanning nitrogen-vacancy magnetometry down to 350 mK*, Applied Physics Letters **120**, 224001 (2022).

[31] G.-Q. Liu, X. Feng, N. Wang, Q. Li, and R.-B. Liu, *Coherent quantum control of nitrogen-vacancy center spins near 1000 kelvin*, Nature Communications **10**, 1344 (2019).

[32] J.-P. Tetienne, T. Hingant, L. Martínez, S. Rohart, A. Thiaville, L. H. Diez, K. Garcia, J.-P. Adam, J.-V. Kim, J.-F. Roch, I. Miron, G. Gaudin, L. Vila, B. Ocker, D. Ravelosona, and V. Jacques, *The nature of domain walls in ultrathin ferromagnets revealed by scanning nanomagnetometry*, Nature Communications **6**, 6733 (2015).

[33] Y. Dovzhenko, F. Casola, S. Schlotter, T. X. Zhou, F. Büttner, R. L. Walsworth, G. S. D. Beach, and A. Yacoby, *Magnetostatic twists in room-temperature skyrmions explored by nitrogen-vacancy center spin texture reconstruction*, Nature Communications **9**, 2712 (2018).

[34] S. Pezzagna, B. Naydenov, F. Jelezko, J. Wrachtrup, and J. Meijer, *Creation efficiency of nitrogen-vacancy centres in diamond*, New Journal of Physics **12**, 065017 (2010).

[35] T. Yamamoto, T. Umeda, K. Watanabe, S. Onoda, M. L. Markham, D. J. Twitchen, B. Naydenov, L. P. McGuinness, T. Teraji, S. Koizumi, F. Dolde, H. Fedder, J. Honert, J. Wrachtrup, T. Ohshima, F. Jelezko, and J. Isoya, *Extending spin coherence times of diamond qubits by high-temperature annealing*, Physical Review B **88**, 075206 (2013).

[36] K. C. Wong, S. L. Ng, K. O. Ho, Y. Shen, J. Wu, K. T. Lai, M. Y. Leung, W. K. Leung, D. B. R. Dasari, A. Denisenko, J. Wrachtrup, and S. Yang, *Microscopic Study of Optically Stable Coherent Color Centers in Diamond Generated by High-Temperature Annealing*, Physical Review Applied **18**, 024044 (2022).

[37] C. Osterkamp, J. Lang, J. Scharpf, C. Müller, L. P. McGuinness, T. Diemant, R. J. Behm, B. Naydenov, and F. Jelezko, *Stabilizing shallow color centers in diamond created by nitrogen delta-doping using SF6 plasma treatment*, Applied Physics Letters **106**, 113109 (2015).

[38] C. A. McLellan, B. A. Myers, S. Kraemer, K. Ohno, D. D. Awschalom, and A. C. Bleszynski Jayich, *Patterned Formation of Highly Coherent Nitrogen-Vacancy Centers Using a Focused Electron Irradiation Technique*, Nano Letters **16**, 2450 (2016).

[39] Y.-C. Chen, B. Griffiths, L. Weng, S. S. Nicley, S. N. Ishmael, Y. Lekhai, S. Johnson, C. J. Stephen, B. L. Green, G. W. Morley, M. E. Newton, M. J. Booth, P. S. Salter, and J. M. Smith, *Laser writing of individual nitrogen-vacancy defects in diamond with near-unity yield*, Optica **6**, 662 (2019).

[40] V. Yurgens, J. A. Zuber, S. Flågan, M. De Luca, B. J. Shields, I. Zardo, P. Maletinsky, R. J. Warburton, and T. Jakubczyk, *Low charge-noise nitrogen-vacancy centers in diamond created using laser writing with a solid-immersion lens*, ACS Photonics **8**, 1726 (2021).

[41] S. D. Subedi, V. V. Fedorov, J. Peppers, D. V. Martyshkin, S. B. Mirov, L. Shao, and M. Loncar, *Laser spectroscopic characterization of negatively charged nitrogen-vacancy centers in diamond*, Optical Materials Express **9**, 2076 (2019).

[42] N. Aslam, G. Waldherr, P. Neumann, F. Jelezko, and J. Wrachtrup, *Photo-induced ionization dynamics of the nitrogen vacancy defect in diamond investigated by single-shot charge state detection*, New Journal of Physics **15**, 013064 (2013).

[43] R. Giri, R. H. Jensen, D. Khurana, J. Bocquel, I. P. Radko, J. Lang, C. Osterkamp, F. Jelezko, K. Berg-Sorensen, U. L. Andersen, and A. Huck, *Charge stability and charge-state-based spin readout of shallow nitrogen-vacancy centers in diamond*, ACS Applied Electronic Materials **5**, 6603 (2023).

[44] J.-C. Jaskula, B. Shields, E. Bauch, M. Lukin, A. Trifonov, and R. Walsworth, *Improved Quantum Sensing with a Single Solid-State Spin via Spin-to-Charge Conversion*, Physical Review Applied **11**, 064003 (2019).

[45] Á. Gali, Ab Initio *theory of the nitrogen-vacancy center in diamond*, Nanophotonics **8**, 1907 (2019).

[46] J. R. Maze, A. Gali, E. Togan, Y. Chu, A. Trifonov, E. Kaxiras, and M. D. Lukin, *Properties of nitrogen-vacancy centers in diamond: The group theoretic approach*, New Journal of Physics **13**, 025025 (2011).

[47] J. R. Rabeau, P. Reichart, G. Tamanyan, D. N. Jamieson, S. Prawer, F. Jelezko, T. Gaebel, I. Popa, M. Domhan, and J. Wrachtrup, *Implantation of labelled single nitrogen vacancy centers in diamond using N15*, Applied Physics Letters **88**, 023113 (2006).

[48] M. W. Doherty, F. Dolde, H. Fedder, F. Jelezko, J. Wrachtrup, N. B. Manson, and L. C. L. Hollenberg, *Theory of the ground-state spin of the NV - center in diamond*, Physical Review B **85**, 205203 (2012).

[49] L. J. Rogers, R. L. McMurtrie, M. J. Sellars, and N. B. Manson, *Time-averaging within the excited state of the nitrogen-vacancy centre in diamond*, New Journal of Physics **11**, 063007 (2009).

[50] J. Happacher, J. Bocquel, H. T. Dinani, M. A. Tschudin, P. Reiser, D. A. Broadway, J. R. Maze, and P. Maletinsky, *Temperature-Dependent Photophysics of Single NV Centers in Diamond*, Physical Review Letters **131**, 086904 (2023).

[51] L. Robledo, H. Bernien, T. V. D. Sar, and R. Hanson, *Spin dynamics in the optical cycle of single nitrogen-vacancy centres in diamond*, New Journal of Physics **13**, 025013 (2011).

[52] F. Dolde, H. Fedder, M. W. Doherty, T. Nöbauer, F. Rempp, G. Balasubramanian, T. Wolf, F. Reinhard, L. C. L. Hollenberg, F. Jelezko, and J. Wrachtrup, *Electric-field sensing using single diamond spins*, Nature Physics **7**, 459 (2011).

[53] M. C. Cambria, A. Norambuena, H. T. Dinani, G. Thiering, A. Gardill, I. Kemeny, Y. Li, V. Lordi, Á. Gali, J. R. Maze, and S. Kolkowitz, *Temperature-Dependent Spin-Lattice Relaxation of the Nitrogen-Vacancy Spin Triplet in Diamond*, Physical Review Letters **130**, 256903 (2023).

[54] M. C. Cambria, G. Thiering, A. Norambuena, H. T. Dinani, A. Gardill, I. Kemeny, V. Lordi, A. Gali, J. R. Maze, and S. Kolkowitz, *Physically motivated analytical expression for the temperature dependence of the zero-field splitting of the nitrogen-vacancy center in diamond*, Physical Review B **108**, L180102 (2023).

[55] V. M. Acosta, E. Bauch, M. P. Ledbetter, A. Waxman, L.-S. Bouchard, and D. Budker, *Temperature Dependence of the Nitrogen-Vacancy Magnetic Resonance in Diamond*, Physical Review Letters **104**, 070801 (2010).

[56] M. H. Abobeih, J. Cramer, M. A. Bakker, N. Kalb, M. Markham, D. J. Twitchen, and T. H. Taminiau, *One-second coherence for a single electron spin coupled to a multi-qubit nuclear-spin environment*, Nature Communications **9**, 2552 (2018).

[57] E. D. Herbschleb, H. Kato, Y. Maruyama, T. Danjo, T. Makino, S. Yamasaki, I. Ohki, K. Hayashi, H. Morishita, M. Fujiwara, and N. Mizuochi, *Ultra-long coherence times amongst room-temperature solid-state spins*, Nature Communications **10**, 3766 (2019).

[58] A. Dréau, M. Lesik, L. Rondin, P. Spinicelli, O. Arcizet, J.-F. Roch, and V. Jacques, *Avoiding power broadening in optically detected magnetic resonance of single NV defects for enhanced dc magnetic field sensitivity*, Physical Review B **84** (2011).

[59] J. F. Barry, J. M. Schloss, E. Bauch, M. J. Turner, C. A. Hart, L. M. Pham, and R. L. Walsworth, *Sensitivity optimization for NV-diamond magnetometry*, Reviews of Modern Physics **92**, 015004 (2020).

[60] H. A. R. El-Ella, S. Ahmadi, A. M. Wojciechowski, A. Huck, and U. L. Andersen, *Optimised frequency modulation for continuous-wave optical magnetic resonance sensing using nitrogen-vacancy ensembles*, Optics Express **25**, 14809 (2017).

[61] J. F. Barry, M. J. Turner, J. M. Schloss, D. R. Glenn, Y. Song, M. D. Lukin, H. Park, and R. L. Walsworth, *Optical magnetic detection of single-neuron action potentials using quantum defects in diamond*, Proceedings of the National Academy of Sciences **113**, 14133 (2016).

[62] E. A. Lima and B. P. Weiss, *Obtaining vector magnetic field maps from single-component measurements of geological samples*, Journal of Geophysical Research **114**, B06102 (2009).

[63] T. Zhu, J. Rhensius, K. Herb, V. Damle, G. Puebla-Hellmann, C. L. Degen, and E. Janitz, *Multicone Diamond Waveguides for Nanoscale Quantum Sensing*, Nano Letters **23**, 10110 (2023).

[64] N. Hedrich, D. Rohner, M. Batzer, P. Maletinsky, and B. J. Shields, *Parabolic Diamond Scanning Probes for Single-Spin Magnetic Field Imaging*, Physical Review Applied **14**, 064007 (2020).

[65] R. S. Schoenfeld and W. Harneit, *Real Time Magnetic Field Sensing and Imaging Using a Single Spin in Diamond*, Physical Review Letters **106**, 030802 (2011).

[66] V. Yurgens, A. Corazza, J. A. Zuber, M. Gruet, M. Kasperczyk, B. J. Shields, R. J. Warburton, Y. Fontana, and P. Maletinsky, *Spectrally stable nitrogen-vacancy centers in diamond formed by carbon implantation into thin microstructures*, Applied Physics Letters **121**, 234001 (2022).

[67] S. Sangtawesin, B. L. Dwyer, S. Srinivasan, J. J. Allred, L. V. H. Rodgers, K. De Greve, A. Stacey, N. Dontschuk, K. M. O'Donnell, D. Hu, D. A. Evans, C. Jaye, D. A. Fischer, M. L. Markham, D. J. Twitchen, H. Park, M. D. Lukin, and N. P. de Leon, *Origins of Diamond Surface Noise Probed by Correlating Single-Spin Measurements with Surface Spectroscopy*, Physical Review X **9**, 031052 (2019).

[68] J. M. Abendroth, K. Herb, E. Janitz, T. Zhu, L. A. Völker, and C. L. Degen, *Single-Nitrogen–Vacancy NMR of Amine-Functionalized Diamond Surfaces*, Nano Letters **22**, 7294 (2022).

[69] J. Geng, T. Shalomayeva, M. Gryzlova, A. Mukherjee, S. Santonocito, D. Dzhavadzade, D. B. R. Dasari, H. Kato, R. Stöhr, A. Denisenko, N. Mizuochi, and J. Wrachtrup, *Dopant-assisted stabilization of negatively charged single nitrogen-vacancy centers in phosphorus-doped diamond at low temperatures*, npj Quantum Information **9**, 110 (2023).

[70] Y. Li, F. A. Gerritsma, S. Kurdi, N. Codreanu, S. Gröblacher, R. Hanson, R. Norte, and T. Van Der Sar, *A Fiber-Coupled Scanning Magnetometer with Nitrogen-Vacancy Spins in a Diamond Nanobeam*, ACS Photonics **10**, 1859 (2023).

[71] F. Alghannam and P. Hemmer, *Engineering of Shallow Layers of Nitrogen Vacancy Colour Centres in Diamond Using Plasma Immersion Ion Implantation*, Scientific Reports **9**, 5870 (2019).

[72] M. Batzer, B. Shields, E. Neu, C. Widmann, C. Giese, C. Nebel, and P. Maletinsky, *Single crystal diamond pyramids for applications in nanoscale quantum sensing*, Optical Materials Express **10**, 492 (2020).

[73] W. S. Huxter, M. L. Palm, M. L. Davis, P. Welter, C.-H. Lambert, M. Trassin, and C. L. Degen, *Scanning gradiometry with a single spin quantum magnetometer*, Nature Communications **13**, 3761 (2022).

[74] E. Turner, S.-H. Wu, X. Li, and H. Wang, *Spin-based continuous Bayesian magnetic-field estimations aided by feedback control*, Physical Review A **106**, 052603 (2022).

[75] I. Zohar, B. Haylock, Y. Romach, M. J. Arshad, N. Halay, N. Drucker, R. Stöhr, A. Denisenko, Y. Cohen, C. Bonato, and A. Finkler, *Real-time frequency estimation of a qubit without single-shot-readout*, Quantum Science and Technology **8**, 035017 (2023).

[76] K. S. Novoselov, A. K. Geim, S. V. Morozov, D. Jiang, Y. Zhang, S. V. Dubonos, I. V. Grigorieva, and A. A. Firsov, *Electric Field Effect in Atomically Thin Carbon Films*, Science **306**, 666 (2004).

[77] A. K. Geim and I. V. Grigorieva, *Van der Waals heterostructures*, Nature **499**, 419 (2013).

[78] E. C. Ahn, *2D materials for spintronic devices*, npj 2D Materials and Applications **4**, 17 (2020).

[79] J. M. D. Coey, *Magnetism and Magnetic Materials*, (Cambridge University Press, Cambridge) (2010).

[80] Q. H. Wang, A. Bedoya-Pinto, M. Blei, A. H. Dismukes, A. Hamo, S. Jenkins, M. Koperski, Y. Liu, Q.-C. Sun, E. J. Telford, H. H. Kim, M. Augustin,

U. Vool, J.-X. Yin, L. H. Li, A. Falin, C. R. Dean, F. Casanova, R. F. L. Evans, M. Chshiev, A. Mishchenko, C. Petrovic, R. He, L. Zhao, A. W. Tsen, B. D. Gerardot, M. Brotons-Gisbert, Z. Guguchia, X. Roy, S. Tongay, Z. Wang, M. Z. Hasan, J. Wrachtrup, A. Yacoby, A. Fert, S. Parkin, K. S. Novoselov, P. Dai, L. Balicas, and E. J. G. Santos, *The magnetic genome of two-dimensional van der Waals materials*, ACS Nano **16**, 6960 (2022).

[81] M. E. Fisher, *The theory of equilibrium critical phenomena*, Reports on Progress in Physics **30**, 615 (1967).

[82] A. Arrott and J. E. Noakes, *Approximate Equation of State For Nickel Near its Critical Temperature*, Physical Review Letters **19**, 786 (1967).

[83] H. E. Stanley, *Scaling, universality, and renormalization: Three pillars of modern critical phenomena*, Reviews of Modern Physics **71**, S358 (1999).

[84] N. D. Mermin and H. Wagner, *Absence of Ferromagnetism or Antiferromagnetism in One- or Two-Dimensional Isotropic Heisenberg Models*, Physical Review Letters **17**, 1133 (1966).

[85] P. C. Hohenberg, *Existence of Long-Range Order in One and Two Dimensions*, Physical Review **158**, 383 (1967).

[86] C. Gong and X. Zhang, *Two-dimensional magnetic crystals and emergent heterostructure devices*, Science **363**, eaav4450 (2019).

[87] E. J. Telford, A. H. Dismukes, K. Lee, M. Cheng, A. Wieteska, A. K. Bartholomew, Y.-S. Chen, X. Xu, A. N. Pasupathy, X. Zhu, C. R. Dean, and X. Roy, *Layered Antiferromagnetism Induces Large Negative Magnetoresistance in the van der Waals Semiconductor CrSBr*, Advanced Materials **32**, 2003240 (2020).

[88] K. Lee, A. H. Dismukes, E. J. Telford, R. A. Wiscons, J. Wang, X. Xu, C. Nuckolls, C. R. Dean, X. Roy, and X. Zhu, *Magnetic Order and Symmetry in the 2D Semiconductor CrSBr*, Nano Letters **21**, 3511 (2021).

[89] S. Jenkins, L. Rózsa, U. Atxitia, R. F. L. Evans, K. S. Novoselov, and E. J. G. Santos, *Breaking through the Mermin-Wagner limit in 2D van der Waals magnets*, Nature Communications **13**, 6917 (2022).

[90] R. Zhang and R. F. Willis, *Thickness-Dependent Curie Temperatures of Ultrathin Magnetic Films: Effect of the Range of Spin-Spin Interactions*, Physical Review Letters **86**, 2665 (2001).

[91] K. S. Burch, D. Mandrus, and J.-G. Park, *Magnetism in two-dimensional van der Waals materials*, Nature **563**, 47 (2018).

[92] T. Song, Z. Fei, M. Yankowitz, Z. Lin, Q. Jiang, K. Hwangbo, Q. Zhang, B. Sun, T. Taniguchi, K. Watanabe, M. A. McGuire, D. Graf, T. Cao, J.-H. Chu, D. H. Cobden, C. R. Dean, D. Xiao, and X. Xu, *Switching 2D magnetic states via pressure tuning of layer stacking*, Nature Materials **18**, 1298 (2019).

[93] E. J. Telford, D. G. Chica, M. E. Ziebel, K. Xie, N. S. Manganaro, C.-Y. Huang, J. Cox, A. H. Dismukes, X. Zhu, J. P. S. Walsh, T. Cao, C. R. Dean, and X. Roy, *Designing Magnetic Properties in CrSBr through Hydrostatic Pressure and Ligand Substitution*, Advanced Physics Research **2**, 2300036 (2023).

[94] S. Jiang, J. Shan, and K. F. Mak, *Electric-field switching of two-dimensional van der Waals magnets*, Nature Materials **17**, 406 (2018).

[95] S. Jiang, L. Li, Z. Wang, K. F. Mak, and J. Shan, *Controlling magnetism in 2D CrI3 by electrostatic doping*, Nature Nanotechnology **13**, 549 (2018).

[96] B. Huang, G. Clark, D. R. Klein, D. MacNeill, E. Navarro-Moratalla, K. L. Seyler, N. Wilson, M. A. McGuire, D. H. Cobden, D. Xiao, W. Yao, P. Jarillo-Herrero, and X. Xu, *Electrical control of 2D magnetism in bilayer CrI3*, Nature Nanotechnology **13**, 544 (2018).

[97] P. Jiang, C. Wang, D. Chen, Z. Zhong, Z. Yuan, Z.-Y. Lu, and W. Ji, *Stacking tunable interlayer magnetism in bilayer* cri$_3$, Physical Review B **99**, 144401 (2019).

[98] W. Chen, Z. Sun, Z. Wang, L. Gu, X. Xu, S. Wu, and C. Gao, *Direct observation of van der Waals stacking–dependent interlayer magnetism*, Science **366**, 983 (2019).

[99] C. Boix-Constant, S. Jenkins, R. Rama-Eiroa, E. J. G. Santos, S. Mañas-Valero, and E. Coronado, *Multistep magnetization switching in orthogonally twisted ferromagnetic monolayers*, Nature Materials (2023).

[100] L. Ciorciaro, M. Kroner, K. Watanabe, T. Taniguchi, and A. Imamoglu, *Observation of Magnetic Proximity Effect Using Resonant Optical Spectroscopy of an Electrically Tunable MoSe 2 / CrBr 3 Heterostructure*, Physical Review Letters **124**, 197401 (2020).

[101] H. Dai, H. Cheng, M. Cai, Q. Hao, Y. Xing, H. Chen, X. Chen, X. Wang, and J.-B. Han, *Enhancement of the Coercive Field and Exchange Bias Effect in Fe3GeTe2/MnPX2 (X = S and Se) van der Waals Heterostructures*, ACS Applied Materials & Interfaces **13**, 24314 (2021).

[102] M. A. Tschudin, D. A. Broadway, P. Reiser, C. Schrader, E. J. Telford, B. Gross, J. Cox, A. E. E. Dubois, D. G. Chica, R. Rama-Eiroa, E. J. G. Santos, M. Poggio, M. E. Ziebel, C. R. Dean, X. Roy, and P. Maletinsky, *Nanoscale magnetism and magnetic phase transitions in atomically thin CrSBr*, arXiv:2312.09279 (2023).

[103] Q.-C. Sun, T. Song, E. Anderson, A. Brunner, J. Förster, T. Shalomayeva, T. Taniguchi, K. Watanabe, J. Gräfe, R. Stöhr, X. Xu, and J. Wrachtrup, *Magnetic domains and domain wall pinning in atomically thin CrBr3 revealed by nanoscale imaging*, Nature Communications **12**, 1989 (2021).

[104] D. A. Broadway, S. C. Scholten, C. Tan, N. Dontschuk, S. E. Lillie, B. C. Johnson, G. Zheng, Z. Wang, A. R. Oganov, S. Tian, C. Li, H. Lei, L. Wang, L. C. L.

Hollenberg, and J.-P. Tetienne, *Imaging Domain Reversal in an Ultrathin Van der Waals Ferromagnet*, Advanced Materials **32**, 2003314 (2020).

[105] M.-G. Han, J. A. Garlow, Y. Liu, H. Zhang, J. Li, D. DiMarzio, M. W. Knight, C. Petrovic, D. Jariwala, and Y. Zhu, *Topological Magnetic-Spin Textures in Two-Dimensional van der Waals Cr2Ge2Te6*, Nano Letters **19**, 7859 (2019).

[106] Y. Wu, S. Zhang, J. Zhang, W. Wang, Y. L. Zhu, J. Hu, G. Yin, K. Wong, C. Fang, C. Wan, X. Han, Q. Shao, T. Taniguchi, K. Watanabe, J. Zang, Z. Mao, X. Zhang, and K. L. Wang, *Néel-type skyrmion in WTe2/Fe3GeTe2 van der Waals heterostructure*, Nature Communications **11**, 3860 (2020).

[107] Z. Hennighausen and S. Kar, *Twistronics: A turning point in 2D quantum materials*, Electronic Structure **3**, 014004 (2021).

[108] J. F. Sierra, J. Fabian, R. K. Kawakami, S. Roche, and S. O. Valenzuela, *Van der Waals heterostructures for spintronics and opto-spintronics*, Nature Nanotechnology **16**, 856 (2021).

[109] T. Song, X. Cai, M. W.-Y. Tu, X. Zhang, B. Huang, N. P. Wilson, K. L. Seyler, L. Zhu, T. Taniguchi, K. Watanabe, M. A. McGuire, D. H. Cobden, D. Xiao, W. Yao, and X. Xu, *Giant tunneling magnetoresistance in spin-filter van der Waals heterostructures*, Science **360**, 1214 (2018).

[110] X. Cai, T. Song, N. P. Wilson, G. Clark, M. He, X. Zhang, T. Taniguchi, K. Watanabe, W. Yao, D. Xiao, M. A. McGuire, D. H. Cobden, and X. Xu, *Atomically Thin CrCl3 : An In-Plane Layered Antiferromagnetic Insulator*, Nano Letters **19**, 3993 (2019).

[111] S. Jiang, L. Li, Z. Wang, J. Shan, and K. F. Mak, *Spin tunnel field-effect transistors based on two-dimensional van der Waals heterostructures*, Nature Electronics **2**, 159 (2019).

[112] T. M. J. Cham, R. J. Dorrian, X. S. Zhang, A. H. Dismukes, D. G. Chica, A. F. May, X. Roy, D. A. Muller, D. C. Ralph, and Y. K. Luo, *Exchange bias between van der waals materials: Tilted magnetic states and field-free spin–orbit-torque switching*, Advanced Materials **36**, 2305739 (2024).

[113] Y. Liu, Y. Huang, and X. Duan, *Van der Waals integration before and beyond two-dimensional materials*, Nature **567**, 323 (2019).

[114] S. Jiang, J. Shan, and K. F. Mak, *Electric-field switching of two-dimensional van der Waals magnets*, Nature Materials **17**, 406 (2018).

[115] X.-X. Zhang, L. Li, D. Weber, J. Goldberger, K. F. Mak, and J. Shan, *Gate-tunable spin waves in antiferromagnetic atomic bilayers*, Nature Materials **19**, 838 (2020).

[116] A. Bedoya-Pinto, J.-R. Ji, A. K. Pandeya, P. Gargiani, M. Valvidares, P. Sessi, J. M. Taylor, F. Radu, K. Chang, and S. S. P. Parkin, *Intrinsic 2D-XY ferromagnetism in a van der Waals monolayer*, Science **374**, 616 (2021).

[117] D. V. Averyanov, I. S. Sokolov, M. S. Platunov, F. Wilhelm, A. Rogalev, P. Gargiani, M. Valvidares, N. Jaouen, O. E. Parfenov, A. N. Taldenkov, I. A. Karateev, A. M. Tokmachev, and V. G. Storchak, *Competing magnetic states in silicene and germanene 2D ferromagnets*, Nano Research **13**, 3396 (2020).

[118] J. Cenker, B. Huang, N. Suri, P. Thijssen, A. Miller, T. Song, T. Taniguchi, K. Watanabe, M. A. McGuire, D. Xiao, and X. Xu, *Direct observation of two-dimensional magnons in atomically thin CrI3*, Nature Physics **17**, 20 (2021).

[119] T. S. Ghiasi, M. Borst, S. Kurdi, B. G. Simon, I. Bertelli, C. Boix-Constant, S. Mañas-Valero, H. S. J. van der Zant, and T. van der Sar, *Nitrogen-vacancy magnetometry of CrSBr by diamond membrane transfer*, npj 2D Materials and Applications **7**, 62 (2023).

[120] C. L. Tschirhart, M. Serlin, H. Polshyn, A. Shragai, Z. Xia, J. Zhu, Y. Zhang, K. Watanabe, T. Taniguchi, M. E. Huber, and A. F. Young, *Imaging orbital ferromagnetism in a moiré Chern insulator*, Science **372**, 1323 (2021).

[121] W. Ge, J. Kim, Y.-T. Chan, D. Vanderbilt, J. Yan, and W. Wu, *Direct Visualization of Surface Spin-Flip Transition in MnBi4/Te7*, Physical Review Letters **129**, 107204 (2022).

[122] Shaofen Tan, Yu Pei Ma, I. M. Thomas, and J. P. Wikswo, *Reconstruction of two-dimensional magnetization and susceptibility distributions from the magnetic field of soft magnetic materials*, IEEE Transactions on Magnetics **32**, 230 (1996).

[123] T. van der Sar, F. Casola, R. Walsworth, and A. Yacoby, *Nanometre-scale probing of spin waves using single electron spins*, Nature Communications **6**, 7886 (2015).

[124] D. Broadway, S. Lillie, S. Scholten, D. Rohner, N. Dontschuk, P. Maletinsky, J.-P. Tetienne, and L. Hollenberg, *Improved Current Density and Magnetization Reconstruction Through Vector Magnetic Field Measurements*, Physical Review Applied **14**, 024076 (2020).

[125] A. Dubois, D. Broadway, A. Stark, M. Tschudin, A. Healey, S. Huber, J.-P. Tetienne, E. Greplova, and P. Maletinsky, *Untrained Physically Informed Neural Network for Image Reconstruction of Magnetic Field Sources*, Physical Review Applied **18**, 064076 (2022).

[126] J. Happacher, D. A. Broadway, J. Bocquel, P. Reiser, A. Jimenéz, M. A. Tschudin, L. Thiel, D. Rohner, M. l. G. Puigibert, B. Shields, J. R. Maze, V. Jacques, and P. Maletinsky, *Low-Temperature Photophysics of Single Nitrogen-Vacancy Centers in Diamond*, Physical Review Letters **128**, 177401 (2022).

[127] S. Ernst, P. J. Scheidegger, S. Diesch, L. Lorenzelli, and C. L. Degen, *Temperature Dependence of Photoluminescence Intensity and Spin Contrast in Nitrogen-Vacancy Centers*, Physical Review Letters **131**, 086903 (2023).

[128] S. Ernst, P. J. Scheidegger, S. Diesch, and C. L. Degen, *Modeling temperature-dependent population dynamics in the excited state of the nitrogen-vacancy center in diamond*, Physical Review B **108**, 085203 (2023).

[129] D. F. Wise, *Could NV Centres in Diamonb Be Used to Measure Donor Spins in Silicon*, Ph.D. thesis, University College London (2021).

[130] D. Rohner, *Towards Single Spin Magnetometry at mK Temperatures*, Ph.D. thesis, Basel (2020).

[131] S. Parthasarathy, M. Joos, L. B. Hughes, S. A. Meynell, T. A. Morrison, J. D. Risner-Jamtgaard, D. M. Weld, K. Mukherjee, and A. C. B. Jayich, *Role of Oxygen in Laser Induced Contamination at Diamond-Vacuum Interfaces*, arXiv:2401.06942 (2024).

[132] M. Kaviani, P. Deák, B. Aradi, T. Frauenheim, J.-P. Chou, and A. Gali, *Proper Surface Termination for Luminescent Near-Surface NV Centers in Diamond*, Nano Letters **14**, 4772 (2014).

[133] J.-P. Tetienne, L. Rondin, P. Spinicelli, M. Chipaux, T. Debuisschert, J.-F. Roch, and V. Jacques, *Magnetic-field-dependent photodynamics of single NV defects in diamond: An application to qualitative all-optical magnetic imaging*, New Journal of Physics **14**, 103033 (2012).

[134] D. Rohner, J. Happacher, P. Reiser, M. A. Tschudin, A. Tallaire, J. Achard, B. J. Shields, and P. Maletinsky, *(111)-oriented, single crystal diamond tips for nanoscale scanning probe imaging of out-of-plane magnetic fields*, Applied Physics Letters **115**, 192401 (2019).

[135] P. Welter, J. Rhensius, A. Morales, M. S. Wörnle, C.-H. Lambert, G. Puebla-Hellmann, P. Gambardella, and C. L. Degen, *Scanning nitrogen-vacancy center magnetometry in large in-plane magnetic fields*, Applied Physics Letters **120**, 074003 (2022).

[136] L. Thiel, *Nanoscale Magnetometry with a Single Spin in Diamond at Cryogenic Temperatures*, Ph.D. thesis, University of Basel (2019).

[137] C. Tang, L. Alahmed, M. Mahdi, Y. Xiong, J. Inman, N. J. McLaughlin, C. Zollitsch, T. H. Kim, C. R. Du, H. Kurebayashi, E. J. Santos, W. Zhang, P. Li, and W. Jin, *Spin dynamics in van der Waals magnetic systems*, Physics Reports **1032**, 1 (2023).

[138] M. Högen, R. Fujita, A. K. C. Tan, A. Geim, M. Pitts, Z. Li, Y. Guo, L. Stefan, T. Hesjedal, and M. Atatüre, *Imaging Nucleation and Propagation of Pinned Domains in Few-Layer Fe5–xGeTe2*, ACS Nano **17**, 16879 (2023).

[139] A. V. Kretinin, Y. Cao, J. S. Tu, G. L. Yu, R. Jalil, K. S. Novoselov, S. J. Haigh, A. Gholinia, A. Mishchenko, M. Lozada, T. Georgiou, C. R. Woods, F. Withers, P. Blake, G. Eda, A. Wirsig, C. Hucho, K. Watanabe, T. Taniguchi, A. K. Geim, and R. V. Gorbachev, *Electronic properties of graphene encapsulated with different two-dimensional atomic crystals*, Nano Letters **14**, 3270 (2014).

[140] S. Liu, X. Yuan, Y. Zou, Y. Sheng, C. Huang, E. Zhang, J. Ling, Y. Liu, W. Wang, C. Zhang, J. Zou, K. Wang, and F. Xiu, *Wafer-scale two-dimensional ferromagnetic Fe_3GeTe_2 thin films grown by molecular beam epitaxy*, npj 2D Materials and Applications **1**, 30 (2017).

[141] M. Ribeiro, G. Gentile, A. Marty, D. Dosenovic, H. Okuno, C. Vergnaud, J.-F. Jacquot, D. Jalabert, D. Longo, P. Ohresser, A. Hallal, M. Chshiev, O. Boulle, F. Bonell, and M. Jamet, *Large-scale epitaxy of two-dimensional van der Waals room-temperature ferromagnet Fe5GeTe2*, npj 2D Materials and Applications **6**, 10 (2022).

[142] M. Liu, Y. L. Huang, J. Gou, Q. Liang, R. Chua, Arramel, S. Duan, L. Zhang, L. Cai, X. Yu, D. Zhong, W. Zhang, and A. T. S. Wee, *Diverse structures and magnetic properties in nonlayered monolayer chromium selenide*, The Journal of Physical Chemistry Letters **12**, 7752 (2021).

[143] A. M. Tokmachev, D. V. Averyanov, O. E. Parfenov, A. N. Taldenkov, I. A. Karateev, I. S. Sokolov, O. A. Kondratev, and V. G. Storchak, *Emerging two-dimensional ferromagnetism in silicene materials*, Nature Communications **9**, 1672 (2018).

[144] A. M. Tokmachev, D. V. Averyanov, A. N. Taldenkov, O. E. Parfenov, I. A. Karateev, I. S. Sokolov, and V. G. Storchak, *Lanthanide f7 metalloxenes – a class of intrinsic 2D ferromagnets*, Materials Horizons **6**, 1488 (2019).

[145] K. S. Kim, D. Lee, C. S. Chang, S. Seo, Y. Hu, S. Cha, H. Kim, J. Shin, J.-H. Lee, S. Lee, J. S. Kim, K. H. Kim, J. M. Suh, Y. Meng, B.-I. Park, J.-H. Lee, H.-S. Park, H. S. Kum, M.-H. Jo, G. Y. Yeom, K. Cho, J.-H. Park, S.-H. Bae, and J. Kim, *Non-epitaxial single-crystal 2D material growth by geometric confinement*, Nature **614**, 88 (2023).

[146] J. Li, X. Yang, Y. Liu, B. Huang, R. Wu, Z. Zhang, B. Zhao, H. Ma, W. Dang, Z. Wei, K. Wang, Z. Lin, X. Yan, M. Sun, B. Li, X. Pan, J. Luo, G. Zhang, Y. Liu, Y. Huang, X. Duan, and X. Duan, *General synthesis of two-dimensional van der Waals heterostructure arrays*, Nature **579**, 368 (2020).

[147] B. Li, Z. Wan, C. Wang, P. Chen, B. Huang, X. Cheng, Q. Qian, J. Li, Z. Zhang, G. Sun, B. Zhao, H. Ma, R. Wu, Z. Wei, Y. Liu, L. Liao, Y. Ye, Y. Huang, X. Xu, X. Duan, W. Ji, and X. Duan, *Van der Waals epitaxial growth of air-stable CrSe2 nanosheets with thickness-tunable magnetic order*, Nature Materials **20**, 818 (2021).

[148] L. Wu, L. Zhou, X. Zhou, C. Wang, and W. Ji, *In-plane epitaxy-strain-tuning intralayer and interlayer magnetic coupling in CrSe2 and CrTe2 monolayers and bilayers*, Physical Review B **106**, L081401 (2022).

[149] P. Reiser et al., *Nanoscale-Resolved Inhomogeneous Magnetism in EuGe2 Monolayer*, (unpublished, manuscript available upon request) .

[150] H. Mattiat, L. Schneider, P. Reiser, M. Poggio, P. Sahafi, A. Jordan, R. Budakian, D. V. Averyanov, I. S. Sokolov, A. N. Taldenkov, O. E. Parfenov, A. M. Tokmachev, and V. G. Storchak, *Mapping the Phase-Separated State in a 2D Magnet*, Nanoscale **16**, 5302 (2024).

[151] M. Loewenhaupt, *Magnetic properties and hyperfine fields of some Eu-compounds with Si, Ge and Sn*, Zeitschrift für Physik **267**, 219 (1974).

[152] S. Bobev, E. D. Bauer, J. D. Thompson, J. L. Sarrao, G. J. Miller, B. Eck, and R. Dronskowski, *Metallic behavior of the Zintl phase EuGe2: Combined structural studies, property measurements, and electronic structure calculations*, Journal of Solid State Chemistry **177**, 3545 (2004).

[153] J. Cadogan, D. Ryan, R. Rejali, and C. Boyer, *The magnetic structure of EuGe2*, Journal of Alloys and Compounds **688**, 51 (2016).

[154] D. V. Averyanov, I. S. Sokolov, A. N. Taldenkov, O. E. Parfenov, I. A. Karateev, O. A. Kondratev, A. M. Tokmachev, and V. G. Storchak, *Intrinsic exchange bias state in silicene and germanene materials EuX2*, Nanoscale Horizons **8**, 803 (2023).

[155] S. Rivillon, Y. J. Chabal, F. Amy, and A. Kahn, *Hydrogen passivation of germanium (100) surface using wet chemical preparation*, Applied Physics Letters **87**, 253101 (2005).

[156] V. Passi, A. Lecestre, C. Krzeminski, G. Larrieu, E. Dubois, and J.-P. Raskin, *A single layer hydrogen silsesquioxane (HSQ) based lift-off process for germanium and platinum*, Microelectronic Engineering **87**, 1872 (2010).

[157] P. Appel, B. J. Shields, T. Kosub, N. Hedrich, R. Hübner, J. Faßbender, D. Makarov, and P. Maletinsky, *Nanomagnetism of Magnetoelectric Granular Thin-Film Antiferromagnets*, Nano Letters **19**, 1682 (2019).

[158] J. Rogiers, E. W. Grundke, and D. D. Betts, *The spin model. III. Analysis of high temperature series expansions of some thermodynamic quantities in two dimensions*, Canadian Journal of Physics **57**, 1719 (1979).

[159] E. C. Stoner and E. P. Wohlfarth, *A mechanism of magnetic hysteresis in heterogeneous alloys*, Philosophical Transactions of the Royal Society of London. Series A, Mathematical and Physical Sciences **240**, 599 (1948).

[160] A. Vansteenkiste, J. Leliaert, M. Dvornik, M. Helsen, F. Garcia-Sanchez, and B. Van Waeyenberge, *The design and verification of MuMax3*, AIP Advances **4**, 107133 (2014).

[161] L. Exl, S. Bance, F. Reichel, T. Schrefl, H. Peter Stimming, and N. J. Mauser, *LaBonte's method revisited: An effective steepest descent method for micromagnetic energy minimization*, Journal of Applied Physics **115**, 17D118 (2014).

[162] J. Leliaert, B. Van De Wiele, A. Vansteenkiste, L. Laurson, G. Durin, L. Dupré, and B. Van Waeyenberge, *Current-driven domain wall mobility in polycrystalline Permalloy nanowires: A numerical study*, Journal of Applied Physics **115**, 233903 (2014).

[163] X. Jiang, Q. Liu, J. Xing, N. Liu, Y. Guo, Z. Liu, and J. Zhao, *Recent progress on 2D magnets: Fundamental mechanism, structural design and modification*, Applied Physics Reviews **8**, 031305 (2021).

[164] V. L. Berezinskii, *Destruction of long-range order in one-dimensional and two-dimensional systems having a continuous symmetry group I. Classical systems*, Soviet Physics JETP **32**, 493 (1971).

[165] J. M. Kosterlitz and D. J. Thouless, *Ordering, metastability and phase transitions in two-dimensional systems*, Journal of Physics C: Solid State Physics **6**, 1181 (1973).

[166] J. M. Kosterlitz, *The critical properties of the two-dimensional xy model*, Journal of Physics C: Solid State Physics **7**, 1046 (1974).

[167] A. Stukowski, *Atomic-Scale Modeling of Nanostructured Metals and Alloys*, Ph.D. thesis, Technische Universität Darmstadt (2010).

[168] Y. Anahory, L. Embon, C. J. Li, S. Banerjee, A. Meltzer, H. R. Naren, A. Yakovenko, J. Cuppens, Y. Myasoedov, M. L. Rappaport, M. E. Huber, K. Michaeli, T. Venkatesan, Ariando, and E. Zeldov, *Emergent nanoscale superparamagnetism at oxide interfaces*, Nature Communications **7**, 12566 (2016).

[169] E. H. d. C. P. Sinnecker, J. M. García-Martín, D. Altbir, J. D'Albuquerque e Castro, and J. P. Sinnecker, *A Magnetic Force Microscopy Study of Patterned T-Shaped Structures*, Materials **14**, 1567 (2021).

[170] S. H. Skjærvø, C. H. Marrows, R. L. Stamps, and L. J. Heyderman, *Advances in artificial spin ice*, Nature Reviews Physics **2**, 13 (2019).

[171] N. Rossi, B. Gross, F. Dirnberger, D. Bougeard, and M. Poggio, *Magnetic Force Sensing Using a Self-Assembled Nanowire*, Nano Letters **19**, 930 (2019).

[172] H. Mattiat, N. Rossi, B. Gross, J. Pablo-Navarro, C. Magén, R. Badea, J. Berezovsky, J. M. De Teresa, and M. Poggio, *Nanowire Magnetic Force Sensors Fabricated by Focused-Electron-Beam-Induced Deposition*, Physical Review Applied **13**, 044043 (2020).

[173] T. Song, M. W.-Y. Tu, C. Carnahan, X. Cai, T. Taniguchi, K. Watanabe, M. A. McGuire, D. H. Cobden, D. Xiao, W. Yao, and X. Xu, *Voltage Control of a van der Waals Spin-Filter Magnetic Tunnel Junction*, Nano Letters **19**, 915 (2019).

[174] S. Giri, M. Patra, and S. Majumdar, *Exchange bias effect in alloys and compounds*, Journal of Physics: Condensed Matter **23**, 073201 (2011).

[175] M.-H. Phan, V. Kalappattil, V. O. Jimenez, Y. Thi Hai Pham, N. W. Mudiyanselage, D. Detellem, C.-M. Hung, A. Chanda, and T. Eggers, *Exchange bias and interface-related effects in two-dimensional van der Waals magnetic heterostructures: Open questions and perspectives*, Journal of Alloys and Compounds **937**, 168375 (2023).

[176] G. Hu, Y. Zhu, J. Xiang, T.-Y. Yang, M. Huang, Z. Wang, Z. Wang, P. Liu, Y. Zhang, C. Feng, D. Hou, W. Zhu, M. Gu, C.-H. Hsu, F.-C. Chuang, Y. Lu, B. Xiang, and Y.-L. Chueh, *Antisymmetric Magnetoresistance in a van der Waals Antiferromagnetic/Ferromagnetic Layered MnPS3/Fe3GeTe2 Stacking Heterostructure*, ACS Nano **14**, 12037 (2020).

[177] P. B. Aravind, K. Aditya, P. Reiser, J. Vas, T. Denneulin, M. A. Tschudin, C. Pellet-Mary, D. Dutta, C. Schrader, T. Scholz, J. Geuchies, S. Fu, H. Wang, A. Bonanni, B. Lotsch, U. Nowak, G. Jakob, A. Kovacs, R. E. Dunin-Borkowski, P. Maletinsky, and M. Kläui, *Thermal cycling induced evolution and colossal exchange bias in Fe3GeTe2/MnPS3 van der Waals heterostructures*, arXiv:2403.05383v1 (2024).

[178] S. Chaudhuri, C. N. Kuo, Y. S. Chen, C. S. Lue, and J. G. Lin, *Low-temperature magnetic order rearrangement in the layered van der Waals compound MnPS3*, Physical Review B **106**, 094416 (2022).

[179] H. Han, H. Lin, W. Gan, R. Xiao, Y. Liu, J. Ye, L. Chen, W. Wang, L. Zhang, C. Zhang, and H. Li, *Field-induced spin reorientation in the Néel-type antiferromagnet MnPS3*, Physical Review B **107**, 075423 (2023).

[180] N. Nagaosa, J. Sinova, S. Onoda, A. H. MacDonald, and N. P. Ong, *Anomalous Hall effect*, Reviews of Modern Physics **82**, 1539 (2010).

[181] B. E. Taylor, J. Steger, and A. Wold, *Preparation and properties of some transition metal phosphorus trisulfide compounds*, Journal of Solid State Chemistry **7**, 461 (1973).

[182] K. Kurosawa, S. Saito, and Y. Yamaguchi, *Neutron Diffraction Study on MnPS3 and FePS3*, Journal of the Physical Society of Japan **52**, 3919 (1983).

[183] G. Long, H. Henck, M. Gibertini, D. Dumcenco, Z. Wang, T. Taniguchi, K. Watanabe, E. Giannini, and A. F. Morpurgo, *Persistence of Magnetism in Atomically Thin MnPS3 Crystals*, Nano Letters **20**, 2452 (2020).

[184] E. Ressouche, M. Loire, V. Simonet, R. Ballou, A. Stunault, and A. Wildes, *Magnetoelectric MnPS3 as a candidate for ferrotoroidicity*, Physical Review B **82**, 100408 (2010).

[185] C. Tan, J. Lee, S.-G. Jung, T. Park, S. Albarakati, J. Partridge, M. R. Field, D. G. McCulloch, L. Wang, and C. Lee, *Hard magnetic properties in nanoflake van der Waals Fe3GeTe2*, Nature Communications **9**, 1554 (2018).

[186] I. O. Robertson, C. Tan, S. C. Scholten, A. J. Healey, G. J. Abrahams, G. Zheng, A. Manchon, L. Wang, and J.-P. Tetienne, *Imaging current control of magnetization in Fe3GeTe2 with a widefield nitrogen-vacancy microscope*, 2D Materials **10**, 015023 (2023).

[187] D. S. Kim, J. Y. Kee, J.-E. Lee, Y. Liu, Y. Kim, N. Kim, C. Hwang, W. Kim, C. Petrovic, D. R. Lee, C. Jang, H. Ryu, and J. W. Choi, *Surface oxidation in a van der Waals ferromagnet Fe3-xGeTe2*, Current Applied Physics **30**, 40 (2021).

[188] M. Rollo, A. Finco, R. Tanos, F. Fabre, T. Devolder, I. Robert-Philip, and V. Jacques, *Quantitative study of the response of a single NV defect in diamond to magnetic noise*, Physical Review B **103**, 235418 (2021).

[189] P. Neumann, I. Jakobi, F. Dolde, C. Burk, R. Reuter, G. Waldherr, J. Honert, T. Wolf, A. Brunner, J. H. Shim, D. Suter, H. Sumiya, J. Isoya, and J. Wrachtrup, *High-Precision Nanoscale Temperature Sensing Using Single Defects in Diamond*, Nano Letters **13**, 2738 (2013).

[190] Z. Qiu, A. Hamo, U. Vool, T. X. Zhou, and A. Yacoby, *Nanoscale electric field imaging with an ambient scanning quantum sensor microscope*, npj Quantum Information **8**, 107 (2022).

[191] Q. Song, C. A. Occhialini, E. Ergeçen, B. Ilyas, D. Amoroso, P. Barone, J. Kapeghian, K. Watanabe, T. Taniguchi, A. S. Botana, S. Picozzi, N. Gedik, and R. Comin, *Evidence for a single-layer van der Waals multiferroic*, Nature **602**, 601 (2022).

[192] H. Zheng, Z. Sun, G. Chatzidrosos, C. Zhang, K. Nakamura, H. Sumiya, T. Ohshima, J. Isoya, J. Wrachtrup, A. Wickenbrock, and D. Budker, *Microwave-Free Vector Magnetometry with Nitrogen-Vacancy Centers along a Single Axis in Diamond*, Physical Review Applied **13**, 044023 (2020).

[193] R. Monge, T. Delord, G. Thiering, Á. Gali, and C. A. Meriles, *Resonant Versus Non-resonant Spin Readout of a Nitrogen-Vacancy Center in Diamond Under Cryogenic Conditions*, Physical Review Letters **131**, 236901 (2023).

[194] J. Görlitz, D. Herrmann, P. Fuchs, T. Iwasaki, T. Taniguchi, D. Rogalla, D. Hardeman, P.-O. Colard, M. Markham, M. Hatano, and C. Becher, *Coherence of a charge stabilised tin-vacancy spin in diamond*, npj Quantum Information **8**, 45 (2022).

[195] J. A. Zuber, M. Li, M. Grimau Puigibert, J. Happacher, P. Reiser, B. J. Shields, and P. Maletinsky, *Shallow Silicon Vacancy Centers with Lifetime-Limited Optical Linewidths in Diamond Nanostructures*, Nano Letters **23**, 10901 (2023).

[196] J. Liu, M. Shi, P. Mo, and J. Lu, *Electrical-field-induced magnetic Skyrmion ground state in a two-dimensional chromium tri-iodide ferromagnetic monolayer*, AIP Advances **8**, 055316 (2018).

[197] A. K. Behera, S. Chowdhury, and S. R. Das, *Magnetic skyrmions in atomic thin CrI3 monolayer*, Applied Physics Letters **114**, 232402 (2019).

[198] L. Ciorciaro, T. Smoleński, I. Morera, N. Kiper, S. Hiestand, M. Kroner, Y. Zhang, K. Watanabe, T. Taniguchi, E. Demler, and A. İmamoğlu, *Kinetic magnetism in triangular moiré materials*, Nature **623**, 509 (2023).

[199] T. van der Sar, F. Casola, R. Walsworth, and A. Yacoby, *Nanometre-scale probing of spin waves using single electron spins*, Nature Communications **6**, 7886 (2015).

[200] D. MacNeill, J. T. Hou, D. R. Klein, P. Zhang, P. Jarillo-Herrero, and L. Liu, *Gigahertz Frequency Antiferromagnetic Resonance and Strong Magnon-Magnon Coupling in the Layered Crystal CrCl3*, Physical Review Letters **123**, 047204 (2019).

Acknowledgments

During my PhD time I received a lot of support from various people. Hence, many people have contributed to this work and without them this thesis would not be possible. I would like to thank them all for their help and express my gratitude to all of them.

First of all, I would like to thank Patrick for giving me the opportunity to do a PhD thesis in his group and for all his support and supervision during this time. I enjoyed our deep physical discussions and appreciated his critical remarks and questions, which significantly improved my work. Furthermore, his passion for physics in general and for our scientific work motivated and inspired me to work on difficult and big challenges. I also always felt his support in difficult times when the experiments did not work as planned or other obstacles arose. In particular his understanding of difficult situations arising from outside the work helped me to cope with them and allowed me to focus on the work again. I enjoyed working with and for you and thank you for the great time with you and your group.

I would also like to thank my colleagues in the quantum sensing lab. Especially my team members from the 4K team: Lucas, David, Caroline, Debarghya, Clément and in particular Märta. It was a great pleasure to work with them and we had a great atmosphere in our team that allowed us to tackle all the challenges that come with running a cryogenic setup. I am grateful for all the support and hands on advice on problems in the lab and life in general. I would also like to thank Kai, Jodok and Paul for all our interesting discussions about science and life in general and all the fun we had together in the lab and in the office. It was great to be able to rely not only on colleagues but also on friends. Finally, a big thank you to all the members of the group for all their advice, help and support. It was an inspiring atmosphere to work with you. Thank you all.

I would also like to thank my collaborators: Martino for taking over the second supervision and being a great alternative contact person in the department. Also thanks for the interesting discussions with you and your team members Boris, Hinrich and Lukas on the EuGe$_2$ project. Jan for being willing to evaluate my thesis as an external supervisor and for investing many hours to enable my graduation. I also appreciate the contact with the Fraunhofer Institute that you made possible. Mathias and his team members Aravind and Aditya for initiating the exchange bias investigations and providing me with the samples to investigate them using scanning NV magnetometry.

Next, I would like to thank the university staff for all their support and help: Arnold for helping me with all the technical issues that come with working in a complex laboratory environment. Dominik for providing the necessary liquid helium for my cryogenic experiments. Laurent and Gerard for managing the clean room and allowing me to perform the fabrication processes required for my work. Sascha and the mechanical workshop for providing me with individual mechanical components needed

for the experiments. Michael and the electronics workshop for helping us with all the electrical problems that arise during complicated experiments. Christian, Jenny and Germaine and the whole administration team for managing all the administrative work needed to do the research. A big thank you to all of you.

Finally, I would like to thank my family for all their support. First of all, my wife for all her understanding in difficult situations and the great life we built together, which gave me the mental resources to complete such a big project as my PhD thesis. My parents and my brother for encouraging me to choose such a difficult path and tackle the scientific challenges. All the rest of my family and friends to being there for me when I needed them. A big thank you to all of you.

Curriculum Vitae

Personal Details

Name	Patrick Siegwolf (Reiser)
Date of Birth	22 of August 1993
Place of Birth	Überlingen, Germany
Email	patrick.reiser@unibas.ch

Education

2019 – 2024	University of Basel, PhD in Experimental Physics
2016 – 2018	University of Freiburg, Master of Science in Applied Physics
	Master thesis in the group of PD F. Kühnemann (Fraunhofer IPM)
	Nichtlinear-Optischer Hochkonverter für die Laserspektroskopie im Mittleren Infrarot
2012 – 2016	University of Konstanz, Bachelor of Science in Physics
	Bachelor thesis in the group of Prof. L. Schmidt-Mende
	Investigation into the electroluminescence decay and rise times of methylammonium lead bromide perovskite-LEDs
2004 – 2012	Nellenburg-Gymnasium Stockach, Abitur

Publications

[201] **P. Reiser** et al., *Nanoscale-Resolved Inhomogeneous Magnetism in EuGe2 Monolayer*, (unpublished, manuscript available upon request).

[202] P. B. Aravind, K. Aditya, **P. Reiser**, J. Vas, T. Denneulin, M. A. Tschudin, C. Pellet-Mary, D. Dutta, C. Schrader, T. Scholz, J. Geuchies, S. Fu, H. Wang, A. Bonanni, B. Lotsch, U. Nowak, G. Jakob, A. Kovacs, R. E. Dunin-Borkowski, P. Maletinsky, M. Kläui, *Thermal Cycling Induced Evolution and Colossal Exchange Bias in Fe3GeTe2/MnPS3 van Der Waals Heterostructures*, arXiv:2403.05383, (2024).

[203] H. Mattiat, L. Schneider, **P. Reiser**, M. Poggio ,P. Sahafi, A. Jordan, R. Budakian, D. V. Averyanov, I. S. Sokolov, A. N. Taldenkov, O. E. Parfenov, A. M. Tokmachev, V. G. Storchak, *Mapping the Phase-Separated State in a 2D Magnet*, Nanoscale **16**, 5302 (2024).

[204] J. A. Zuber, M. Li, M. Grimau Puigibert, J. Happacher, **P. Reiser**, B. J. Shields, P. Maletinsky, *Shallow Silicon Vacancy Centers with Lifetime-Limited*

Optical Linewidths in Diamond Nanostructures, Nano Letters **23**, 10901–10907, (2023).

[205] M. A. Tschudin, D. A. Broadway, **P. Reiser**, C. Schrader, E. J. Telford, B. Gross, J. Cox, A. E. Dubois, D. G. Chica, R. Rama-Eiroa, E. J. Santos, M. Poggio, M. E.Ziebel, C. R. Dean, X. Roy, P. Maletinsky, *Nanoscale Magnetism and Magnetic Phase Transitions in Atomically Thin CrSBr*, arXiv:2312.09279, (2023).

[206] X. Li, A. C. Jones, J. Choi, H. Zhao, V. Chandrasekaran, M. T. Pettes, A. Piryatinski, M. A. Tschudin, **P. Reiser**, D. A. Broadway, P. Maletinsky, N. Sinitsyn, S. A. Crooker, H. Htoon, *Proximity-Induced Chiral Quantum Light Generation in Strain-Engineered WSe2/NiPS3 Heterostructures*, Nature Materials **22**, 1311–1316 (2023).

[207] J. Happacher, J. Bocquel, H. T. Dinani, M. A. Tschudin, **P. Reiser**, D. A. Broadway, J. R. Maze, P. Maletinsky, *Temperature-Dependent Photophysics of Single NV Centers in Diamond*, Physical Review Letters **131**, 086904 (2023).

[208] J. Happacher, D. A. Broadway, J. Bocquel, **P. Reiser**, A. Jimenéz, M. A. Tschudin, L. Thiel, D. Rohner, M. Puigibert, B. Shields, J. R. Maze, V. Jacques, P. Maletinsky, *Low-Temperature Photophysics of Single Nitrogen-Vacancy Centers in Diamond*, Pysical Review Letters **128**, 177401 (2022).

[209] D. Rohner, J. Happacher, **P. Reiser**, M. A. Tschudin, A. Tallaire, J. Achard, B. J. Shields, P. Maletinsky, *(111)-Oriented, Single Crystal Diamond Tips for Nanoscale Scanning Probe Imaging of out-of-Plane Magnetic Fields*, Applied Physical Letters **115**, 192401 (2019).

June 25, 2024